Hybrid Interfaces: Adsorption of Aromatic Molecules on Metals

Anu Baby

A thesis presented for the degree of

Doctor of Philosophy

Department of Materials Science

University of Milano-Bicocca

Italy

January 2016

Hybrid Interfaces: Adsorption of Aromatic Molecules on Metals

Ph.D. Thesis

Anu Baby

Supervisor: Prof. Gian Paolo Brivio

Co-Supervisor: Dr. Guido Fratesi

Secondment Supervisor: Prof. Egbert Zojer

Abstract

This thesis presents the density functional theory (DFT) studies of the adsorption of aromatic molecules on metals with perspective applications in organic electronics. These hybrid interfaces are found at the metal contacts in organic electronic devices. Understanding the precise electronic structure including the energy alignment between the Fermi level of the metal and the HOMO/LUMO states of the molecule is essential as it influences the carrier injection across the interface, which in turn affects the overall performance of these devices. Additionally the topography of such a first layer of adsorbates is very important as it drives the orientation of the subsequent growing layers.

In this respect I have investigated by DFT including the van der Waals interactions two systems namely pentacene adsorbed on Al(001) and K doping of 3,4,9,10-perylene tetracarboxylic dianhydride (PTCDA) adsorbed on Ag(111). The structural, electronic, and spectroscopic properties of the first system, pentacene adsorbed on the Al(001) surface was studied computationally in collaboration with the experimental group of Dr. Luca Floreano at ELETTRA, Trieste, Italy who measured the X-ray photoemission spectra (XPS), the near-edge X-ray absorption fine structure (NEXAFS), and the surface morphology by scanning tunneling microscopy (STM). In the most stable adsorption configuration, pentacene is bent into a V-shape due to the

direct anchoring of the two central carbons atop the two Al atoms underneath and oriented with the long axis parallel to the substrate [110] direction. Such an anchoring is favoured by optimally matched interatomic distances which also results in filling of the LUMO.

Next I have investigated computationally K doping of PTCDA adsorbed on Ag(111), during my secondment at the Graz University of Technology, Austria with the experimental collaboration of Prof. Torsten Fritz and group at the Friedrich Schiller University Jena, Germany. In fact once you have an ordered layer, another key parameter to be tuned as far as the device performance is concerned is the number of charge carriers which can be improved by doping. Alkali metal atoms are very good candidates for the n-type doping of organic semiconductors and are frequently used. The adsorption of dopant atoms from the gas phase into the molecular crystal structures needs to be controlled and well understood in order to optimize the electronic properties (charge carrier density and mobility) of the target semiconductor material. The K doping of PTCDA/Ag(111) results in highly ordered and large K_xPTCDA domains. The emerging structures were found to be stable for stoichiometries $x = 2$ and 4 by combining the experimental low temperature STM, scanning tunneling hydrogen microscopy (STHM), and low-energy electron diffraction (LEED) methods with DFT calculations. The DFT calculations proved to be crucial for locating the positions of K atoms by interpreting the experimental ST[H]M data correctly for the stoichiometry $x = 4$. Our calculations have shown that the K atoms eventually lose their electrons to PTCDA and the Ag substrate thereby filling the LUMO and reducing the surface work function.

Dedication

To amma and papa

Acknowledgements

First of all, I am pleased to express my indebtedness, to Prof. Gian Paolo Brivio, my supervisor for giving me the opportunity to do this work, for his constant motivation and guidance throughout my Ph.D., and for correcting and encouraging me whenever things were challenging. I cannot express my sincere gratitude enough to my co-supervisor, Dr. Guido Fratesi, who taught me how to run scientific computer simulations and analyse the results. I am grateful for his immense patience at numerous hard times, for helping me and clearing all my doubts. I am indebted to Prof. Egbert Zojer who was my supervisor during my secondment in Graz University of Technology, Austria for his constant help and support during my stay there. Many thanks to Dr. Luca Floreano and his group at Elettra, Trieste, Italy and Prof. Torsten Fritz and his group at Friedrich Schiller University, Jena, Germany for their excellent experimental collaboration. I would like to thank the members (former and current) of my group at the University of Milano-Bicocca, Italy: Carlo Motta, He Lin, Abhilash Ravikumar, Moritz Müller, Aldo Ugolotti and my colleagues at Graz University of Technology, Austria: Oliver T. Hofmann, Iris Hehn, Elisabeth Verwüster, Shashank Harivyasi, Elisabeth Wruß, Veronika Obersteiner, Gernot Kraberger, and Thomas Taucher. I also acknowledge the PCAM European Doctorate Programme within which this work has been done.

My beloved parents, Mr. Baby and Mrs. Rajamma and sister Ms. Anju, even if 4500 miles far away, always supported me through their boundless love, prayers and blessings. Whenever I was in need, my best friends were there for me, Nastassja and Görkem, thanks to both of you. Last but not the least I would like to thank Andrea for being there by my side during all the difficult times through my joys and sorrows, for always inspiring me and cheering me up whenever I was in low spirits.

Contents

1 Introduction **9**

1.1 Organic Electronics 9

1.2 Metal Organic Interfaces 11

1.3 Doping of Organic Molecules 13

2 Computational Methods and Physical Background **15**

2.1 Density Functional Theory (DFT) 15

2.1.1 Introduction 15

2.1.2 Hohenberg-Kohn and Kohn-Sham Theorems 17

2.1.3 Approximations to the exchange correlation functional 20

2.2 X-ray Photoelectron Spectroscopy (XPS) 22

2.3 Near Edge X-ray Absorption Fine Structure Spectroscopy (NEXAFS) 24

2.4 Scanning Tunnelling Microscopy (STM) and Scanning Tunnelling Hydrogen Microscopy (STHM) 27

3 Pentacene/Al(001) **30**

3.1 Introduction 30

3.2 Experimental Interface Morphology 32

3.3 Computational Method and Results 35

3.3.1 Structure of the adsorbed system 36
3.3.2 Origin of the V-shape 41
3.3.3 Effects of V-shape on Bond Length 42
3.3.4 Ground State Electronic Properties and Charge Transfer 45
3.4 XPS 50
3.5 NEXAFS 54
3.6 STM 63

4 Potassium doping of PTCDA/Ag(111) 67
4.1 Introduction 67
4.2 Experimental Findings 69
4.3 Computational Approach and Results 77
4.3.1 Modification of the Ag substrate 78
4.3.2 Structural Optimization 80
4.3.3 ST[H]M 88
4.3.4 Electronic Structure and Charge Transfer Analysis . . 96

5 Conclusions 102

A Quantum Espresso 105

B Vienna Ab Initio Simulation Package (VASP) 107

C Molecular Orbital Projected Density of States (MOPDOS) 109

Bibliography 111

Chapter 1

Introduction

1.1 Organic Electronics

"A single molecule or a group of molecules could change the world" - Hiroo Inokuchi [1].

Organic semiconductors have shown the potential to produce several technologically important devices which are fast approaching commercial viability opening up the field of future electronics [2, 3, 4]. This is as a result of the intense research that has been carried out in this field, giving space for the very obvious question: what has prompted so much research attention in organic electronics? The answer lies in the useful properties of organic materials such as low-cost and easy manufacturing processes, flexibility, light-weight, and achievable nanoscale active device area. These combination of properties has attracted large scale production interest. The first ever organic field effect transistor was fabricated in the year 1986 using the polymer polythiophene [5] and the first organic light emitting field effect transistor was developed in the year 2003 with tetracene as the semiconducting material [6]. Since then organic semiconductors have been employed for numerous applications such

as in organic light-emitting diodes (OLEDs) for displays [7, 8], organic field effect transistors (OFETs) and thin film transistors (TFTs) [9], photovoltaic devices [10, 11], memory devices [12, 13], chemical vapor sensors [14] etc. Hence, for the past 50 years the research and engineering concerning this class of materials has been carried out with the aim of establishing a new organics based electronic industry.

The two main classes of organic materials usually considered are: polymers and oligomers. Their structures comprising polymeric and molecular units respectively, exhibit the common feature of delocalized π -conjugated electrons from the p_z orbitals of the sp^2 -hybridized C atoms, giving rise to delocalized filled bonding (π-orbital) and empty anti-bonding (π^*-orbital) that greatly impact the optical and electrical properties [9]. And the lowest electronic excitation occurs between these $\pi - \pi^*$ orbitals. Polymers are long-chain molecules consisting of a large number of molecular repeated units, easy and cheap to process. While oligomers are low molecular weight small organic molecules difficult to prepare but yielding semiconductors with well ordered layers [15]. The former ones can be prepared only from solution (spin-coating or printing) while the latter can be deposited from gas phase by means of sublimation or evaporation. Due to the achievable high purity and quality of film, most of the devices that have reached the market are based on oligomers. The molecular backbone of an oligomer is formed by strongly linked σ-bonds whereas the intermolecular interactions are through weaker π-bonds.

The synthesis of new organic materials along with understanding their electronic structure are the key ingredients in designing high performance organic electronic devices. The number of possible applications grows as materials with desired properties such as low-cost, lightweight, flexibility,

(perhaps also disposable) etc. as mentioned earlier, become available. The organisation Chemical Abstracts Service (CAS) has registered around 102 million organic and inorganic compounds till date. The easiness with which these materials can be processed is another important factor required for commercialization. The advantage of using organic materials in the devices gives the possibility to manufacture the latter by printing methods such as inkjet, roll-to-roll, which simplifies, speeds-up and reduces the cost of mass production. Some of these devices are now reaching the consumer market, OLEDs being the most successful among them [16]. Though, for many applications commercialization is hindered by poor device performance and operational stability. One major drawback of many organic devices is that they can fail even at ambient temperatures due to the low melting or glass transition temperatures, which limits the lifetime and operational environment of these devices.

Since many applications encompass several thin film layers made of organic and inorganic materials, the understanding of both organic-inorganic hybrid interfaces is an important issue necessary for the successful development of organic electronics.

1.2 Metal Organic Interfaces

The metal organic interfaces are found at the metal contacts in organic electronic devices. Even though single crystals can be grown from organic molecules it is difficult to attach metal contacts to them as such crystals are soft. So, it is preferable to deposit thin layers of organic molecules onto the substrate already containing metal electrodes [15]. The fact that organic molecules in contrast to atoms have an anisotropic shape leads to a num-

ber of new aspects and effectively introduces a new dimensionality in such a film growth. Moreover, these molecules are rather soft and can deform when brought into contact with another substrate or even in the molecular bulk. The topography and order of the first layer of organic molecules are very important as they form the foundation for the growth of the subsequent layers. Such a first layer can also induce possible stress and strain in the underlying metal substrate. When the observed lattice constant is smaller/larger than the bulk value compressive/tensile strain is detected in the film [15]. To study the growth relationship of the adsorbate layer with the substrate usually single-crystal surfaces are considered even if production wise they are very expensive.

For device applications it is also extremely important to study the electronic structure at the interface. The energy level alignment between the Fermi level of the metal and the states of the molecule is critical as it influences the carrier injection across the interface, which in turn affects the overall performance of organic electronic devices [17]. The difference in energy between the Fermi level of the metal and the HOMO/LUMO of the molecule is called the hole/electron injection barrier. The interaction between the adsorbate molecules and the metal substrate can induce some charge rearrangements and hence shift the vacuum level closer to/farther from the Fermi energy level thereby reducing/increasing the surface work function.

In the case of metals, atoms are held together by metallic bonds where the nuclei together with the core electrons form a background potential in which the deocalized valence electrons move around like a nearly free electron cloud. Whereas the backbone of an aromatic molecule is made up of carbon and hydrogen atoms held together by covalent bonds. In the crystal these molecules are held together by rather weak van der Waal's (vdW)

bonds. Aromatic hydrocarbons mostly adsorb planar when on direct contact with metal surfaces, which maximizes the overlap of their π-orbitals with the electron cloud for effective charge transfer at the interface [18, 19, 20, 21]. In this case, the charge transfer takes place perpendicular to the substrate. In some other cases when the molecules adsorb perpendicular or tilted thereby minimizing the overlap of the π-orbitals with the substrate [22] the charge transfer mainly takes place parallel to the substrate. The π-electrons are involved in bonding and their interaction strength with the substrate ranges from relatively weak to strong, depending on the system under consideration. In fact, the criteria for categorizing the bonding as physisorption or chemisorption are subject to revision in the recent literature [21, 23]. The vdW interactions play a crucial role in stabilizing the adsorption of molecules to surfaces, and the physisorption binding energy can exceed that of covalent bonding [24]. In this case the vdW force is the London dispersion one which is defined as that between two non-polar materials polarizable by instantaneous charge fluctuations. A theoretical description of the vdW interactions is difficult to implement in DFT as the former one is a non-local force whereas the latter method deals with local or semi-local forces. In this thesis, pentacene/Al(001) hybrid interface is investigated by taking into account the vdW interactions.

1.3 Doping of Organic Molecules

The two key parameters to be considered for the efficient functioning of a semiconductor device whether it be organic or inorganic are (1) the order of the conducting layer which affects the mobility of charge carriers and (2) the doping which affects the number of charge carriers [25, 26]. The topography

of the conducting layer and its importance in the energy level alignment and charge transfer were discussed in Section 1.2. Once we have well-ordered layers, the charge carrier density can be tuned by doping. Doping an organic semiconductor is different from that of an inorganic one as the doping concentration in the latter is in terms of ppm (parts per million), whereas in the former one it could be even one or two atoms per organic molecule. It is notable that subtle changes in the structure or composition of an organic material can alter its bulk properties [16]. The first successful controlled doping of conjugated polymers was achieved in the 1970s which was honoured with the Nobel prize in Chemistry in the year 2000 [27]. They were able to accomplish an increase in the electrical conductivity of polyacetylene over eleven orders of magnitude by doping with halogens [28]. Superconductivity has also been reportedly attained by alkali doping of the organic molecule picene [29]. Another interesting property achieved so far is the insulator-metal-insulator phase transition [30].

So, understanding the effects of controlled doping on organic systems is very important and requires detailed investigations. The microscopic molecular structures formed during doping although crucial for the understanding of the associated physical properties are not yet well-established. Predominantly vdW bound molecular crystals are prone to reordering processes upon intercalation with atoms leading to new crystalline or amorphous phases [31, 32, 33, 34, 35, 36, 37]. For doped molecular thin films in the monolayer regime, the presence of an interface with the substrate further increases the complexity of the system by providing additional interaction channels and, thus, possibly influencing the physical and electronic structures extensively. To this respect, in this thesis, the K doping of PTCDA monolayer adsorbed on Ag(111) is studied.

Chapter 2

Computational Methods and Physical Background

Electrons play a fundamental role in determining the properties of matter. Hence, as already discussed in the introduction, understanding the electronic structure is crucial for designing new organic materials and hybrid interfaces. The electronic structure can be obtained by using theoretical methods of quantum mechanics. The basic definitions and equations of the most widely used method for computational ab-initio studies which is also employed in this work are discussed in this chapter. How such an approach is able to simulate the experimental results of this work is outlined as well.

2.1 Density Functional Theory (DFT)

2.1.1 Introduction

Solving the Schrödinger equation for interacting electrons and nuclei remains the biggest challenge in the field of quantum mechanics. Density Functional

Theory (DFT), the most widely used theory for performing electronic structure calculations of matter, has been astonishingly successful in achieving this goal. It was conceived in its initial simplest version in 1927 independently by Thomas [38] and Fermi [39], immediately after the foundation of quantum mechanics by E. Schrödinger in 1926 [40]. It is referred to as *ab initio* or first principles method as it is a non-empirical quantum mechanical one or in other words it does not use any experimentally obtained parameters other than fundamental constants. It is a ground state theory with charge density as the relevant physical quantity.

For a many-body system where multiple electrons are interacting with several nuclei, the Hamiltonian is given by:

$$\begin{aligned} H =& KE_e + KE_N + V_{ee} + V_{NN} + V_{eN} \\ =& -\frac{\hbar^2}{2m}\sum_i \nabla^2_{\mathbf{r}_i} - \frac{\hbar^2}{2M_I}\sum_I \nabla^2_{\mathbf{R}_I} + \frac{1}{2}\sum_{i\neq j}\frac{e^2}{|\mathbf{r}_i - \mathbf{r}_j|} \\ &+ \frac{1}{2}\sum_{I\neq J}\frac{Z_I Z_J e^2}{|\mathbf{R}_I - \mathbf{R}_J|} - \sum_{i,I}\frac{Z_I e^2}{|\mathbf{r}_i - \mathbf{R}_I|} \end{aligned} \tag{2.1}$$

where $\hbar$ is the Planck constant divided by 2π, m is the mass and e is the charge of an electron, M_I is the mass and Z_I is the charge of the nucleus I, KE_e is the kinetic energy of electrons, KE_N is the kinetic energy of nuclei, V_{ee} is the interaction potential between two electrons at positions $\mathbf{r}_i$ and $\mathbf{r}_j$, V_{NN} is that between nuclei at positions $\mathbf{R}_I$ and $\mathbf{R}_J$, and V_{eN} between electrons and nuclei (which is a negative quantity as it is an attractive potential) at positions $\mathbf{r}_i$ and $\mathbf{R}_I$ respectively. The Born-Oppenheimer approximation is used in order to simplify the situation further assuming that the electronic problem can be decoupled from the nuclear one. This simplification is justified because the nuclei are much heavier than the electrons and hence the motion of electrons can be separated from that of the nuclei. We can write the Hamiltonian of the electrons considering the nuclei coordinates as

a parameter.

$$\begin{aligned} H_e &= KE_e + V_{ee} - V_{eN} \\ &= -\frac{\hbar^2}{2m}\sum_i \nabla^2_{\mathbf{r}_i} + \frac{1}{2}\sum_{i\neq j}\frac{e^2}{|\mathbf{r}_i - \mathbf{r}_j|} - \sum_{i,I}\frac{Z_I e^2}{|\mathbf{r}_i - \mathbf{R}_I|} \end{aligned} \tag{2.2}$$

But the situation remains a many body problem which makes it difficult to solve the Schrödinger equation.

2.1.2 Hohenberg-Kohn and Kohn-Sham Theorems

The calculation of the ground state energy of a system can be performed in principle exactly following the two theorems by Hohenberg and Kohn with the introduction of charge density as the basic variable. The first theorem [41] states that *the ground state energy $E[\rho(\boldsymbol{r})]$ of an N electron system is a unique functional of the ground state electron density $\rho(\boldsymbol{r})$.* The importance of this theorem lies in the fact that the ground state energy can be determined from the electron density which is a function of 3 spatial variables plus spin rather than wave function which is of $3N$ spatial variables plus spin. The second theorem states an important property of the energy functional that *relative to the arbitrary variations in the electron density and subject to the constraint of fixed number of particles, the density that gives the minimum ground state energy is the exact ground state density.* If the exact form of the functional were known, the electron density could be varied until the energy functional were minimized. Since this is unfeasible in most problems, in 1965 Kohn and Sham (KS) suggested a different approach to find the ground state electron density of an auxiliary system whose ground state electron density is same as that of the interacting one [42]. They proposed solving a single electron equation.

$$H_{KS}\psi_i(\mathbf{r}) = [-\frac{\hbar^2}{2m}\nabla^2_{\mathbf{r}_i} + V_{eff}(\mathbf{r})]\psi_i(\mathbf{r}) = \epsilon_i\psi_i(\mathbf{r}) \tag{2.3}$$

And hence an interacting many body problem has been reduced in dimensionality into a non-interacting single particle one with ground state density defined as $\rho(\mathbf{r}) = \sum_{i=1}^{N} |\psi_i(\mathbf{r})|^{\mathbf{2}}$, as the basic variable. The effective potential in equation 2.3 is given by,

$$V_{eff}(\mathbf{r}) = V_{ext}(\mathbf{r}) + V_H(\mathbf{r}) + V_{XC}(\mathbf{r}) \tag{2.4}$$

where $V_{ext}(\mathbf{r})$ is the interaction potential between electrons and the nuclei, $V_H(\mathbf{r})$ is the Hartree potential which describes the classical Coulomb repulsion. This also includes the self-interaction contribution, i.e. the repulsion of an electron from itself which is unphysical. Methods have been devised to amend this drawback [43]. The last term $V_{XC}(\mathbf{r})$ is the exchange-correlation potential which also usually includes the correction for the unphysical self-interaction contribution, and its exact form is unknown. The quality of this approximation determines the accuracy of the found ground state electron density and energy. Overall the exact $V_H(\mathbf{r}) + V_{XC}(\mathbf{r})$ bears no self-interaction.

The level of simplicity of the KS equation makes possible to solve it for small systems even on a normal desktop computer. A flow chart demonstrating the general computational procedure employed to find a self-consistent solution to the KS equation is shown in figure 2.1. Initially the external potential $V_{ext}(\mathbf{r})$ is constructed from the known atomic numbers and positions. The initial charge density $\rho(\mathbf{r})$ is guessed and $V_H(\mathbf{r})$ and $V_{XC}(\mathbf{r})$ are calculated, and hence $V_{eff}(\mathbf{r})$. The wavefunctions are expanded on a suitable basis set. This is followed by the construction of the KS Hamiltonian matrix which is then diagonalized to obtain the KS eigenstates. Once solved for all the N occupied states, $i = 1, 2...N$, the resulting KS eigenstates are used to compute back the charge density. It is checked if the final output charge

Figure 2.1: Flow chart describing the general computational procedure to find a self-consistent solution to the KS equation.

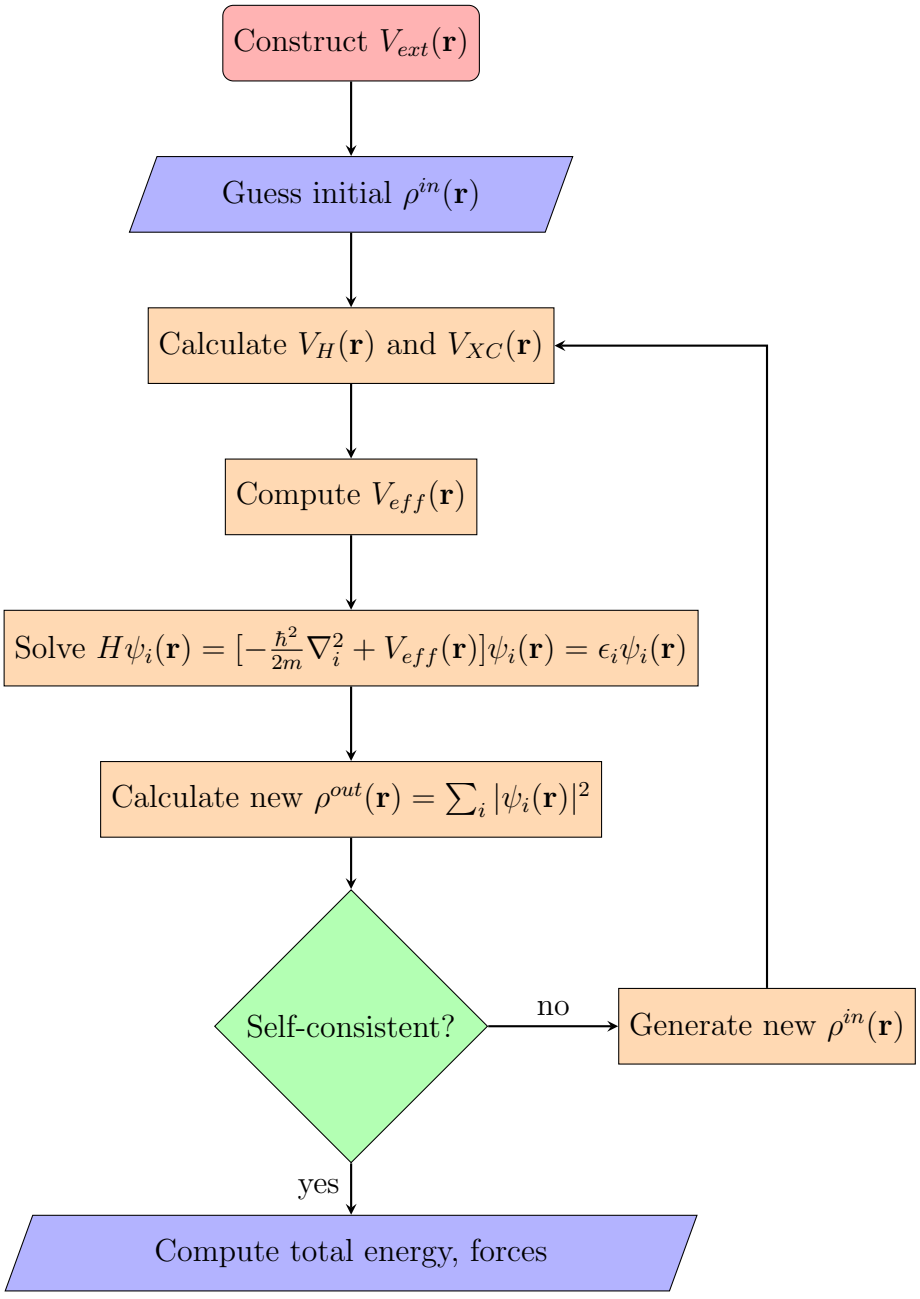

density $\rho^{out}(\mathbf{r})$ is self-consistent. If not, the procedure is repeated and if yes, the self-consistency cycle is stopped and the total energy of the system is calculated.

2.1.3 Approximations to the exchange correlation functional

The most widely used approximations for the exchange-correlation functional are the local density approximation (LDA) and the generalized-gradient approximation (GGA). The LDA uses the exchange-correlational energy of a homogeneous electron gas locally dependent on $\rho(\mathbf{r})$ and can be considered when the deviations in the electron density are smaller. A variation of LDA, called the local spin density approximation (LSDA), can be used for spin dependent systems which also includes a spin polarization functional. Some non-locality was introduced in the exchange correlational functional by a gradient expansion of the density called the gradient expansion approximation (GEA) [44]. Then the generalized gradient approximation (GGA) [45] was proposed to set physical constraints on the exchange and correlation holes, satisfied by the uniform electron gas (LSDA) but not by GEA, obtaining much improved results [43]. In this work a form of GGA called PBE (Perdew-Burke-Ernzerhof) is used [46]. It contains a unified real space cut-off for exchange and correlation holes to avoid spurious long range parts in the second order gradient expansion of density. The PBE does not have any fitting parameters, retains correct features of LSDA, and combines them with the most energetically important features of gradient-corrected non-locality.

As already discussed in section 1.2 metal-organic interfaces are influenced by the vdW forces. These vdW interactions called the London dispersion forces are exhibited by non-polar atoms because of the correlated motion

of electrons in them. For this reason, the electronic charge in one atom fluctuates or redistributes when in proximity to another atom. This is frequently described as the formation of instantaneous dipoles. The resulting force due to the attractive interaction potential between these two atoms, with no permanent dipole moments, separated by a distance R exhibiting an R^{-6} asymptotic behaviour is called the disperion or vdW force. The standard PBE functional can be corrected to include this kind of weak long-range interactions in our calculations. Two approaches namely (1) the Grimme (called DFT-D) [47] and (2) the modified Tkatchenko-Scheffler (called vdW^{surf}) [48] have been used for the same in this work.

(1) In Grimme's approach the semiempirical Becke's GGA B97-D (energy functionals with gradient contributions expanded up to second order) [49] is parameterized by including damped atom-pairwise potentials of the form $C_6^{ij} R_{ij}^{-6}$ which are obtained by suitably fitting the experimental data (where C_6^{ij} is the dispersion coefficient for atoms i, j and R_{ij} is their interatomic distance).

(2) The second approach combines the Tkatchenko-Scheffler (TS) method [50] with the Lifshitz-Zaremba-Kohn (LZK) theory [51, 52], where the latter models Coulomb screening of the bulk [48]. In the TS method, the C_6^{ij} and R_{ij} are derived from the electron density of a molecule or a solid (by DFT-GGA) and accurate reference data for the free atoms. By including the LZK theory, C_6 coefficients and the vdW radii are determined by taking into account also the many-body collective response (screening) of the substrate electrons, which goes beyond the pairwise description. We recall that the vdW radius is defined as the distance at which the Pauli repulsion balances the attraction forces between two atoms [53].

In this thesis two codes have been used to perform the DFT calculations:

Quantum Espresso (see Appendix A) for pentacene/Al(100) and VASP (see Appendix B) for K doping of PTCDA/Ag(111). In the former the Grimme method and in the latter the modified TS one are implemented.

2.2 X-ray Photoelectron Spectroscopy (XPS)

The interaction of an X-ray photon of appropriate energy with a sample material ejects a photoelectron and X-ray Photoelectron Spectroscopy (XPS) is the study of the energy distribution of such photoelectrons. It is also called *Electron Spectroscopy for Chemical Analysis (ESCA)* following the extensive studies of chemical structure by Kai Siegbahn and his colleagues [54]. It is a surface technique, sensitive upto 10 nm depth. Its relevance lies in the fact that even if the atomic core electrons have no role in chemical bond formation, their binding energy changes depending on the chemical environment of the atom [55]. And probing the binding energy of the core electrons can shed light onto the bonding character of an atom. Because of energy conservation the photoemission process can be written as:

$$h\nu = BE + KE_{det}(e) + e\phi_{det} \tag{2.5}$$

where $h\nu$ is the energy of the incoming photon, BE is the binding energy of the photoemitted core electron, $KE_{det}(e)$ is the kinetic energy and $e\phi_{det}$ is the potential energy of the photoelectron both taken at the detector [56]. The binding energy is defined as the difference in energy between the ionized and the ground states of the system.

$$BE = E^{+} - E^{0} \tag{2.6}$$

where E^{+} is the energy of the ionized system and E^{0} is that of the system in ground state. The core level binding energy, BE is a fingerprint of an

element and hence can be used to determine the chemical composition of a surface. As already mentioned BE is sensitive to the chemical environment such as surface potential, change in geometry, charge transfer etc. and the resulting changes in BE are called core level shifts (CLS) or chemical shifts.

In DFT calculations, two models often used for the prediction of chemical shifts are: the initial state method and the ΔSCF method [56] where SCF stands for self-consistent field. The initial state method neglects the effects of relaxation of the core and valence electrons in the presence of core hole. In other words it takes into account only the effects that occur before the photoemission. This approximation can be used to describe the CLS due to the different chemical environments and requires only a ground state calculation. Whereas in the ΔSCF approach the valence electrons relax fully in the presence of the core hole thereby also accounting for the screening process. Two important assumptions considered here are (1) the valence electrons are in the ground state; (2) the geometry does not change after ionization [56]. The ΔSCF method is adopted in this work and the BE is computed using the equation 2.6. To compute E^+, a pseudopotential with a core hole is employed. Depending on the nature of the system the core hole may or may not be screened by an extra electron. If there are plenty of free charges available for screening like in the case of a metal substrate, an extra electron is considered at the Fermi level of the system and hence an overall neutral cell is used. In case the core hole is not screened by an electron, a neutralizing background charge is introduced and the spurious effects henceforth can be minimized by the Makov and Payne approach [57].

The CLS are to be reported with respect to a reference BE. The choice of the reference BE depends on the physical case of interest. For example it can be that of a bulk atom of the same species in the same sample or

of a surface atom of the same species at another coverage from a different sample. Hence the CLS of an atom i with respect to reference atom j can be expressed by the following equation 2.7. The E^0 and E^0_{ref} are the same if they are the ground state energies of the same system and then in the ΔSCF method:

$$CLS_i = BE_i - BE_{j(ref)} \quad = (E_i^+ - E^0) - (E^+_{j(ref)} - E^0_{ref}) = E_i^+ - E^+_{j(ref)} \tag{2.7}$$

In the case of pentacene/Al(001) system, for $E^+_{j(ref)}$ we used the weighted average of the system energies with a full core hole on the 1s level of every inequivalent C atoms present in pentacene.

2.3 Near Edge X-ray Absorption Fine Structure Spectroscopy (NEXAFS)

Near Edge X-ray Absorption Fine Structure Spectroscopy (NEXAFS) also known as X-ray absorption near edge structure (XANES) is an extremely useful absorption technique in studying the electronic structure of materials and surface adsorbate properties by looking at the unoccupied states. In the case of molecular adsorption, it is possible to extract clear information regarding the orientation of the molecule on the substrate [58]. The NEXAFS π^* resonances give information about the out-of-plane and σ^* resonances regarding the in-plane orientations of the molecule.

Different from XPS, here the core electron is excited to an unoccupied orbital thereby making it feasible to probe x-ray absorption through de-excitation of the core hole (mostly by Auger decay) and emission of photo-electrons. To calculate the NEXAFS spectrum, one needs to compute the absorption cross section. This is given by the Fermi golden rule as a sum

of probabilities for making a transition from an initial state to an unoccupied final state per unit time through an interaction Hamiltonian [59]. The amplitude of the electronic transition involved in absorption is given by the electric dipole operator directed along the photon beam polarization. The main difficulty of any absorption cross section calculation lies in the solution of the Schrödinger equation for the initial and final states. The choice of the method used to solve the Schrödinger equation depends on the localized or delocalized character of final states. If the final state is delocalized, electron-electron interactions are weaker and DFT based single-electron approaches can be used.

According to the transition-state method devised by Slater [60], and extended by Janak [61], the excitation energy $h\nu$ is estimated as the orbital energy difference between two levels of a variationally determined (transition) state, with half an electron excited as given in equation 2.8.

$$h\nu = \epsilon_f^{n_i=1/2,n_f=1/2} - \epsilon_i^{n_i=1/2,n_f=1/2} \tag{2.8}$$

where ϵ_i, n_i and ϵ_f, n_f are the KS eigen values and occupation numbers of the initial i and final f levels respectively. The transition-state approach of Slater requires a state-by-state calculation which makes it impractical for generating a complete X-ray absorption spectrum for the systems considered here. This is obtained by using the transition-potential (TP) approach introduced by Triguero et al. [62] which is an approximation to Slater's [58]. The TP approach avoids the state-by-state calculations by simply removing half an electron from the final state resulting in the following equation.

$$h\nu = \epsilon_f^{n_i=1/2,n_f=0} - \epsilon_i^{n_i=1/2,n_f=0} \tag{2.9}$$

This approximation is good if the orbital character of the relaxed half-

occupied level is similar to the empty one. The spectrum is then obtained by diagonalising the Hamiltonian constructed by using the potential obtained from the orbitals with half a core hole [62]. This potential determines the excited electronic level or final state, a virtual orbital which is the eigenvector of the KS operator. Since the i and f states use the same orthogonal orbital set, the whole spectrum calculation is reduced to just evaluating the matrix elements between the KS orbitals corresponding to the core level (here C 1s) and the unoccupied states.

In this thesis we will present the XPS and NEXAFS calculated by using the XSPECTRA code in the QE distribution [63, 64, 65, 66]. This code calculates the absorption spectrum including both dipolar and quadrupolar matrix elements. The charge density calculated with one absorbing atom in the super cell is post-processed by the code. The all-electron wavefunctions are reconstructed using the PAW method as its implementation in the GIPAW code [66]. The presence of a full/half core-hole in the final state of the X-ray absorption process is simulated by using a pseudopotential for the absorbing atom with a full/half hole in the core state. From the self-consistent charge density, the X-ray absorption spectra are obtained using the Lanczos method and a continued fraction expansion [65, 59]. By this method, once the charge density is known, it is not necessary to calculate the empty bands to describe the very high energy features of the spectrum [65, 66].

2.4 Scanning Tunnelling Microscopy (STM) and Scanning Tunnelling Hydrogen Microscopy (STHM)

Scanning Tunnelling Microscopy (STM) is a powerful tool for determining the surface structure with atomic resolution, thanks to its inventors G. Binnig and H. Rohrer [67]. The working principle of STM is based on quantum tunnelling. When a tunnelling voltage (V_T) is applied between a scanning tip and a sample surface as the tip is brought very close to the surface, the electrons can tunnel through the vacuum gap between the tip and the surface. Both the tip and the sample should be conducting in order for the tunnelling to take place. The tip scans the surface in two dimensions, while its height is adjusted by a mechanical feedback arrangement to maintain a constant tunnelling resistance. The result is essentially a contour map of the surface. This mode of STM operation is called the constant current mode. There is also a second mode for STM operation called the constant height mode where the tip is maintained at a constant distance from the surface during the scanning procedure and then the resulting output image is an electron density/current map.

The most widely used and well-established theoretical method to obtain the STM images by simulation is the one put forward by J. Tersoff and D. R. Hamann in 1983, two years after the invention of STM [68]. The tunneling current in the Tersoff-Hamann approach as given in the following equation 2.10 is proportional to the surface local density of states (LDOS) at the Fermi level (E_F) at the position of the tip where the obtained image represents a contour map of constant surface LDOS. The tip is modelled as a locally spherical potential well considering only the solution with an s-type angular

momentum. This approximation is a useful way of parameterizing the effect of finite tip size. For the density of states at the Fermi level, the surface represents a potential barrier whose height is equal to the work function (ϕ). The tunnelling current is exponentially related to the vacuum gap in the case of planar tunnelling [69] which means that the current decays exponentially with the increasing distance between the tip and the sample surface. For a given tip position, the tunneling current is given by the following equation.

$$I \propto V_T \phi^2 D_t(E_F) R^2 \kappa^{-4} e^{2\kappa R} \times \sum_{\nu} |\Psi_\nu(\mathbf{r}_0)|^2 \delta(E_\nu - E_F) \tag{2.10}$$

where D_t is the density of states per unit volume of the probing tip, E_ν is the eigenvalue of the surface state Ψ_ν, $\mathbf{r}_0$ is the position of the centre of curvature and R is the radius of curvature of the tip and $\kappa = \hbar^{-1}(2m\phi)^{1/2}$ is the inverse decay length for wave functions in vacuum.

Scanning Tunnelling Hydrogen Microscopy (STHM) is a new technique introduced in 2008 by Temirov et al [70]. The application of this technique goes well beyond STM by allowing small amounts of hydrogen, H_2 between the tunneling tip and the sample and subsequently driving the tip-sample distance into the Pauli repulsive regime. Depending on the scanning parameters (such as the very small tunnelling voltage in the range of mV) one can attain a submolecular topographic contrast reminiscent of the corresponding skeletal formula of the compound [70, 71]. This technique is particularly useful where the conventional STM fails such as when a direct and simultaneous imaging of the guest atoms together with the molecular host matrix is required. This is quite challenging and has not yet been achieved, supposedly because imaging the molecular and atomic orbitals often requires different tunnelling parameters. So far, intercalated atoms were inferred only indirectly from the visualization of bonding channels between the molecule and

the dopant [72].

In this work we have also used the STM images simulated by using the Tersoff-Hamann approach to compare with the experimental STHM images [73]. The modeling of STM experiments by the Tersoff-Hamann formalism (LDOS at the tip position, strictly speaking at approx. 10 Å from the surface) is generally not enough to explain the high resolution which can be attained in STM experiments as discussed since [74]. The most common description of the process, which produces a good similarity to measurements achieving high resolution, is rather given by extending the Tersoff-Hamann approach to distances which are unrealistically much closer to the surface (typically, 2-5 Å). The way this higher resolution is attained in the experiments is not unique: tip states with specific symmetries, tip-sample interactions, adsorbate species, etc., as well as their possible combinations may be realized in tip processing. In the case of STHM the higher contrast is provided by adsorbing hydrogen to the tip, justifying comparison between the observations and the simulated data, which would be otherwise too much resolved in comparison to plain STM measurements. One should bear in mind that a single interpretation of how STHM works may not explain all cases: for example, the H_2 may be dissociated and enhance the p-character of the tip states [75]; or the H_2 molecule may interact with the sample and act as a transducer so that the tip responds more locally than a bare tip [71]. A comprehensive study on this sense would require testing a tip against a well studied reference surface [76], a purpose which is beyond the scope of the present work.

Chapter 3

Pentacene/Al(001)

3.1 Introduction

Pentacene ($C_{22}H_{14}$) is a well known organic small molecule which was first synthesized by Mills and Mills in 1912 [77]. And in 1961 Campbell and coworkers reported the structure of pentacene molecular crystals for the first time [78]. It acts as a p-type organic semiconductor in its intrinsic state with an ionization potential of 6.58 eV [1] and exhibits a very high melting point [9]. It has shown temperature-independent highest hole mobility (35 $cm^2/V-s$) and electron mobility (1.5 $cm^2/V-s$) which is a very interesting property for applications in fast switching devices [79, 80, 81, 82, 83]. In terms of processing, pentacene molecules are cheap and very easy to process and they also enable the use of flexible substrates. Several experimental and theoretical investigations were focused on the adsorption of pentacene onto a few metal surfaces for contact fabrication which were of potential interest. And these studies have shown that significant deviation from a conventional planar adsorption geometry was reported only for the Au(110) surface, with mixed edge-on/planar phases [84]. In all other cases only a

minor bending of the molecular backbone, with the central ring closer to the surface was reported for this adsorbate on Au(111) [85] and Cu(001) [20] and Cu(110) [21] surfaces. An asymmetric adsorption along the long edge of the molecule was determined for Co islands on Cu(111) [86]. "Several studies point to a significant mixing of the molecular and substrate electronic states at the interface, spanning from the simple broadening of the unoccupied π^* resonances on weakly interacting Au surfaces [84] to the filling of the lowest unoccupied molecular orbital (LUMO) on more strongly interacting surfaces like Cu(001) [20, 87], Cu(110) [21], and Cu(111) [88]. The filling of the LUMO may even show a dependence on coverage as for pentacene/Ag(110) [19] that is a phenomenon in common with other adsorbed molecules [89, 90]"[1].

Aluminum is a strongly reactive substrate metal with nearly free s, p-electrons and is of potential interest for Si-free electronic devices. Previous studies have shown that pentacene coupled to aluminum results in the formation of Schottky barrier at their interface which property could be utilized to fabricate devices like Schottky diodes and organic thin film transistors (OTFTs) [91, 92, 93, 94]. The interaction between pentacene and aluminum is also important in organic solar cells [95] and memory devices [96]. Despite the aforementioned general interest, only a few theoretical investigations related to the adsorption and first layer growth on aluminum surfaces (without taking into account the long-range dispersion forces) were conducted [97, 98]. Due to the extreme ductility of aluminum crystals, the difficult in the preparation of well ordered surfaces may have hampered attempts to investigate the interface of this metal with organic semiconductors [63]. As a matter of fact, there are no atomically resolved microscopic investigations of adsorbates on Al crystals reported till date other than the fundamental studies of

[1]Taken from Baby et al. Ref. [63]

Ertl and coworkers [99]. We study the structural and electronic properties of pentacene/Al(001). Discussion of the results from our two papers: Ref. [63] and [64] are included here.

3.2 Experimental Interface Morphology

The experiments were carried out by Dr. Luca Floreano and his group at the ALOISA beamline of ELETTRA synchrotron, Trieste, Italy. The deposition of pentacene was monitored in real time by Reflection High Energy Electron Diffraction (RHEED) [63]. The RHEED pattern appears to be incommensurate with the substrate, and it is characterized by the presence of major quasi-4-fold streaks ($\sim$1/4 and $\sim$3/4) aside the integer peaks, along both the [100] and [110] directions, as can be seen in figure 3.1(a) for 1 ML pentacene/Al(001). The streaky nature of the diffraction pattern suggests the presence of terraces and other surface irregularities. The emergence of a half-integer ($n/2$) peak was not observed at whatever coverage and sample temperature. RHEED taken at 1 ML along the [100] direction eventually displays two additional faint streaks close to the seven-fold positions (3/7 and 4/7), as seen in figure 3.1(a); however, the emergence of the 1/7 and 6/7 peaks in either directions was never observed so that a $\times$7 periodicity cannot be deduced. "From comparison with STM images taken slightly before completion of the monolayer (where mostly the quasi-4-fold streaks are detectable), we can associate this RHEED pattern to the interplay between the correlation among the molecules and a local quasi-4-fold substrate reconstruction induced by pentacene. The latter reconstruction partly extends also to uncovered terraces, as shown in figure 3.1(b), where images taken with atomic resolution display a rippling of the Al rows across the [100] direction,

Figure 3.1: (a) RHEED pattern at 1 ML pentacene/Al(001) as taken with the [100] surface direction oriented in the scattering plane; arrows indicate the quasi-four fold streaks aside the substrate integer Bragg's peaks. (b) STM picture form an uncovered albeit reconstructed portion area after deposition of $\sim$ 0.8 ML pentacene; a regular 1.6 nm spacing is detected across the rippled atomic rows (-0.8 V; 50 pA). Taken from Baby et al. Ref. [63].

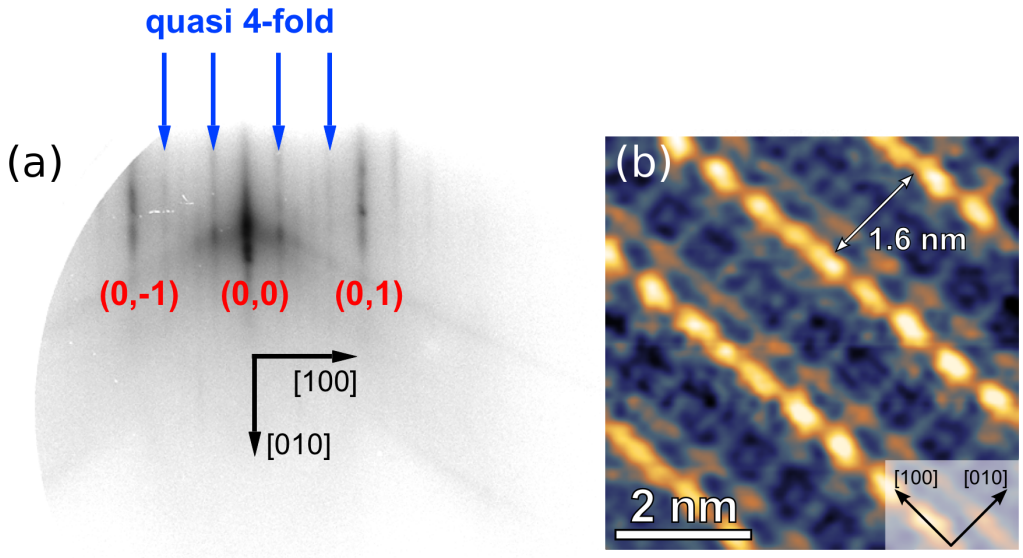

Figure 3.2: (a) STM picture taken at ~ 0.8 ML coverage after annealing to 450 K (-1.0 V; 50 pA). Three adjacent molecular stripes parallel to the [100] direction are visible. An uncovered portion of the substrate reconstruction can be detected in the upper part of the image. (b) A scheme of the molecular accommodation within the substrate reconstruction. Taken from Baby et al. Ref. [63].

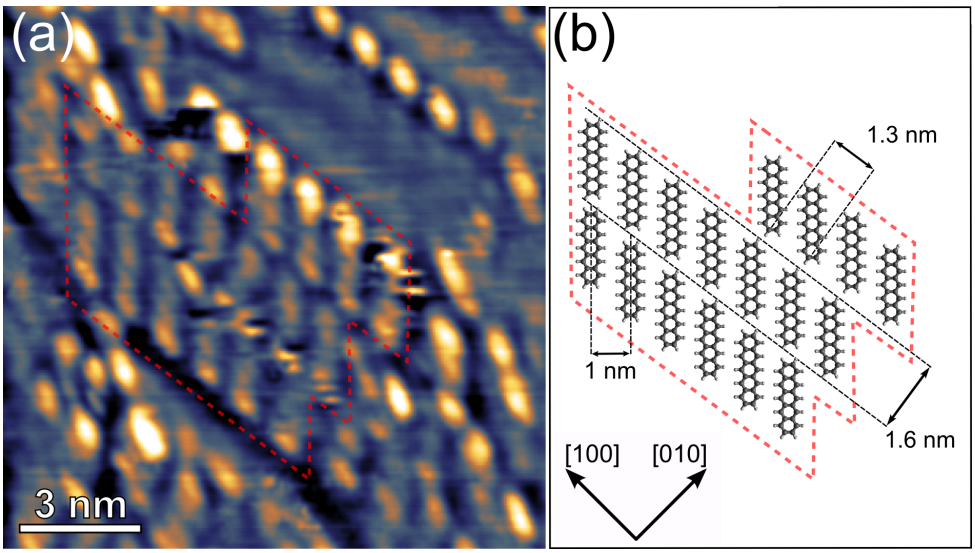

with a measured corrugation of 30 pm. A modulation of the STM intensity is also observed along the Al rows, but we have not been able to correlate it with a well-defined periodicity in the RHEED patterns"[2].

"The STM image of deposited pentacene/Al(001) close to the saturation coverage is displayed in figure 3.2(a). We can see that the surface is full of elongated features with lengths compatible to that of pentacene ($15 - 16$Å). No long-range ordered domains could be detected (consistently with the limitations of the clean surface ordering) by the experimentalists. It has to be stressed that the moderate surface ordering limited a quantitative STM anal-

[2]Taken from Baby et al. Ref. [63]

ysis. The molecules are aligned side-by-side forming parallel stripes oriented along the [100] direction with the major axis along the [110] direction. Since the width of these parallel stripes corresponded to that of the substrate reconstruction, the experimentalists deduced that the $\sim$ 1.6 nm wide ripples of the reconstructed Al substrate accommodates pentacene, as schematically depicted in figure 3.2(b). Most of the molecules are observed to have brighter molecular ends implying a structural origin (i.e., conformational change) as the STM imaging mode used here is constant current mode. Unfortunately the experimentalists were not able to determine the registry of the molecules with the substrate. They measured the side-by-side period between the adjacent molecules within a stripe to be $\sim$ 1.3 nm along the [100] direction (see Figure 3.2(b)). A period of $\sim$ 2.8 nm (twice as long), was measured for the 7-fold RHEED streaks along [100] which indicates the presence of two inequivalent molecules per cell. Beyond the first wetting layer a gradual smearing of the RHEED pattern is obtained, which implies the formation of the disordered clusters which can be further confirmed from the weak dependence of photoemission measurements on coverage (not shown here) "[3].

3.3 Computational Method and Results

The DFT based calculations of pentacene adsorbed on Al(001) system are done using the Quantum-ESPRESSO package (see Appendix A for further information) [66]. The generalized gradient approximation (GGA) as proposed by Perdew, Burke, and Ernzerhof (PBE) [46] is used as the exchange correlation functional. Plane waves are used along with the ultrasoft pseudopo-

[3]Adapted from Baby et al. Ref. [63]

tentials (PPs) (generated with the Rappe, Rabe, Kaxiras, and Joannopoulos scheme). A planewave cutoff of 27 Ry and charge density cutoff of 108 Ry are adopted for relaxation and total energy calculations. The aluminum (001) substrate is constructed in the slab model with three layers of atoms, fixing the bottom two layers during all relaxation runs. The slab was constructed in a rectangular shape of size 8×5 in order to simulate the adsorption of isolated pentacene molecules. A vacuum space of 20 Å separates the adjacent slabs. "The surface Brillouin zone is integrated using a Monkhorst-Pack [100] special 2×3 grid of k-points and Methfessel-Paxton smearing [101] with a broadening of 0.02 Ry, eventually thickened to 6×10 in evaluating electronic density of states. Pentacene is deposited only on one side of the slab, with one molecule every unit cell of aluminum, and its coordinates are optimized together with those of the first layer of aluminum. Test calculations for the most stable configuration are run for slab thickness up to 10 layers, reconfirming the results. The vdW interactions between the molecule and the surface are taken into account by adding semiempirical London dispersion forces in the Grimme approach [47] and excluding them within the Al atoms"[4].

3.3.1 Structure of the adsorbed system

"In my calculations single pentacene molecules with the long molecular axis aligned along the [110] direction were considered (as suggested by experiments). Pentacene was placed with its central ring on the high symmetry sites of the ideal Al(001)surface, namely top (T), hollow (H), and bridge (B), together with (B') and (H') (explanation about these two sites follow) and these configurations were optimized [63]. The resulting geometries are

[4]Taken from Baby et al. Ref. [63]

reported in figure 3.3. The long molecular axis of pentacene is perpendicular to the Al-Al bridge at B and parallel at B' sites. We also tried configurations where the molecules are tilted around their long axis but they returned to a planar configuration (not discussed here). The adsorption energies obtained for all these configurations after optimization are reported in table 3.1 together with the main structural information. The adsorption energy is calculated using equation 3.1.

$$E_{ads} = E_{sys} - E_{sub} - E_{mol} \tag{3.1}$$

where E_{sys} is the total energy of the optimized system, E_{sub} is the energy of the bare substrate, and E_{mol} is the energy of the free molecule. The deformation energy E_{def} defined as the energy spent to elastically deform the molecule in gas phase is given in the last column of table 3.1. Table 3.1 shows that the B configuration is the most stable one, with a binding energy 0.7 eV lower than that in all the other cases which show similar values of adsorption energy and distance from the surface but with negligible bending.

So let us first look at what happens in the B configuration. The two central C atoms of pentacene with inter-atomic distance (C1-C1') of 2.82 Å matches almost perfectly the Al atoms underneath (with the bridge $d_{\text{Al-Al}}$ distance of 2.86 Å). This allows for a bending of the pentacene molecule as a result of the strong interaction between the C1-C1' atoms with the Al atoms lying below them (which is discussed in a very detailed manner in the next section), leading to V-shaped molecules. The V-angle being $\alpha = 155°$, the central carbon atoms are much closer to the surface compared to the other cases, with perpendicular coordinate of $z = 2.16$ Å and a distance to the nearest Al atoms of only 2.20 Å [63]. Molecular terminations lie about $\Delta z = 1.35$ Å higher. Such a molecular bending costs an elastic deformation energy,

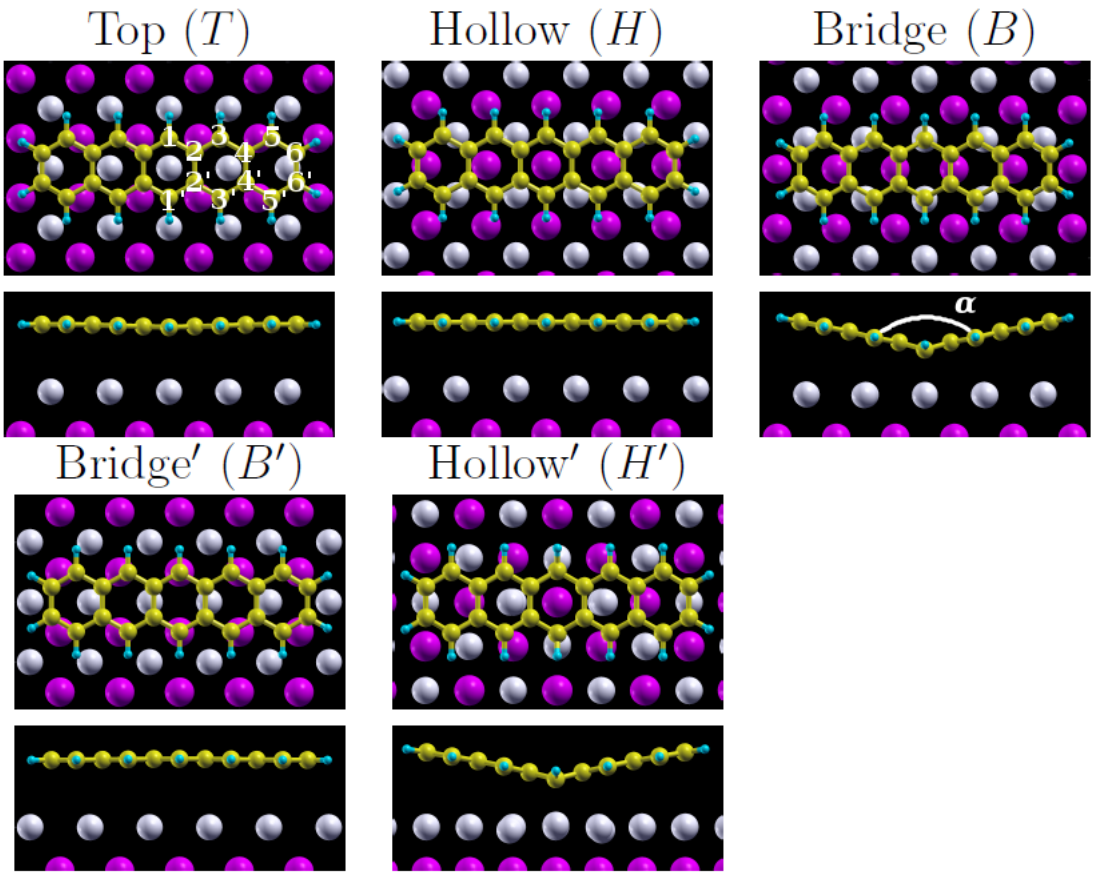

Figure 3.3: Top and side views of adsorption configurations of pentacene/Al(001). Brighter (silver) and darker (pink) spheres mark positions of Al atoms in the first and second layer, respectively. Notice the different orientation for the H' case. The numbering of atoms is shown in the T panel. Taken from Baby et al. Ref. [63].

Table 3.1: Adsorption energies (E_{ads}), height of the central (lowest) carbon atom from the surface (z), height difference between the peripheral and central and carbon atoms (Δz), and deformation energy (E_{def}) for different configurations depicted in Fig. 3.3. Taken from Baby et al. Ref. [63].

Site	E_{ads} (eV)	z (Å)	Δz (Å)	E_{def} (meV)
T	-1.50	3.09	0.13	0.04
H	-1.42	3.19	0.01	0.03
B	-2.20	2.16	1.35	1.35
B'	-1.37	3.26	-0.05	0.01
H'	-1.78	2.25	1.24	1.38

$E_{def} \sim 1.35$ eV for the free molecules. A surface buckling of -0.04 Å is noted for the Al atoms lying below C1 and C1'. Usually for all planar molecules the adsorption mechanism is physisorption with a potential energy surface weakly dependent on the adsorption site. But in this particular case the direct anchoring of the central C atoms to the specific surface atoms matching their distance results in a site-specific stronger adsorption. The situation is ideal for the B configuration for this kind of interaction to occur. But additionally it can also be realized when the H-site molecule is azimuthally rotated by 45° around the perpendicular axis (*i.e.,* with the long molecular axis parallel to [100]). This case denoted as H', shown in figure 3.3 also results in a V-shaped molecule. In this case the interaction between the central C atoms and two Al atoms below results in bringing these Al bridge atoms closer (originally at a distance of 4.04 Å from each other) to 3.84 Å upon adsorption. This results in the adsorption energy of -1.78 eV which is significantly larger than that for the planar cases, but smaller in magnitude

than that for the B site which remains the most stable configuration. The C-Al distance (2.19 Å) for the H-site is very similar to that in the B case like the other structural parameters also reported in table 3.1. We conclude thus that B and H' are the only possible configurations for comparable C1-C1' and Al-Al distances for pentacene on Al(001), and that other adsorption sites with long molecular axis along [100] are expected to result in a planar molecular geometry and a lower adsorption energy [63]. The surface reconstruction and its inhomogeneities are most probably increasing the reactivity of Al at some surface regions of the surface such that a direct molecular anchoring at a couple of metal atoms therein would be enhanced. I have considered only the ideal Al(001) in the simulations and investigating the adsorption on the reconstructed Al surface would require a reliable atomistic model of the latter. As this was not available from the experiments it was not simulated and is also beyond the current understanding of this system.

Now I will discuss the role played by the vdW interactions in this system. Usually vdW interactions were known to shorten bond lengths and stabilize adsorption energies [102]. But here, these dispersion forces has a fundamental role to play in obtaining the observed V-shaped molecular bending which required a direct anchoring of C1 to the underlying Al and would not have occured if there were no attractive forces between the aromatic rings and the surface. This was confirmed by the calculations that I performed without including these interactions i.e. only with PBE as in refs [97] and [98]. And this results in very weak adsorption strength, clearly underestimated and the specific V-shape is not obtained eventually. The maximum deformation reported at the B site was obtained by the local density approximation (LDA), which is however missing the dispersion forces, was $\Delta z = 0.74$ Å [97]. However, the molecule did not display the V-shape reported in this work. As a

comparison, a clear U-shape deformation was determined for pentacene on Cu(110) [21].

The treatment of dispersion forces within DFT is a delicate issue, and the work towards an approach with optimal accuracy and cost is still a very active field of research. I remark that the difference in the molecular shape between Al(001) and Cu(110) adsorption is independent of the method chosen, namely the vdW density functional (vdW-DF) [103] for Cu(110) [21] and the Grimme correction [47] for Al(001) (this work). This was confirmed by my additional calculations applying the PBE+Grimme approach to the pentacene/Cu(110) system, obtaining U-shaped molecules in close agreement with those of Ref. [21] hence demonstrating that the different theoretical descriptions do not affect the results (not shown here). It is noticeable that at the same cost of a standard GGA calculation, the Grimme approach provides a reasonable level of accuracy, while the vdW-DF method commonly overestimates molecule-surface distances [88, 104]. Finally, I also confirmed that the V-shape bending of pentacene obtained on the three layer thin Al(001) slab considered in my calculations is fully convergent with respect to the slab thickness (upto 10 layers)"[5].

3.3.2 Origin of the V-shape

The V-shape obtained for the adsorption of pentacene on Al(001) is a very interesting feature not reported before elsewhere and the rationale for this behavior is examined in detail in this section. "Bending at the central position is in agreement with the findings about the reactivity of pentacene and related molecules [105], as described in terms of the molecular aromaticity (defined as the ability of the π-electrons to delocalize above and below the

[5]Adapted from Baby et al. Ref. [63]

plane of cyclic molecules resulting in their extra stabilization [106, 107]). If we consider benzene the most aromatic molecule as an example, as more rings are added to it, the electronic density within the molecule rearranges in such a manner that it is largest for the central ring (hence highly reactive even if more aromatic) and decreases towards the outer ones [108, 109]. Taking part in reactions through the most aromatic central ring is convenient for the molecule as the activation energy barrier is lower [110]. Furthermore the HOMO coefficients are highest for the central carbon atoms in acenes and decrease towards the outer ring ones [110]. Other studies related reactivity to the ring current showing that this is highest for the central ring in the case of pentacene and also the highest proton chemical shift is found for the hydrogen atoms attached to the central carbon atoms in the case of acenes [111]. All these results support the reactive nature of the central carbon atoms in pentacene [64]. In agreement with such properties our results in the previous section demonstrate that V-shaped pentacene bonds to the Al atoms underneath through the two central carbon atoms of the innermost phenyl ring as the distance between them becomes comparable to the Al-Al one. An analogous bending was reported for pentacene dimers in the gas phase [105], where sp^3-hybridized C atoms at the center of pentacene directly bond to those of a facing molecule, with $d_{\mathrm{CC}} = 1.60$ Å and even smaller V-angle $\alpha = 115^\circ$ than that of our calculations"[6].

3.3.3 Effects of V-shape on Bond Length

Now we are in a position to understand the outcomes of this structural bending on the electronic properties. First of all, we look at the bond lengths. "The V-shaped molecular deformation influences the carbon-carbon bond

[6]Taken from Baby et al. Ref. [64]

lengths of adsorbed pentacene. They are reported in table 3.2 in which the bond lengths of the free molecule in the gas phase (g) is compared to that of the molecule adsorbed flat and bent at T and B sites, respectively [64]. A common trend is found while moving from the free molecule to the flat and to the bent adsorbed one, as they keep either increasing or decreasing, conversely decreasing or increasing the π-character of those bonds [112]. Due to the strong coupling between C1 and the underlying Al atom at B site the C1-C2 experiences the highest variation in bond length, which increases by 0.07 Å from g to B. Such an elongation occurs because the C1 orbital modifies from sp^2 to sp^3 hybridization, which results in a displacement of the valence electron density of C1 from the C1-C2 bond to the newly formed C1-Al one, as recently discussed for self assembled monolayers [113]. This further affects the delicate electron density balance within the molecule, i.e. while the C1-C2 bond length increases (decreasing the π-character), the C2-C2' bond length decreases (increasing the π-character) at B site. This kind of rearrangement in the electron density reduces the aromaticity of the central carbon ring of pentacene but in a smaller way than that for bending through the outer rings [110], as discussed before. Furthermore shorter C2-C2', C4-C4' and C6-C6' bond lengths (on an average of about 0.02 Å) are observed moving from second to fourth column of table 3.2 additionally indicating that the molecule shrinks along the short molecular axis. On the contrary an increase in the length of the molecule is observed along the long axis for the B configuration hinting a slight weakening in the coupling of outer atoms with respect to those of pentacene in gas phase. Summarizing, the differences between the bond lengths in the two directions reduces [64]"[7].

[7]Taken from Baby et al. Ref. [64]

Table 3.2: Carbon-carbon bond lengths for free pentacene (g) and for pentacene adsorbed at top (T) and bridge (B) sites. See Figure 3.3 for the numbering of C atoms. Taken from Baby et al. Ref. [64].

C-C	g (Å)	T (Å)	B (Å)
C1-C2	1.400	1.408	1.466
C2-C3	1.411	1.409	1.396
C3-C4	1.390	1.400	1.420
C4-C5	1.429	1.423	1.414
C5-C6	1.368	1.375	1.383
Average	1.400	1.403	1.416
C2-C2'	1.458	1.454	1.428
C4-C4'	1.453	1.448	1.428
C6-C6'	1.427	1.422	1.410
Average	1.446	1.441	1.422

3.3.4 Ground State Electronic Properties and Charge Transfer

More insights on the electronic properties can be gained in this section. "For the same we compare the B configuration to the T one, which is an example of the less interacting and hence almost planar pentacene. The energy levels of the adsorbed system show a clear dependence on the adsorption configuration. To this purpose, the states with a strong molecular character are emphasized by projecting the DOS of the full system onto the molecular orbitals called the molecular orbital projected density of states (MOPDOS) (see Appendix C). Such projections are displayed in figure 3.4 for T and B configurations, showing a clear dependence of the HOMO and LUMO on the adsorption configuration. A large difference between the HOMO and the LUMO resonances and a reduction of their gap can be observed moving from T to B. In addition, both HOMO and LUMO orbitals broaden and shift to lower energies for B-site adsorption. In particular for the LUMO an appreciable filling was observed as this state displays an energy range as large as 4 eV with its main peak more than 1 eV below the Fermi energy level. Conversely, the energy position of other states like the HOMO-1 and LUMO$+1$ is practically unaffected. The different behaviour can be accounted for by the strong weight of HOMO and LUMO on the $2p_z$ states of the central C atoms ($\sim$ 25%), while HOMO-1 and LUMO$+1$ vanish along the short molecular axis and they have no weight on the central carbon atoms [64]. Significant filling of the LUMO is obtained as observed in other systems [21, 20, 87, 88, 19, 89, 90], although the large V-shape bending observed here was not previously reported. It is known that the LUMO of the adsorbed molecule should lie closer to the Fermi level of the metal substrate for efficient electron injection from the metal to the organic semiconducting

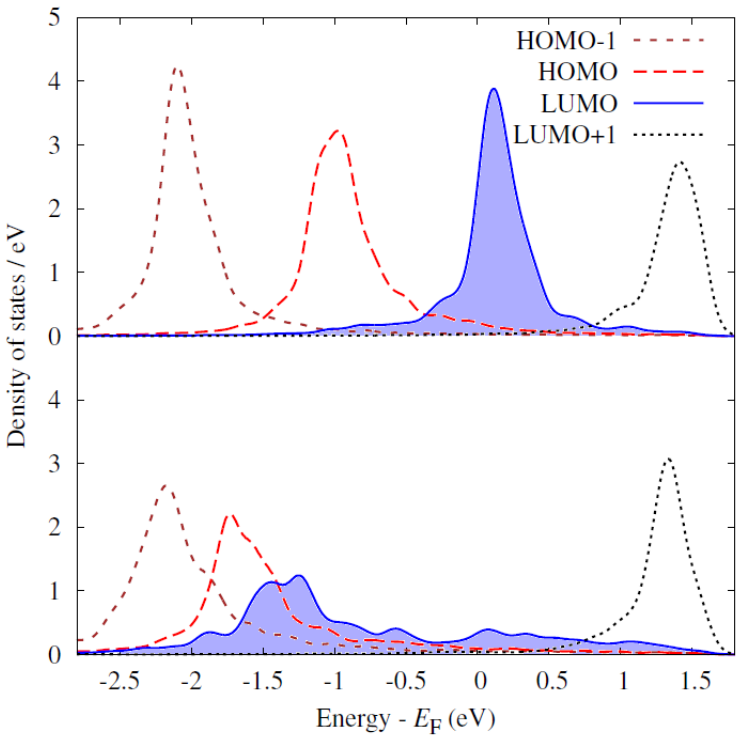

Figure 3.4: Molecular orbital projected DOS of pentacene/Al(001) at T (upper panel) and B (lower panel) sites respectively. Adapted from Baby et al. Ref. [63].

molecule [15]. Hence, the calculated energy position of LUMO indicates that pentacene acts as a p-type semiconductor when paired with aluminum.

Let us now quantify the interactions taking place between the molecule and the metal substrate in terms of charge transfer upon adsorption. The isodensity plots showing the three dimensional charge rearrangements for pentacene at B and T sites are shown in figure 3.5, which can be defined using the equation 3.2.

$$\Delta\rho = \rho(total) - \rho(adsorbate\ layer) - \rho(substrate) \tag{3.2}$$

where $\rho(total)$ is the total charge of the combined system, $\rho(adsorbate\ layer)$

is that of the non-interacting pentacene monolayer and $\rho(substrate)$ of the non-interacting Al substrate (all atoms are fixed at the same positions as in the combined system). Red colour indicates regions of higher electron density and blue ones of lower density. For B site adsorption, at an isovalue of $\Delta\rho = 0.005$ e/Bohr^3 we can clearly observe in figure 3.5(c) accumulation of electron density between the two central carbon atoms (C1 and C1') and the two Al atoms underneath them confirming the bonding of the molecule at that specific site. At a lower isovalue (0.002 e/Bohr^3), as depicted in figure 3.5(a, b) we can see that such charge originates from the electronic density depletion in the close proximity of the C-Al bond, with overall electron transfer from the surface to pentacene. An excess electronic charge of ΔQ = 0.56 e is calculated on the adsorbed molecule, by means of Löwdin charge partitioning scheme [114, 115], much larger than those (0.15 electrons at most) reported by calculations with LDA and PBE functionals [97, 98]. One also observes (see the red regions in figure 3.5(a, b)) electron accumulation between the atoms C3, C3' and the surface, while other C atoms at larger distances are clearly less interacting with the surface. Intramolecular charge displacements in figure 3.5(a) show electronic charge accumulation between the atoms C3-C2-C2'-C3'. It has to be stressed that at the same isovalue, no charge restructuring is visible for the flat molecule at the T site and hence a lower isovalue of 0.001 e/Bohr^3 is chosen in figure 3.5(d) to plot a much less localized charge displacement amounting to ΔQ = 0.20 e [64].

The structural change in the V-shape of adsorbed pentacene induces alterations in the molecular orbitals which are best perceived by looking first at the gas phase molecule, but with the same geometry as in the B-site. In particular, the Kohn-Sham eigenvalues for bent and flat molecules are compared in figure 3.6. One of the major features emerging is the reduction

Figure 3.5: (a) and (b) Side views of the isodensity plot showing the bond charge of pentacene at B-site for an isodensity value = 0.002 e/Bohr^3 (red regions: high electron density and blue regions: low electron density), (c) pentacene at B-site for an isodensity value of 0.005 e/Bohr^3, (d) pentacene at T-site for an isodensity value of 0.001 e/Bohr^3. Taken from Baby et al. Ref. [64].

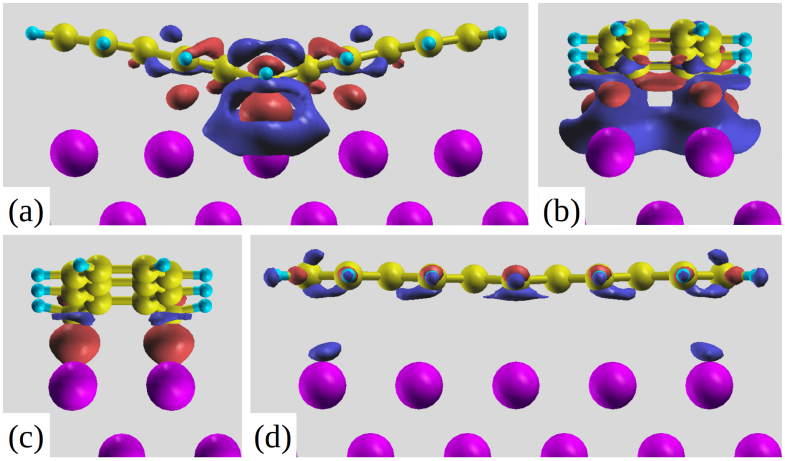

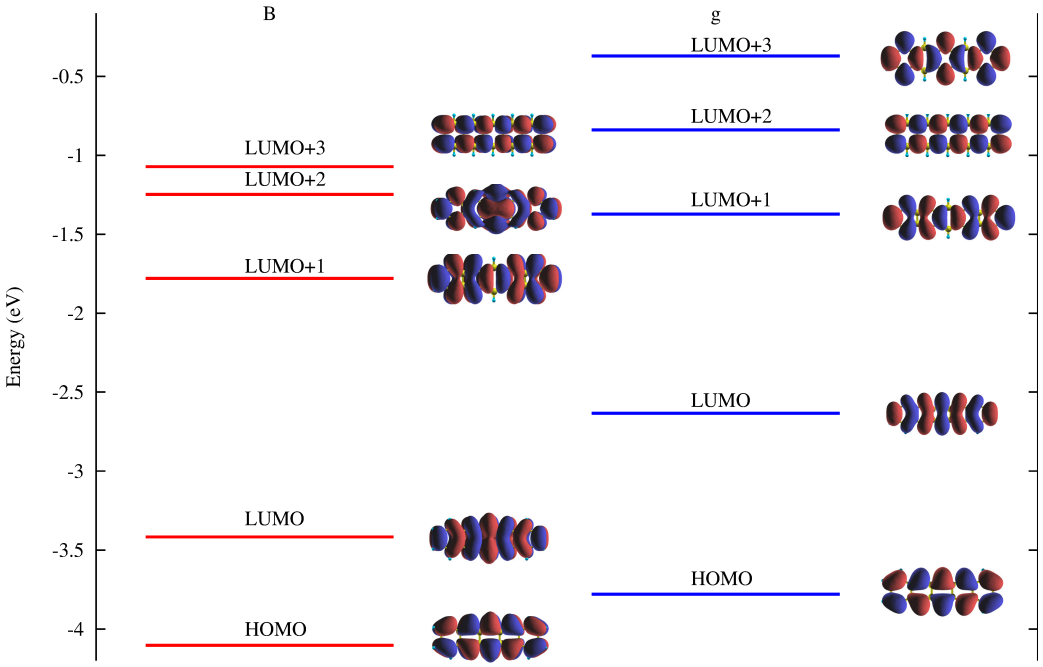

Figure 3.6: Comparison between the Kohn-Sham eigenvalues for V-shaped free pentacene with coordinates extracted from the bridge site adsorption (B) and gas phase (g) pentacene. The corresponding orbital wave functions are also shown for each case. Taken from Baby et al. Ref. [64].

in the HOMO-LUMO gap of the free molecule by 0.5 eV which decreases further for adsorption at B site due to electron transfer. Additionally, one observes that the orbital corresponding to the LUMO+3 in the undistorted molecule is stabilized with the V-shaped distortion in order to become the LUMO+2. Pentacene does not show this kind of large bending and huge charge transfer on any other metal surface reported to date [21, 85]"[8]. In the following sections I will discuss the experimental and simulated experimental results of XPS, NEXAFS and STM.

[8]Taken from Baby et al. Ref. [63] and Baby et al. Ref. [64]

3.4 XPS

The XPS spectrum is computed in terms of the core level shifts (CLS). Here, the CLS of a C atom i is defined as the difference between the total energy of the system in the presence of a full core hole on the 1s level of atom i and the weighted average of the system energies with a full core hole on the 1s level of every other inequivalent C atom taking into account their multiplicity, as given in equation 3.3 [116, 117].

$$CLS_i = E(PP_i^{fch}) - Weighted\ Average\ of\ E(PP_j^{fch}),\ i \neq j \qquad (3.3)$$

For this purpose carbon PPs with full core hole in the 1s orbital was used, requiring a higher plane wave cutoff of 59 Ry and charge density cutoff of 320 Ry. As we are using pseudopotentials, only relative binding energies are accessible. As already mentioned in Section 2.2, the electrons from the metal eventually neutralize the core hole in the adsorbed molecules and so a globally neutral cell was used. This also results in CLS computed with reference to the Fermi level of the substrate, similar to that obtained in the experiments [56].

In figure 3.7 the core level C 1s photoemission spectra (XPS) obtained by experiment, and by simulations for free undistorted pentacene and pentacene adsorbed at T and B sites are plotted. "Calculated initial state binding energies are indicated as vertical bars with height proportional to the multiplicity of the inequivalent carbon atoms (see figure 3.3). These vertical bars when broadened (here with pseudo-Voigt profiles having 0.52 eV Lorentzian and 0.36 eV Gaussian full width at half maximum) determine the simulated XPS spectra reported in figure 3.7. Since the absolute energy values are not accessible the simulated spectra are aligned to the experimental ones. The C 1s CLS spectrum computed in the gas phase [58], figure 3.7(a), is already able to

capture the main features of the experimental result for adsorbed pentacene [64]. When we consider pentacene adsorbed on Al(001) at the T-site, figure 3.7(b), the agreement actually worsens as the spectrum becomes too broad. Conversely, a good agreement is eventually observed for V-shaped pentacene adsorbed on the B-site, see figure 3.7(c), where the CLSs are smaller, further supporting the structural model [64].

The differences in the spectra seen in figure 3.7 can be understood stepwise as follows. When the molecule is adsorbed almost undistorted on the T-site, it may be affected by the surface coupling through several effects [118]. First, the full molecule is subjected to an effective potential due to the Al surface which influences similarly all atoms in the planar configuration and results in no net CLS. Second, the surface electrons screen the perturbation of the core hole, which is at the same distance in all cases resulting in a net electron transfer, which may induce changes in the CLS. This effect can be estimated by performing additional simulations for the free undistorted molecule to calculate the shifts in binding energies as a function of a given uniformly distributed excess electronic charge. The presence of such an excess electronic charge results in a more negative shift of the binding energy for atoms C1, C3 and C5 and a more positive one for the C2, C4 and C6 energies, providing a broader spectrum in the charged molecule case (not shown here) than in the gas phase neutral one. In particular, the C1-C2 binding energy difference amounts to 0.70 eV in the gas phase for neutral molecules and increases to 0.76 eV (0.84 eV) with 0.2 (0.5) additional electrons, in qualitative agreement to the value of 0.86 eV computed at the T-site. Indeed, comparing figure 3.7(a) and (b) we point out that the excess charge is unevenly redistributed in the molecule i.e. more electron density around C1, C3 and C5 and less around C2, C4 and C6, see also the LUMO amplitude

Figure 3.7: Experimental XPS spectrum for pentacene/Al(001) compared with the simulated C 1s photoemission spectra of (a) free pentacene, g and of pentacene on Al(001) at (b) T and (c) B sites. Simulated spectra are convoluted with pseudo-Voigt profiles with 0.52 eV Lorentzian and 0.36 eV Gaussian full widths at half maximum and offset by a constant (see the dashed blue line), the individual contributions from the six inequivalent carbon atoms are shown as vertical bars. Taken from Baby et al. Ref. [64].

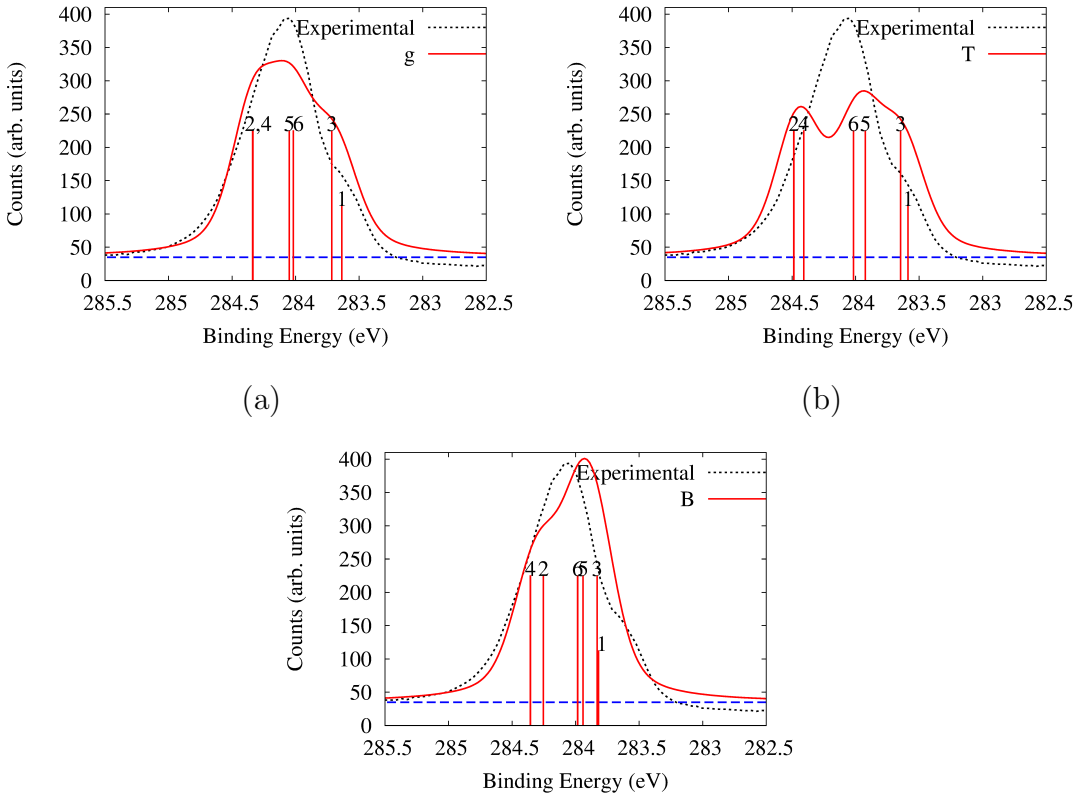

from figure 3.6 [64]. This reduces/increases the binding energy of $1s$ electrons in the first/second group of atoms, respectively [118].

This simple argument alone cannot explain the narrowing of the spectrum as we move from T to the B-site, where charge transfer upon adsorption is higher but the C2-C1 binding energy difference amounts to 0.43 eV only (0.54 eV for C4-C1). Here the additional effect exists that the potential of the aluminum surface experienced by the various carbon atoms, is not constant anymore as the C atom heights differ by up to 1.35 Å. However, a non monotonic dependence on distance is observed, as a similar variation with respect to C2 is computed for C1 and C3 which are at shorter and longer heights respectively. Hence, the variations in screening offered by the system for the hole at the various sites must play an important role. To visualize such variations, the screening charge following the C 1s level ionization, was evaluated, which is defined by the following equation 3.4 [64].

$$\Delta\rho^* = \rho(Pentacene^{fch}/Al) - \rho(Pentacene/Al) \tag{3.4}$$

where $\rho(Pentacene^{fch}/Al)$ is the total charge of the combined system with a full core hole on the selected C atom, and $\rho(Pentacene/Al)$ is that of the combined system in its ground state. The same is compared in figure 3.8 for the T and B sites, in the presence of a full core hole on atoms C1 and C2. We may observe that the screening charge at the T-site is similar for the two atoms C1 and C2 (figure 3.8(a-f)), when seen from the excited atom, and that the largest charge displacements are localized in its proximity. Conversely, $\Delta\rho^*$ for the molecule at the B-site (figure 3.8(g-l)) extends throughout the molecule as it also involves large contributions from the π system polarizing towards the surface. Note in particular the region of electron depletion (blue coloured) that is observed in figure 3.8(h, i) just above the Al atom located below the $1s$-excited C1. Such a depletion corresponds to a reduction of the

C1(C1')-Al(Al) bond as a result of the retraction of the bonding electronic charge into the molecule in order to screen the core hole (compare figures 3.5(c) and 3.8(h, i)). This is absent in figure 3.8(k, l) for excitation on C2. Hence, a larger destabilization of adsorption is expected when the core hole is present in C1 than in C2. Therefore the presence of core hole reduces the binding energy of C2 and increases that of C1. This is in agreement with a reduction in the difference between their core level binding energies, thereby determining a narrower spectrum for B site adsorption as seen in Figure 3.7(c) and compensating the effects of electron transfer [64]"[9].

3.5 NEXAFS

NEXAFS spectra are simulated using the XSPECTRA code in Quantum-ESPRESSO [59, 65]. The half core-hole with the transition-potential approach introduced by Triguero et al. [62] as discussed in Section 2.2 is adopted here and hence the calculation is performed with a carbon PP containing half a core hole in the C 1s orbital. "Such calculations can reproduce the main features in the spectral profiles [58, 119] while more refined approaches [120] allowing for a detailed analysis are difficult or unfeasible to implement for large systems and those systems with a continuous spectrum. To analyze the simulated NEXAFS spectrum of pentacene/Al(001) it is convenient to consider first a molecule in the gas phase but retaining the V-shaped geometry as in figure 3.6 [64]. In particular, let us focus on the transitions to the lowest lying LUMO+i states for the different C atoms with π^* symmetry, which characterize the low-energy part of the spectrum. The corresponding spectrum for photon electric field along the z-direction

[9]Taken from Baby et al. Ref. [64]

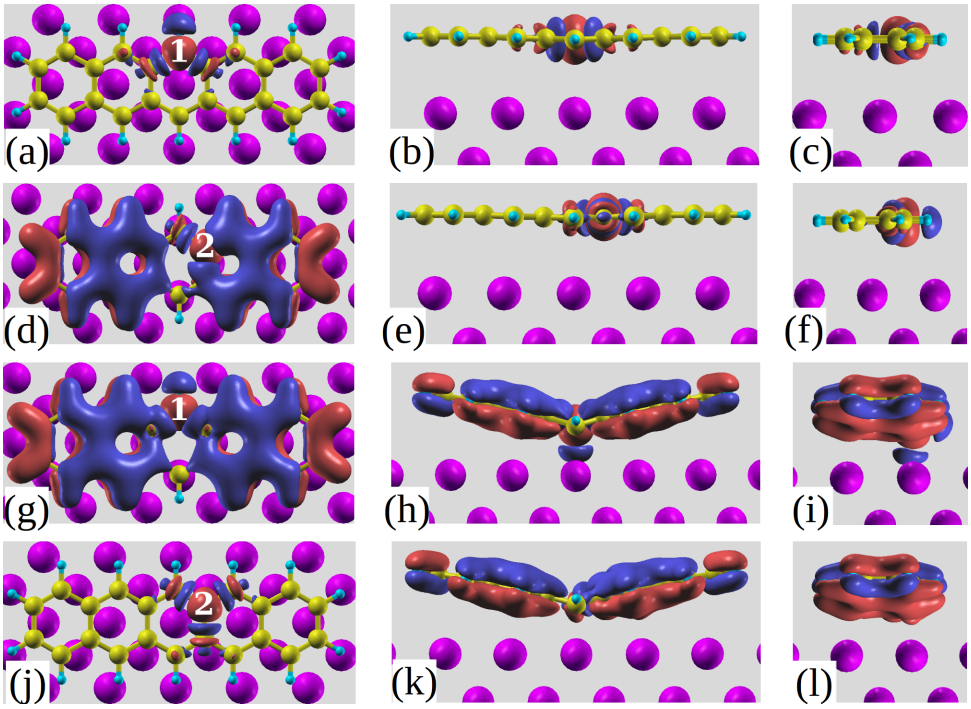

Figure 3.8: Top and side views of the screening charges in the presence of a full core hole on (a), (b), (c) C1 at T-site; (d), (e), (f) C2 at T-site; (g), (h), (i) C1 at B-site and (j), (k), (l) C2 at B-site respectively for an isodensity value of 0.005 e/Bohr^3. Taken from Baby et al. Ref. [64].

i.e. perpendicular to the plane of the molecule is shown in figure 3.9 as a solid black line. Owing to the lack of absolute energy reference from the calculation, this spectrum is arbitrarily offset so as to align it with the most prominent features in the spectra measured for absorbed molecules (to be presented subsequently). The contributions from individual excitations (initial and final state) is also marked in figure 3.9 by showing the projected amplitude of the final state on the p_z atomic states of the absorbing atoms, which produces a good qualitative description of the NEXAFS spectrum [58, 119]. One can see two visibly separated broad features with multiple peaks. The first broad feature (spanning the energy range between 282.5 eV and 284 eV) is completely due to the core-electron excitations to the LUMO of pentacene. The first peak of the second broad feature lying between 284.5 eV and 285.5 eV is mainly constituted by the LUMO+1 excitations and partly also by the LUMO+2. The larger energy contributions to the second broad feature are from higher lying LUMO+i orbitals. In considering these contributions one has to recall that the presence of a half core hole affects the molecular orbitals resulting into their intermixing and hybridization, as compared to the ground state [64]. To show this, in Table 3.3 we report the overlap between the molecular orbitals of the excited V-shaped molecule in gas phase with those of the ground state undistorted one, referred to as former LUMOs is reported, selecting as a representative example that of C1. The presence of half core hole has not affected the LUMO but has significantly altered the higher lying LUMOs as also found for perylene derivatives [119]. It is noteworthy that a free pentacene molecule has a nodal plane for (former) LUMO+1 and LUMO+2 along the central carbon atoms C1 and C1' (see figure 3.6) so no contribution to NEXAFS would be expected by transitions to these molecular orbitals from the 1s orbital of C1 at variance with the

Figure 3.9: Simulated NEXAFS of the gas phase V-shaped pentacene from the B-site along the field z-direction, perpendicular to the molecular plane. For excitations from each C atom, the vertical bars numbered correspondingly show the projection of the various molecular orbitals, computed with half core hole in that atom, on the $2p_z$ state of the same carbon atom, and are referred to the axis on the right (in %). Taken from Baby et al. Ref. [64].

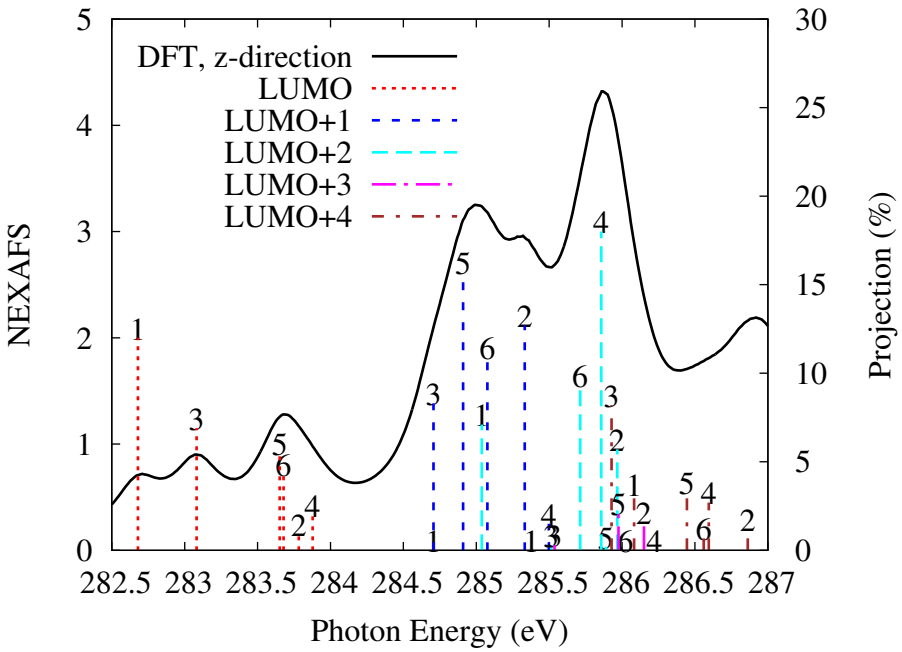

Table 3.3: Overlap of the molecular orbitals of pentacene with a half core hole (*hch*) at C1 in the V-shaped geometry, with those of the free molecule in the ground state, g. Values less than 0.5 % are not reported here. Taken from Baby et al. Ref. [64].

$C1^{hch}$	Orbitals of free molecule in the ground state (g)			
	LUMO	LUMO+1	LUMO+2	LUMO+3
LUMO	77.2 %	-	-	5.6 %
LUMO+1	-	89.2 %	-	-
LUMO+2	11.0 %	-	-	51.4 %
LUMO+3	-	-	86.5 %	-
LUMO+4	-	-	-	9.5 %
LUMO+5	-	-	-	16.8 %

result in figure 3.9 of a non negligible contribution from the transition from the C1 1s to the LUMO+2. This is because the LUMO+2 and LUMO+3 orbitals get interchanged due to the V-shaped bending of pentacene already in the ground state, where the structural deformation of pentacene causes the former LUMO+2 to shift to a higher energy than that of LUMO+3, which is retained also with the core hole [64]. Indeed, now the LUMO+2 displays contributions by the former LUMO and LUMO+3 (see table 3.3). Furthermore, we can see that LUMO+3 in figure 3.9 has no weight on C1, as it originates mostly from the LUMO+2 of the undistorted free molecule which has moved to higher energy. In the case of adsorbed pentacene, the molecular orbitals broaden due to hybridization with the substrate states extending into overlapping energy ranges, hampering a similar analysis in terms of final states.

Figure 3.10 shows the simulated NEXAFS spectra for pentacene adsorbed at the B-site in (a) p-polarization with the electric field perpendicular and (b) s-polarization with the electric field parallel to the surface. The long molecular axis is directed along the x-direction and the short molecular axis along the y-one. There, the spectrum decomposed in terms of initial state effects is shown and compared to the experimental result (dashed line) [64], for different orientations of the surface normal with respect to the linearly polarized photon beam. Looking at the upper panel (a) of figure 3.10, we can see a nice agreement between the experimental and simulated p-polarization (solid line) results. The simulated spectrum is arbitrarily aligned to the most prominent double peaked experimental feature centered at 285.5 eV which can be attributed to the π^* resonances. The first peak of the π^* resonance consists of contributions from all the atoms except C1 and C4. The second peak has contributions from all the atoms but with a major weight from C4. It can be observed that the π^* resonances in figure 3.10 have narrowed down compared to those of the V-shaped gas phase pentacene in figure 3.9. It was mentioned before that the V-shaped structural deformation alone reduces the HOMO-LUMO gap of the free molecule by 0.5 eV which facilitates the filling of LUMO by getting electronic charge from aluminum and is hence absent in the NEXAFS spectrum [64]. Absence of significant contribution from C1 in the first peak of the π^* resonances in figure 3.10 further confirms that such a peak corresponds to transitions to the LUMO+1 rather than the LUMO of the molecule [64].

Most importantly, the observed narrowing of the measured π^* resonances with respect to those of the free molecule ones, is well reproduced by the simulations at B configuration. To understand this narrowing, it is useful to look at the molecular density of states at the B-site. The case of excitations

Figure 3.10: (a) Analysis of the initial state effects in the simulated NEXAFS spectrum and its comparison with the experimental one measured in p-polarization (electric field along z, i.e., perpendicular to the surface). (b) Same as (a), in s-polarization. Simulations are shown for electric field in the x and y-directions (i.e., along the long and short molecular axes). Taken from Baby et al. Ref. [64].

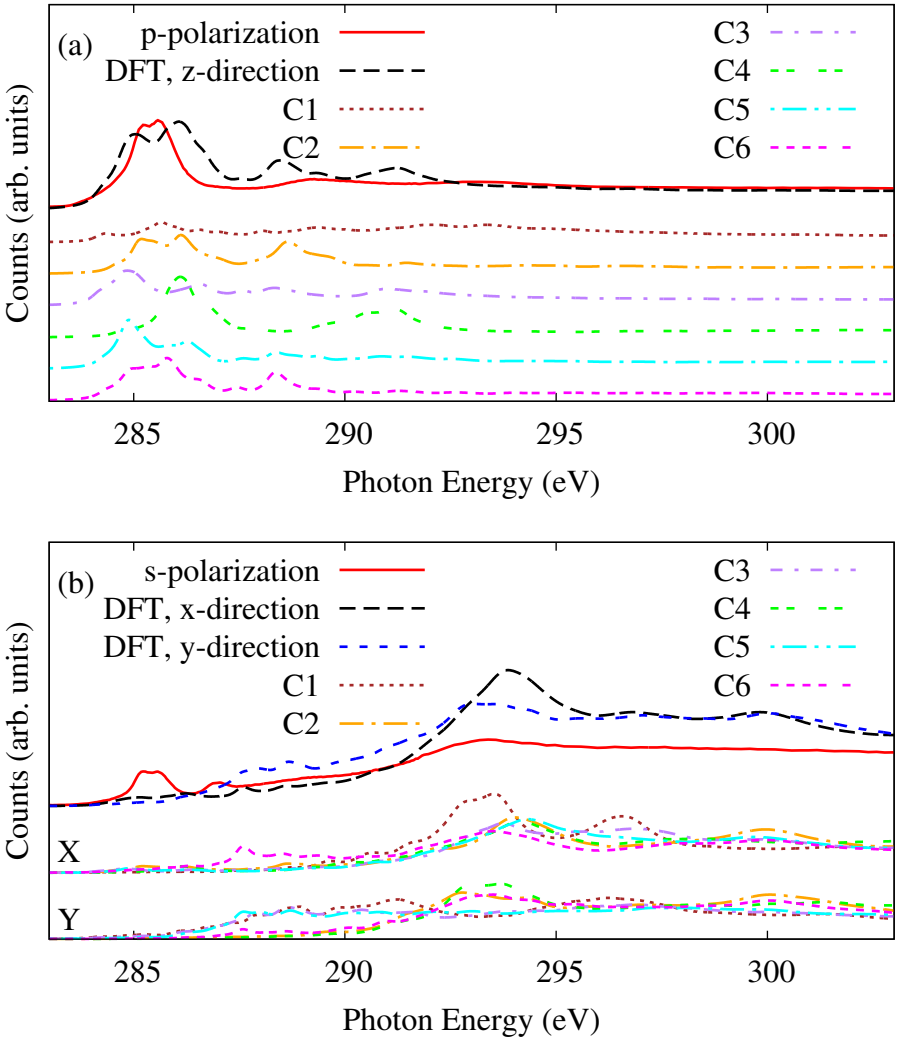

from the 1s orbital of one of the central C atoms is taken as a representative example and the DOS projected onto the molecular orbitals is displayed in figure 3.11. At variance with the ground state result shown previously in figure 3.4(b), here a half core hole is included in the calculation as in the simulated spectra of figure 3.10. It can be observed that the LUMO narrows and lowers further by the core hole attraction and, being centered at about 1.6 eV below the Fermi level, it cannot participate in the X-ray absorption process [63]. The spectrum is hence contributed solely by higher molecular orbitals. These effects are analogous to those described for the case of molecules adsorbed at the surface of a semiconductor [121], yet mitigated here by the screening of the metal electrons. Similar results are obtained when exciting the core level of the other C atoms and hence we can conclude that the filling of the LUMO is the origin of the narrower π^* resonance in the spectrum.

Now let us look at the σ^* resonances of figure 3.10(b) where the simulated NEXAFS computed for the molecule at B-site along the x and y directions (long and short molecular axes respectively) are compared to the experimental NEXAFS in s-polarization. The experimental s-polarization has been averaged over the [110] and [001] surface azimuths, which provide very similar results as differently oriented domains are sampled. The experimental spectrum still displays some π^* resonance leftover centered at around 285.5 eV. This residual intensity of the π^* resonance measured in the s polarization ($\sim$ 15 % of the intensity collected in p polarization), indicates a tilting of the aromatic plane by $28^\circ \pm 5^\circ$ with respect to the surface. This effect is not completely reproduced in the simulated spectrum even if we observe some non-zero contributions which are due to the V-shaped molecules forming an angle of about $\frac{\pi-\alpha}{2} = 13^\circ$ with the surface plane. In this respect, it

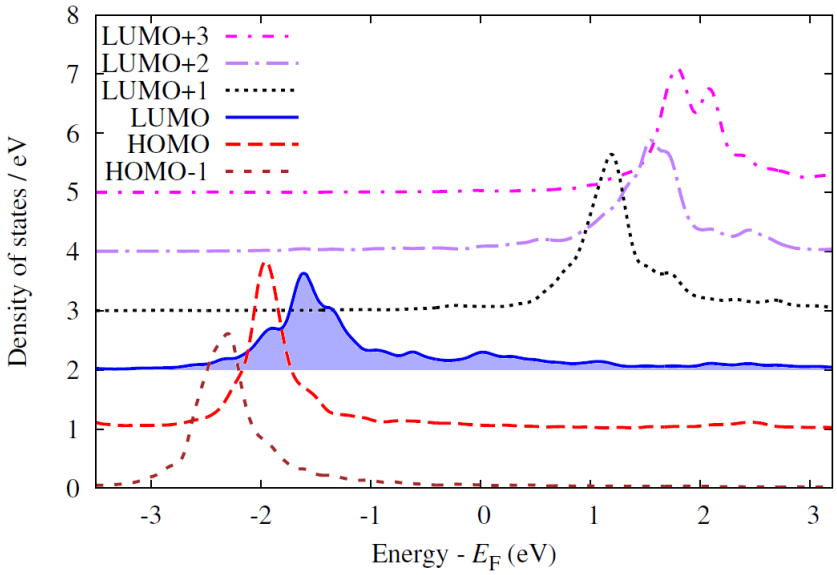

Figure 3.11: DOS of pentacene/Al(001) in the *B* adsorption configuration with half a core hole on the central carbon atom, projected onto the molecular orbitals. Taken from Baby et al. Ref. [63].

is remarked that structural optimizations were also attempted for molecules initially tilted by 30° with respect to the z-direction; however, they returned to the 0° tilt angle geometry retaining the V-shape in the lowest energy configuration. So the presence of the π^* resonances in the experiment even for s-polarization could be interpreted as a result of a fraction of molecules being adsorbed at step edges or defects due to the low degree of ordering (large atomic roughness) of the Al surface as further confirmed by the RHEED images [63].

Looking at the main σ^* peak centered at around 294 eV, a small energy splitting between transitions with the electric field along the long and short molecular axes is observed. This azimuthal dichroism [58] is much reduced, as compared to that of the free molecule. In the latter case, such azimuthal dichroism amounts to about 2 eV and was attributed equally to the intrinsic asymmetry of the molecule and to the shorter C-C bond lengths along the long molecular axis than that along the short one [58]. For adsorbed V-shaped molecules, the bond lengths along the two directions are more similar, as reported in table 3.2. This produces a substantial reduction of azimuthal dichroism to approx. 1 eV. Reporting the initial state contributions in this energy range, the x-direction spectrum has largest contributions by the core excitations from C1 whereas the y-direction one mainly by those from the carbon atoms C2, C4 and C6 [64]"[10].

3.6 STM

Experimental STM images with sub-molecular resolution are shown in figure 3.12, with a negative voltage (−0.8 V) corresponding to the tunneling

[10]Taken from Baby et al. Ref. [64]

through the occupied molecular states. "Few molecules close to a region exposing the reconstructed substrate are imaged in figure 3.12(a). There, the molecule on the left is oriented along the [110] direction (alike the majority phase), and the other two have an intermediate azimuthal orientation as they are attached at a step edge. Molecules oriented along the [100] direction (minority phase) are shown in figure 3.12(b). All these molecules display a clear saddle-shape topography like those oriented along the [110] direction, which forms the molecular stripes of the majority phase. Molecules oriented along [110] and [100] directions can be compared to the simulated STM images for the B and H' adsorption configurations, respectively. The STM images were simulated in constant current mode by integrating the local density of states (LDOS) from the bias voltage until the Fermi energy using the Tersoff Hamann approach [68]. They are evaluated from the isosurface of the electronic density of states (isovalue 6.7 x 10^{-6} states/Å^3) corresponding to an average height of $\sim$ 350 pm above the molecule and are reported as insets in figure 3.12 (panels a and b) [63].

The V-shaped bending results in an apparent height depression of 30 pm at the center of the molecule in the constant DOS mapping. This value, much less than the height difference Δz = 135 pm between C atoms, is indeed in excellent agreement with measured data. For comparison, the experimental line profiles along the long molecular axes are shown in figure 3.12(c) together with the calculated ones, highlighting a height depression of about $20 - 30$ pm at the center of the molecule for the three measured molecular orientations. Molecules appearing with higher peripheral rings in the STM were also reported for pentacene/Au(111) but rather attributed to a simple electronic effect [85]. Remarkably, not only the molecules oriented along the [110] and [100] directions but also those at the step edge display a very

similar V-shape inflection, suggesting that also in this peculiar orientation pentacene sits atop two Al atoms suitably displaced for direct anchoring of the central carbon atoms. This observation illustrates both the strong pentacene/substrate interaction and the universality of the V-shaped adsorption configuration [63].

Concerning the morphology of the pentacene overlayer, the side-by-side molecular coupling into elongated stripes is a quite common morphology for pentacene in the submonolayer range, and it has been observed on a wide variety of crystalline surfaces from fcc metals [85, 122, 123, 124] to TiO_2 [125]. A few structures at denser coverage were computationally analysed to investigate the role of intermolecular interactions. In this case, a thicker surface k-point sampling was adopted, corresponding to meshes equivalent to at least 16×16 points in the (1×1) surface unit cell for comparison between different unit cells [63]. Our results for $(n \times m)$ rectangular surface unit cells with molecules in the B configuration show an adsorption energy which is independent of n and m down to the (6×3) periodicity, where the molecules are 3.58 Å apart. A weak intermolecular interaction could not allow discriminating among different overlayer configurations directly from the calculations. We speculate that the V-shape bending hampers the π coupling between adjacent molecules, thus the residual intermolecular vdW attraction is definitely lower than that exerted by the Al substrate [63]"[11].

[11]Taken from Baby et al. Ref. [63]

Figure 3.12: (a) STM image showing submolecular resolution of pentacene close to a region with substrate exposed. Bias $V = -0.8$ V. The simulated STM image at the same bias for a B molecule is shown as inset. (b) STM image of molecules accomodated within the substrate reconstruction, but oriented along the [100] direction, and compared to simulated result for the H' configuration. (c) Experimental line profile for differently oriented molecules, taken along lines depicted in panels (a) and (b), compared to the calculated one for molecules in B and H' configurations. Taken from Baby et al. Ref. [63].

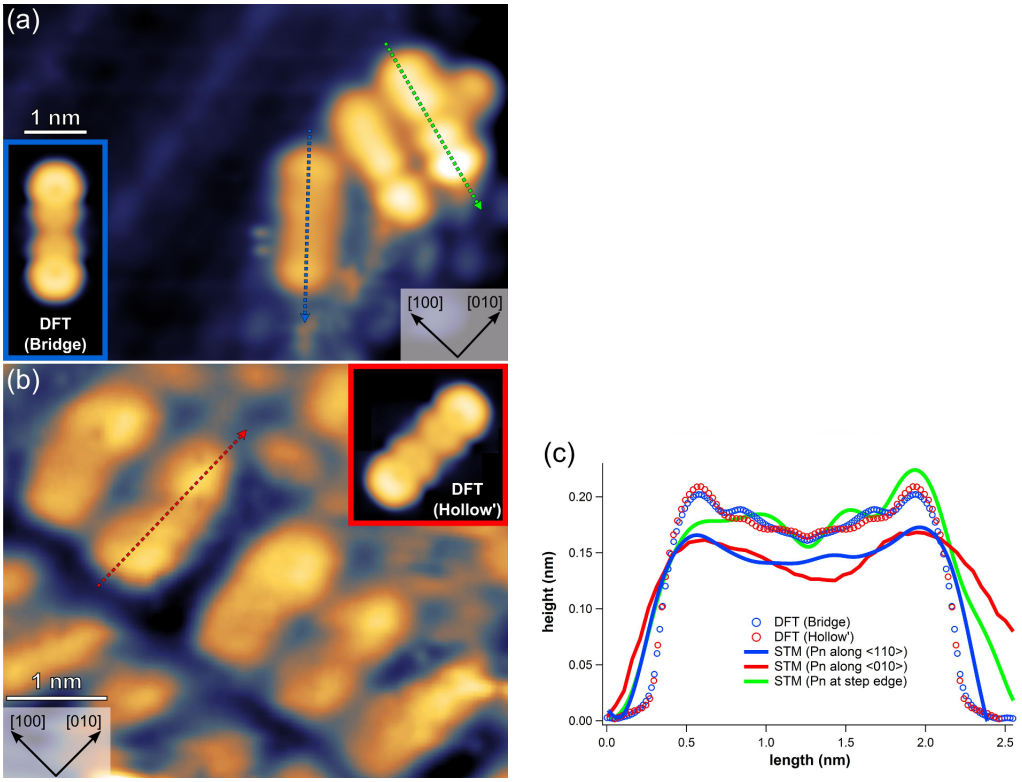

Chapter 4

Potassium doping of PTCDA/Ag(111)

4.1 Introduction

Due to the high electron affinity (4.5 eV) and ionization potential (8.15 eV) of the dye molecule 3,4,9,10-perylenetetracarboxylic dianhydride (PTCDA), it can be easily n-doped [26, 127]. The effects of doping the PTCDA layers with alkali metal atoms has been thoroughly investigated with regard to the electronic and optical properties [128, 26, 129, 130, 131, 132, 133, 134]. Quoting our paper Ref.[73] "Molar doping ratios x (i.e., number of dopants per host molecule) on the order of several percent already lead to a substantial increase of σ. Higher ratios x have been shown to boost σ by as much as 6 orders of magnitude, as demonstrated for PTCDA". Alkali metal atoms such as sodium, potassium and cesium have been used so far in order to dope organic molecules [73, 130, 131, 132, 133, 134]. But the dopant sites have not been accurately determined by employing the direct experimental imaging techniques till date. In this work we use K atoms to dope the PTCDA

submonolayer adsorbed on Ag(111). We chose PTCDA/Ag(111) as it is a very well-known, well-studied and well-understood system [142, 148].

Experimental methods such as low-energy electron diffraction (LEED) and STM can be used to obtain the variations in the lattice parameters upon intercalation with dopant atoms. But due to the usually blurred electronic contrast of STM images for adsorbates on metal surfaces, the precise and simultaneous imaging of the dopant atoms along with the host molecules is rather challenging [35, 36]. "As a promising strategy to tackle this drawback, STHM introduced by Temirov et al. may be used [70]. This technique is adapted here to image simultaneously PTCDA molecules and potassium atoms for K_xPTCDA complexes of varying stoichiometries x of K in PTCDA monolayer domains on Ag(111) surface. This is realized by tuning the tunneling conditions such that the recorded signal is close enough to the ideal STHM case for highly resolved submolecular contrast of PTCDA but still contains a sufficient contribution of the local electron density of states to identify the K atoms as well. This then enables a detailed observation of the unit cell composition"[1] and for the first time the dopant atoms and host molecules have been imaged in the same scan using this method.

In this work, the experiments were done by Prof. Torsten Fritz and his group at the Institute of Solid State Physics, Friedrich Schiller University Jena, Germany and they obtained two distinct highly ordered, large and stable phases by controlled doping of PTCDA/Ag(111) by K. From the distortion-corrected quantitative LEED measurements they found that the epitaxial relations for both of these intercalation concentrations are classified as point-on-line (POL) with respect to the silver substrate [135, 73]. Thorough theoretical investigation of all the cases (before and after doping) by

[1] taken from Zwick, Baby et al. Ref.[73]

means of DFT calculations was my main objective of work during the secondment under the supervision of Prof. Egbert Zojer at the Institute of Solid State Physics, Graz University of Technology, Austria. DFT results became inevitable especially for the second phase where the ST[H]M images exhibit an ambiguous feature. "With this interplay between the complementary information acquired from LEED, ST[H]M, and DFT, comprehensive insight into the formed structures is gained, which is indispensable for future evaluations of the electronic properties of alkali-metal intercalated interfaces"[2].

4.2 Experimental Findings

The experimentalists performed differential reflectance spectroscopy (DRS) for making the initial interpretations of the chemical processes occurring during K doping which is a version of optical absorption spectroscopy. One main advantage is that DRS can be applied also in the case of opaque substrates. It is a real-time in situ reflectance measurement process carried out during film deposition under UHV conditions, and the measured quantity is:

$$DRS(E,d) = \frac{R(E,d) - R(E,d=0)}{R(E,d=0)} \tag{4.1}$$

where $DRS(E,d)$ is the change in reflectance between the covered $R(E,d)$ and bare $R(E,d=0)$ substrate surface, E is the photon energy and d is the film thickness [136, 137]. The DRS spectrum is basically due to the electronic transitions between the frontier orbitals of the molecule. In the case of molecular adsorbates hence one can probe their electronic properties. So when optical transitions between the metal-organic hybrid orbitals occur, this effect is also reflected in the DRS spectrum when compared with the

[2]taken from Zwick, Baby et al. Ref.[73]

molecular spectrum in solution. In this way this method can also help to discriminate between physisorption and chemisorption, taking the previous spectrum as reference. The magnitude of this spectrum is sensitive to the molecular adsorbate layer thickness and increases with the increasing number of layers as more absorption sites are available. Since unpolarized light can be used for DRS measurements, it can be also applied to polycrystalline or amorphous materials but then since single-crystalline materials form well ordered epitaxial layers the analysis is eased [138]. When polarized light is used, for not normal incidence DRS gives different signals for s and p-polarizations and less or no difference for normal incidence.

The evolution of the in-situ DRS spectra of 0.7 ML of PTCDA on K doping are shown in panels (a) and (c) of Figure 4.1. Spectra in panels (b) and (d) of Figure 4.1 are given as references for comparison. The black curve in Figure 4.1(a) corresponds to 0.7 ML of undoped PTCDA on Ag(111) which exhibits a very broad and featureless absorption behavior due to the strong electronic interaction at the metal-organic interface as in chemisorption [136]. Whereas the situation changes dramatically upon doping (red curve in panel (a)). Up to 5 mins of potassium deposition (1st doping stage) the spectrum becomes less broad which indicates a much weaker and predominantly physisorptive electronic interaction with the substrate. The DRS spectrum of 1 ML of PTCDA on a weakly interacting Au(111) surface [137] is shown with the red curve in Figure 4.1(b) for comparison and a good similarity can be observed between the two spectra (red curve in panels (a) and (b)). Therefore, they excluded the formation of K doped PTCDA monoanions on the Ag(111) surface which would lead to a different spectral fingerprint as shown by the dark brown curve in Figure 4.1(b) (T. Dienel, Dissertation, TU Dresden (2005)). From 5 mins on up to 8 mins of K deposition sharp spectral

features arise (blue curve in panel (c)). These features can be unambiguously assigned to the electronically decoupled K doped PTCDA dianions as seen in Figure 4.1(d) (blue curve, cf. T. Dienel, Dissertation, TU Dresden (2005)).

After acquiring an initial input regarding the electronic properties by means of DRS, the structural information for the different doping stages was obtained from low temperature (LT) STM, STHM [70] and LEED techniques. The adsorption sites of K were precisely determined from the STHM images with the help of DFT simulations. Additionally, for all the cases highly accurate epitaxy matrices were determined from the LEED images [73]. We recall here that the term epitaxy is used when the adsorbate overlayer grows following the orientation of the substrate on which it is grown. And an epitaxy matrix C is a matrix that gives the geometrical relationship between the adsorbate unit cell vectors, $\mathbf{a_{1,2}}$ and the substrate unit cell vectors, $\mathbf{s_{1,2}}$ for an epitaxial overlayer. It is defined via the relationship:

$$\begin{bmatrix} \mathbf{a_1} \\ \mathbf{a_2} \end{bmatrix} = C \cdot \begin{bmatrix} \mathbf{s_1} \\ \mathbf{s_2} \end{bmatrix} = \begin{pmatrix} C_{11} & C_{12} \\ C_{21} & C_{22} \end{pmatrix} \cdot \begin{bmatrix} \mathbf{s_1} \\ \mathbf{s_2} \end{bmatrix} \tag{4.2}$$

For full-commensurism all the elements of the epitaxy matrix C are integers since all the adsorbate lattice points are situated on the substrate lattice points. In the case of point-on-line epitaxy, all adsorbate lattice points are situated on primitive substrate lattice lines and not necessarily substrate lattice points and hence only one of the columns of the epitaxy matrix will consist of integers [143]. A new type of epitaxy is found in the case of organic-organic heteroepitaxy called the line-on-line epitaxy which cannot be identified by looking at the epitaxy matrix as the adsorbate lattice points lie on substrate lattice lines, not necessarily on the primitive ones. The epitaxy matrix in this case contains non-integer or even irrational elements. If none of the adsorbate lattice points neither lie on the substrate lattice points nor coin-

Figure 4.1: In-situ differential reflectance spectra (DRS) of 0.7 ML PTCDA being doped with potassium showing the different doping stages (Courtesy of Prof. Torsten Fritz and group).

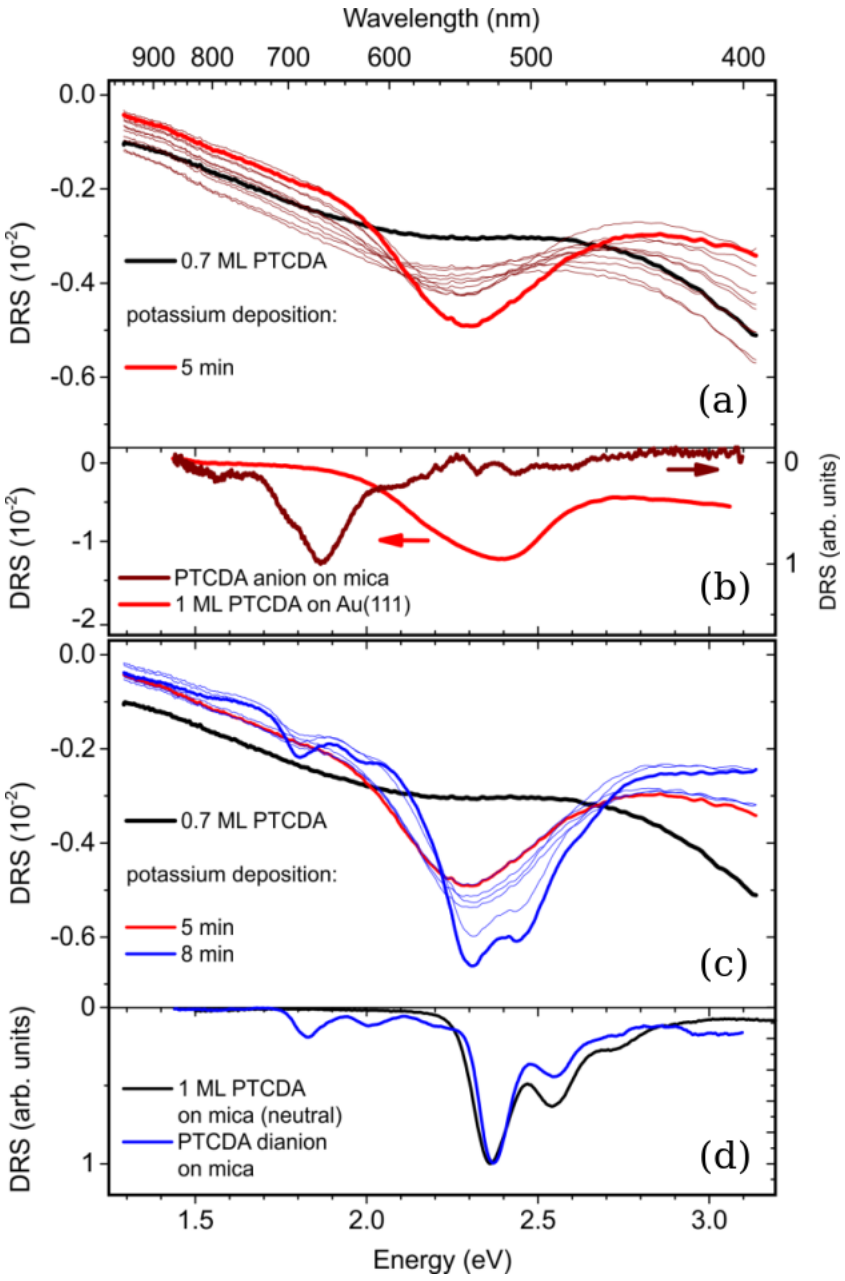

cides with the substrate (primitive or non-primitive) lattice lines then the adsorbate is said to be incommensurate with the substrate.

Self-assembled structures of distinct K_xPTCDA phases on Ag(111) for x = 0, 2, and 4 are shown in Figure 4.2. Figures 4.2 (a), (b), and (c) show the STM image, structural model, and LEED image of pristine PTCDA/Ag(111). It is well known that the undoped PTCDA forms commensurate monolayers in the herringbone motif on Ag(111) [139, 140, 141, 142]. Since in the experiments they were always working with sub-monolayer coverages, part of the silver surface was uncovered to allow possible structural rearrangements without forcing the molecules to adopt adsorption sites in the second layer. By depositing potassium onto these sub-monolayer domains of PTCDA/Ag(111), the herringbone structure is converted into a new highly ordered self-organized phase even without annealing. This phase is called K_2PTCDA according to the stoichiometry i.e. two K atoms per PTCDA molecule as shown in the structural model obtained from the STHM image (Figures 4.2(d) and (e)).

All the molecular domains transformed uniformly and spontaneously into the K_2PTCDA phase even without annealing the sample [73]. These K_2PTCDA domains exhibited a rather low defect density. "By means of LEED (Figures 4.2(e) and (f)) the experimentalists found a unit cell with significantly shorter lattice vectors ($|\mathbf{a_1}|$ and $|\mathbf{a_2}|$ decrease by 29.9% and 15.4%, respectively) and an increased unit cell angle Γ as compared to the initial commensurate herringbone structure (Figure 4.2(b)). Further, the epitaxial relation is a point-on-line (POL) coincidence, as can be inferred from the differences between the epitaxy matrix elements in each row being integer numbers. This is equivalent to a column of integer elements in the epitaxy matrix, provided

Figure 4.2: The K_xPTCDA phases on Ag(111) for $x = 0$, 2, and 4. (a) shows the STM image, (d) and (g) show the STHM images; (b), (e), and (h) shows the structural models; (c), (f), and (i) LEED images. In each LEED image (c), (f), and (i), the simulated reciprocal unit cell of the associated K_xPTCDA structure ($x = 0$ purple, $x = 2$ orange, and $x = 4$ blue) and the silver surface orientation along (01) and (10) (yellow) are superimposed. Displayed quantities: V_T bias voltage; I_{SP} tunneling current; E beam energy; $\mathbf{a_1}$, $\mathbf{a_2}$ adsorbate lattice vectors; Γ is the angle between $\mathbf{a_1}$ and $\mathbf{a_2}$; $\mathbf{s_1}$, $\mathbf{s_2}$ are the substrate lattice vectors with unit cell angle between them of 120°; ϕ is the angle between $\mathbf{s_1}$ and $\mathbf{a_1}$ domain angle; ξ(A/B) is the orientation of molecules A and B in the unit cell. Taken from Zwick, Baby et al. Ref. [73].

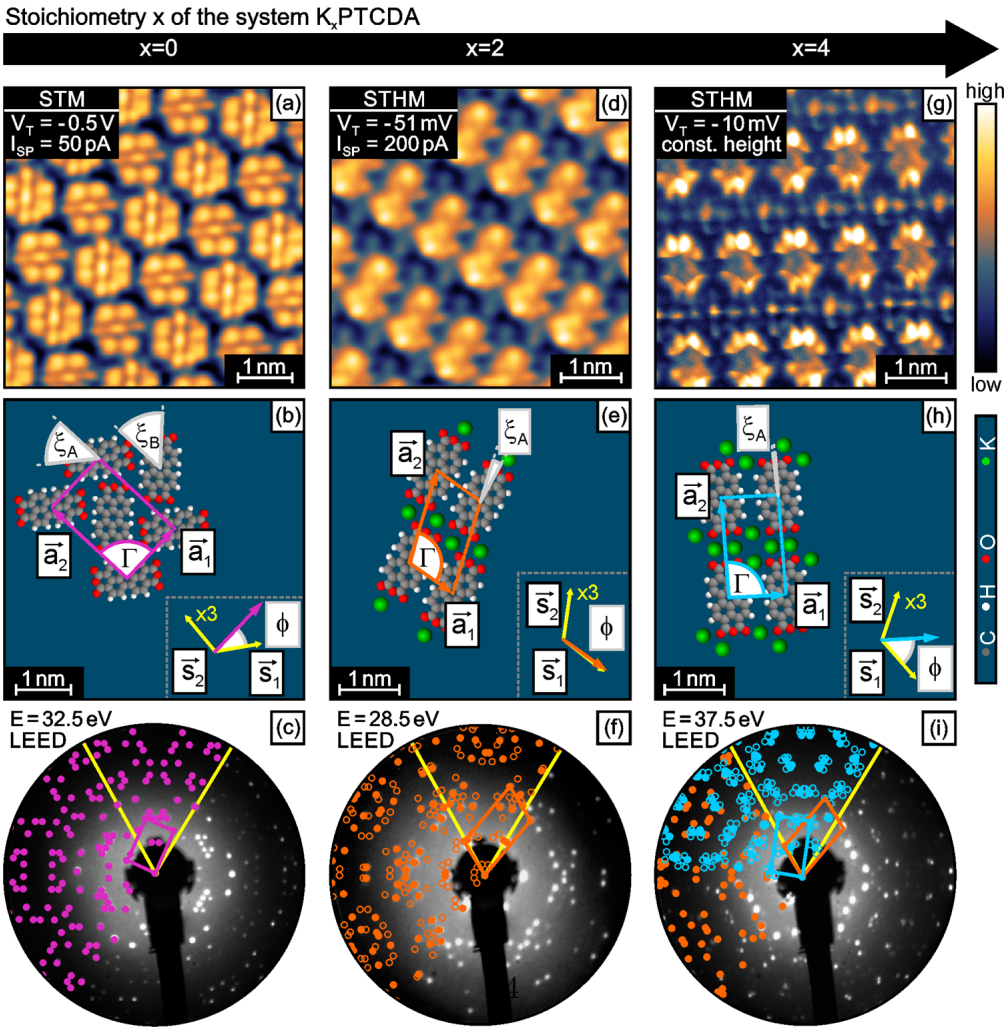

that $\angle(\mathbf{s_1}, \mathbf{s_2}) = 120°$ (as chosen here for the Ag(111) surface) [143]"[3].

Various samples with several different STHM conditions were studied by the experimentalists and it can be confirmed that artifacts such as the features caused by double tips are not present. A reduction in the total unit cell area is observed as now there is only one molecule per K_2PTCDA surface unit cell compared to two molecules for the herringbone arrangement of the pristine PTCDA layer the total unit cell area has reduced. The structural data of the same is given in Table 4.1. The STHM image further shows that potassium is incorporated in-plane into the molecular film close to the short edge of PTCDA. Under closer inspection, the potassium atoms are located near the oxygen atoms and exhibit rather similar bonding distances to PTCDA as compared to the calculated structure of freestanding K_2PTCDA complexes [26]. It has been shown that such a structure is a consequence of an ionic bonding between the alkali metal and PTCDA resulting in PTCDA dianion formation [130, 131]. By inspecting domains of the K_2PTCDA phase with STHM (Figure 4.2(d)), the formed complex shows a characteristic stripe-like assembly of alternating rows of PTCDA and K, both oriented along the short lattice vector $\mathbf{a_1}$, with the molecules oriented nearly perpendicular to the stripe axis. The relative shift of molecules in adjacent rows of PTCDA offers the densest packing and a coordination maximum of the intercalated potassium towards the carboxylic groups. One can view the situation as one-dimensional PTCDA stripes between which rows of K atoms are intercalated (i.e., a reduced dimensionality analogon to conventional intercalation of atoms between 2D extended layers) [144]. It is noteworthy that the Ag(111) surface remains structurally unaltered upon K deposition. This is fundamentally different from the situation encountered for the Ag(110) surface, which

[3]taken from Zwick, Baby et al. Ref. [73]

was previously found to reconstruct significantly when K is evaporated onto a pre-deposited PTCDA monolayer with subsequent annealing [34]. There the smaller packing density of the Ag(110) surface (whose atoms retain a lower coordination number) allows for an incorporation of K into the topmost silver layer, resulting in a long-range "potassium-induced missing row reconstruction" [34]. Since our experiments were performed without post-growth annealing and revealed no surface reconstruction it is unlikely that K diffused into the topmost densely packed Ag(111) atomic layer. Instead, it was exclusively found intercalated in between PTCDA molecules, i.e., neither underneath nor on top of the molecular layer.

By further controlled evaporation of K, at the end of 8 mins the former K_2PTCDA phase is converted into a second highly ordered intercalation stage as shown in Figure 4.2(g). It was quite challenging to determine the stoichiometry for this phase from the STM and STHM images alone as only a single blob-like feature was visible in the former and five separate features were visible in the latter corresponding to the presence of five K atoms which was more than the estimated K content as per the deposition rate (Figures 4.8(2)(a),(c)). And so initially, the experimentalists assigned this phase wrongly as K_3PTCDA with x=3 as it was in better agreement with the K deposition rate. But in order to avoid ambiguity in the terminology used and also in anticipation of the results, this phase will be referred to K_4PTCDA from here onwards. The transition to this phase occurs directly, as evidenced by the LEED investigations, which reveal no intermediate structure (Figure 4.2(i)). By means of ST[H]M large domains of the K_4PTCDA complexes are observed. The defect density is low, but their structural perfection is slightly inferior to the K_2PTCDA phase, i.e., the average domain size is smaller and the number of defects appear somewhat increased. To

optimize simultaneously the contrast and to exclude possible experimental artifacts, a variety of experimental conditions were also used here. The LEED analysis reveals a significant change of the lattice parameters compared to the former K_2PTCDA phase. Both unit cell vectors increase in length ($|\mathbf{a_1}|$ and $|\mathbf{a_2}|$ increase by 7.3% and 4.6%, respectively), while their enclosed angle Γ decreases (Table 4.1). The epitaxy matrix contains one column of integer numbers as can be seen in Table 4.1, thus a point-on-line coincidence can be stated also in this case [143]. Note that in LEED experiments with average molar ratios x between 2 and 4, coexisting K_2PTCDA and K_4PTCDA phases were often found on the same sample, indicating that on macroscopic scales the layer is not necessarily uniform. Notably, the relative intensity of the LEED spots associated with K_4PTCDA could be successfully increased at the expense of the K_2PTCDA phase content by additional K deposition.

Compared to the former K_2PTCDA phase, the changed lattice parameters imply an increase of the unit cell surface area per molecule of 18.3%, offering the necessary space for the additional K atoms. The corresponding structure exhibits a stripe-like assembly of alternating K and PTCDA rows oriented alongside $\mathbf{a_1}$, similar to the K_2PTCDA phase but with some notable differences: The formerly mentioned relative shift of adjacent rows of PTCDA along $\mathbf{a_1}$ (by about half of its length) has disappeared now. The molecules are arranged in an essentially rectangular pattern and are almost parallel to the long lattice vector $\mathbf{a_2}$.

4.3 Computational Approach and Results

The DFT calculations were performed by applying the repeated slab approach using the Vienna ab initio Simulation Package (VASP) [145] in con-

Table 4.1: Structural data of the distinct K_xPTCDA phases on Ag(111). Taken from Zwick, Baby et al. Ref. [73].

x	$\lvert\mathbf{a_1}\rvert$ (Å)	$\lvert\mathbf{a_2}\rvert$ (Å)	Γ (°)	A_{PTCDA} (Å^2)	Epitaxy Matrix, C
0	12.59	18.95	90.99	119.3	$\begin{pmatrix} 5.00 & 3.00 \\ -1.00 & 6.00 \end{pmatrix}$
2	8.92	16.05	108.60	135.7	$\begin{pmatrix} 3.16 & 0.16 \\ 0.98 & 5.98 \end{pmatrix}$
4	9.57	16.77	91.66	160.4	$\begin{pmatrix} 3.55 & 3.00 \\ -2.65 & 4.00 \end{pmatrix}$

junction with GADGET [146] (see Appendix B for more information). The Purdew Burke Ernzerhof (PBE) functional [46] was applied together with the vdW^{surf} method [48, 50] to account for the long range vdW interactions. Off-gamma Monkhorst-Pack [100] k-points grids of 5x3x1 was used for the first doping stage and 3x3x1 for the second doping stage with a Methfessel-Paxton [101] smearing of 0.2 eV. Projector augmented wave (PAW) pseudopotentials [147] were used with a cutoff energy of 400 eV for the plane-wave basis set. The silver substrate was constructed with five layers of atoms with the bottom three layers fixed during all the optimization runs.

4.3.1 Modification of the Ag substrate

The experimentally determined unit cell and stoichiometry were used for the calculations. Given that K_2PTCDA is not commensurate but point-on-line with respect to Ag(111), the silver unit cell had to be slightly modified in order to achieve a geometry consistent with periodic boundary conditions (i.e., a fully commensurate arrangement), necessary for the calculations. "In

principle, a quasi-commensurate structure with an all integer epitaxy matrix could also have been achieved by slightly modifying the unit cell of the adsorbate, but we intentionally kept the experimentally determined dimensions in order not to modify the distances between the K atoms and the PTCDA molecules bearing in mind the crucial role played by the interactions between the K atoms and the carboxylic and anhydride oxygen atoms. The elements of the epitaxy matrices were either rounded off to the nearest integer (in the K_2PTCDA case) or first doubled in order to obtain close-to-integer values and then rounded off (in the K_4PTCDA case)"[4]. In the latter case, this would have resulted in an epitaxy matrix $\begin{pmatrix} 7 & 6 \\ -5 & 8 \end{pmatrix}$ with 4 molecules in the unit cell (indicated by blue lines in Figure 4.3), thereby making the computation tedious. This could be avoided by redefining a supercell being commensurate with the substrate containing only 2 molecules as shown by green lines in Figure 4.3 with an epitaxy matrix $\begin{pmatrix} 7 & 6 \\ 1 & 7 \end{pmatrix}$.

The changes in the Ag(111) lattice constants due to this rounding off of the epitaxy matrix elements to the nearest integers were very small around 0.6% along one and 2.8% along the other substrate unit cell vector directions for K_2PTCDA and similarly for K_2PTCDA. The modified unit cell parameters for the two phases are summarized in Table 4.2. Firstly we had to check to what extent these modifications of the Ag substrate effected its electronic properties. For this purpose we computed the work function and interlayer spacing of the modified silver slab for both cases. We computed the work functions, surface interlayer spacings and extent of surface relaxations of the distorted Ag substrates and the differences were negligible compared to those of the pristine Ag substrate calculated using the optimized PBE lattice

[4]taken from Zwick, Baby et al. Ref.[73]

Figure 4.3: Possible supercells (green and blue lines) that can be used as commensurate adsorbate structures to approximately describe the K_4PTCDA layer on Ag(111). Red dots and lines mark the Ag(111) substrate lattice and unit cell (Courtesy of Marco Gruenewald).

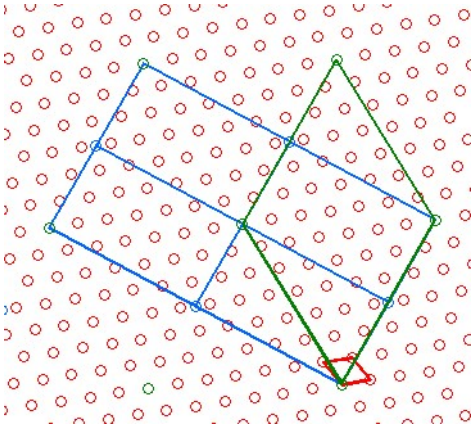

constants and also from the experiments as shown in Table 4.2.

4.3.2 Structural Optimization

As the changes in the electronic properties of the modified Ag substrate were negligible, we passed onto optimizing the adsorption structure of the PTCDA and 2K monolayer on the modified Ag substrate of the K_2PTCDA phase given in Table 4.2. So as a first step we optimized the structures for the two K atoms and PTCDA separately on the modified Ag substrate by arranging at positions similar as viewed in the experimental STHM. The motivation behind the starting geometry for 2K in the K_2PTCDA unit cell was that during the relaxation calculations with a single K atom on pristine Ag substrate it preferred the fcc hollow site with an adsorption height of 2.372 Å. In the optimized geometry however (Figures 4.5(a) and (b)), one K atom sits on the fcc hollow site and the other one (which was initially on fcc

Table 4.2: The rounded epitaxy matrix used in calculations C', resulting commensurate Ag substrate unit cell vectors $|\mathbf{s_1}|, |\mathbf{s_2}|$ and the angle between them γ, substrate work function, surface interlayer spacing Δz^{surf} and the comparison to the bulk interlayer spacing Δz^{bulk}. All values are given for bare Ag(111) substrates for the pristine surface with optimized lattice constants (PBE) and for the modified surfaces later used to accomodate commensurate K_2PTCDA and K_4PTCDA structures. Experimental values are given for comparison. Taken from Zwick, Baby et al. Ref. [73].

	Epitaxy Matrix, C'	$\lvert\mathbf{s_1}\rvert$, $\lvert\mathbf{s_2}\rvert$ (Å)	γ (°)	Work Function (eV)	Δz^{surf}	Δz^{surf} - Δz^{bulk}
K_2PTCDA	$\begin{pmatrix} 3 & 0 \\ 1 & 6 \end{pmatrix}$	2.9718, 2.8690	118.03	4.46	2.36	-0.06
K_4PTCDA	$\begin{pmatrix} 7 & 6 \\ 1 & 7 \end{pmatrix}$	2.9799, 2.9173	120.96	4.49	2.39	-0.05
Theory	-	2.9490, 2.9460	120.00	4.46, 4.45 [148]	2.38	-0.03
Experiment	-	-	-	4.46 [149], 4.5 [150], 4.74 [151]	-	-0.06 [152]

Figure 4.4: A schematic of PTCDA molecule. O_{carb} are the carboxylic oxygen atoms, O_{anhy} are the anhydride oxygen atoms, C_{func} are the carbon atoms attached to the oxygen atoms and the rest of the carbon atoms are the ones belonging to the perylene core, C_{pery}.

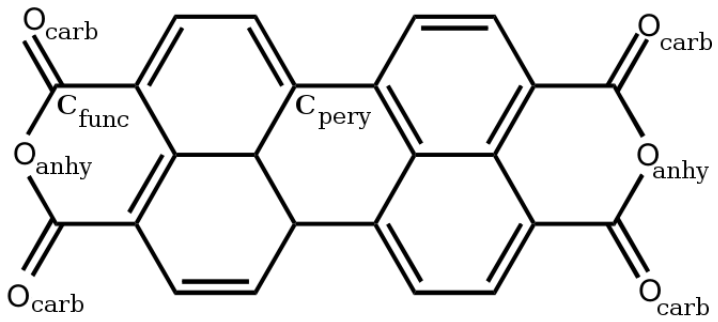

hollow) has moved to hcp hollow site as a result of the interaction between them. At the end of optimization, the distance between the two K atoms had decreased and the height of the two K atoms from the Ag(111) surface has increased compared to the starting geometry thereby indicating more interaction between the two K atoms than between K and Ag atoms. In order to analyse in detail the chemical scenario at the interface we can have a look at Figures 4.5(a) and (b), the 3D charge rearrangements computed by using the equation 3.2. We can see that there is a loss of electron density on the topmost layer of Ag atoms followed by a huge gain in electron density above the topmost layer. The K atoms are deprived of electron density which is possibly due to the donation of electronic charge to the interfacial. In the case of PTCDA in the K_2PTCDA unit cell, the Pauli push-back effect is evidently seen as a huge loss of electron density just above the topmost layer and a small gain in electron density on the topmost layer (Figures 4.5(c) and (d)). The plane of carbon atoms of PTCDA molecule as explained in Ref.

[148] has lost electron density while regions above and below the molecular plane gain electron density. They have mentioned therein the reason as the σ system of PTCDA loosing electrons and the π-system gaining electrons as in the case of flat lying π-conjugated molecules. I have also calculated the PTCDA in its herringbone motif on pristine Ag(111) (not shown here). In the case shown in Figures 4.5(c) and (d) the oxygen atoms are much closer to the Ag surface (by 0.2 Å) compared to the herringbone arrangement. The change in work function of Ag for these two cases are reported in Table 4.7.

Now we are in a position to start optimizing the K_2PTCDA phase by putting both the 2K atoms and PTCDA together at relative positions adopted from the experimental images (with some initial clues from the calculations mentioned before). This structural arrangement was optimized by keeping the bottom three layers of Ag fixed. The optimized structure obtained for the K_2PTCDA is shown in Figure 4.6. We can observe that the molecule is bend into a U-shape. In the absence of K atoms, PTCDA follows herringbone motif on Ag(111) with the molecular backbone bend into a very shallow inverted U-shape where the carboxylic oxygens (O_{carb}, see Figure 4.4) are bent towards the silver surface (not shown here but similar to the Figure fig:first(c)). This is as a result of the covalent bonding between mainly the O_{carb} and Ag even if the primary bonding is due to the vdW interactions existing through the π-system of the perylene backbone [142, 153, 141]. In the presence K atoms the herringbone arrangement of PTCDA is altered and transformed into K_2PTCDA as previously mentioned and the added K interacts with the carboxylic and anhydride (O_{anhy}, see Figure 4.4) oxygen atom of PTCDA, thereby decoupling and pulling them away from Ag (reason for the U-shape). Hence, now the K atoms act as the bonding channel between the O_{carb} and Ag atoms (Figure 4.6). The adsorption heights for the different

Figure 4.5: Side and top views of the 3D charge rearrangements obtained for the optimized structures of 2K ((a) and (b)) and PTCDA ((c) and (d)) separately in the modified K_2PTCDA Ag unit cell (for an isovalue = 0.006 e/Å^3). K atoms are shown with magenta, Ag atoms with dark grey, C with yellow, hydrogen with blue and oxygen with red balls respectively.

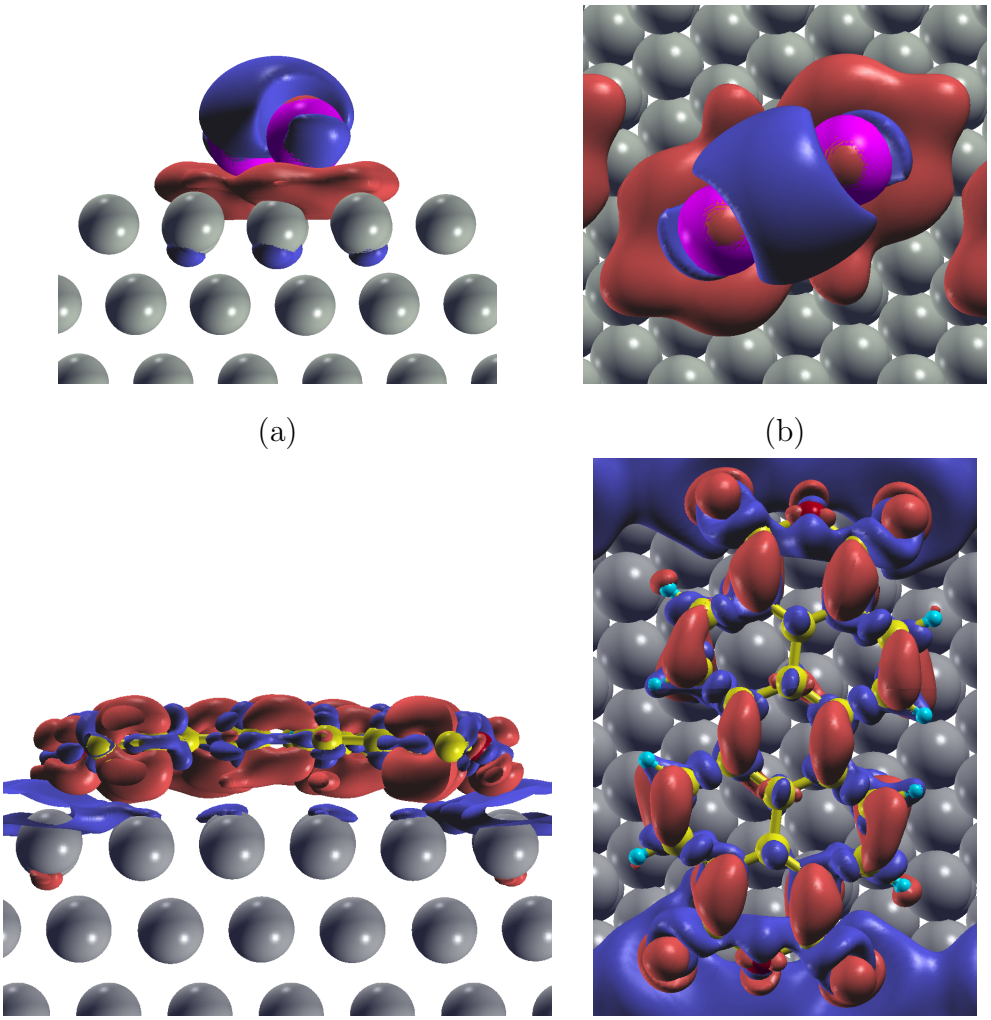

(a) (b)

(c) (d)

Figure 4.6: (a) Side and (b) top views of the optimized structure obtained for K_2PTCDA. K atoms are shown in green colour from hereafter. Taken from Zwick, Baby et al. Ref. [73].

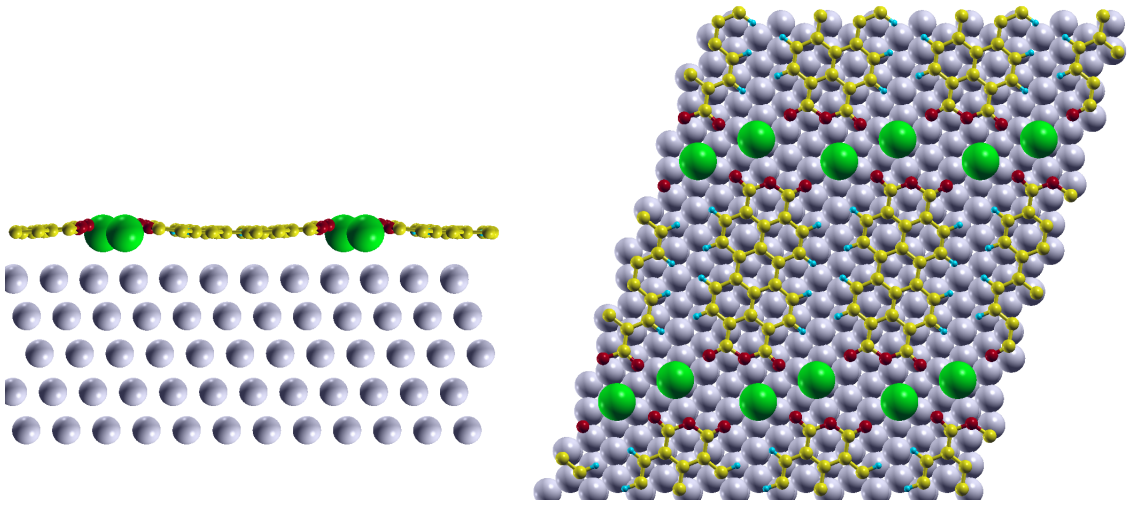

(a) (b)

atomic species are reported in Table 4.5.

Next we optimized the structure for the second doping stage K_4PTCDA. However, the estimation of the starting geometry requires determining of stoichiometry. But in this case relying on the contrast of the STHM alone (Figure 4.2(g)) is error-prone since five bright features per PTCDA molecule are perceived which exceeds the estimated potassium content. Instead the contrast of the STM image shows only one prominent feature in between the molecules which seems to be contradictory to the STHM measurements (Figure 4.8(2)(a) and (c)). In this case, it is indeed indispensable to compare

the experimental data to optimized structures obtained from DFT calculations. And so we constructed a commensurate unit cell as close as possible to the experimentally determined one for the stoichiometries x = 3, 4 and 5. The unit cell contained 2 PTCDA molecules and 6, 8, and 10 potassium atoms, corresponding to the K_3PTCDA, K_4PTCDA, and K_5PTCDA phases as a result of using the epitaxy matrix $\begin{pmatrix} 7 & 6 \\ 1 & 7 \end{pmatrix}$ as already discussed. The optimization of a hypothetical K_5PTCDA results in a structure where some K atoms move underneath the PTCDA, thereby tilting the molecules (Figures 4.7(e) and (f)). This clearly contradicts the experimental observation of flat-lying molecules. The structurally optimized configuration with three potassium atoms does not show the same symmetry as the experimental data since the third K atom is positioned (alternatively) above or below the expected position of the visible central feature and hence misses two feature (see Figures 4.7(a) and (b)). The optimized structure obtained for K_4PTCDA is shown in Figures 4.7(c) and (d) but extra steps are required to check if this is in agreement with the experiments. In order to compare the stabilities of these three configurations, first of all we did an adsorption energy analysis.

As only in the K_2PTCDA unit cell there was a single PTCDA and in all the other unit cells there were two molecules, we decided to compute the adsorption energy, E_{ads} here per molecule as defined using the equation 4.3, where $E(total)$ is the total energy of the system, $E(Ag)$ is that of the Ag substrate, N is the number of PTCDA molecules in the unit cell, $E(PTCDA)$ is the energy of the free molecule, M is the number of K atoms in the unit cell and $E(K)$ is the energy of a single free K atom. "The values obtained for the different phases are given in Table 4.4. The one obtained for the K_2PTCDA phase is 11.61 eV, which is significantly larger than for phases of PTCDA in the well-known herringbone structure (4.01 eV per molecule) and

Figure 4.7: Side and top views of the optimized structures obtained for K_3PTCDA ((a) and (b)), K_4PTCDA ((c) and (d)), and K_5PTCDA ((e) and (f)). Taken from Zwick, Baby et al. Ref. [73].

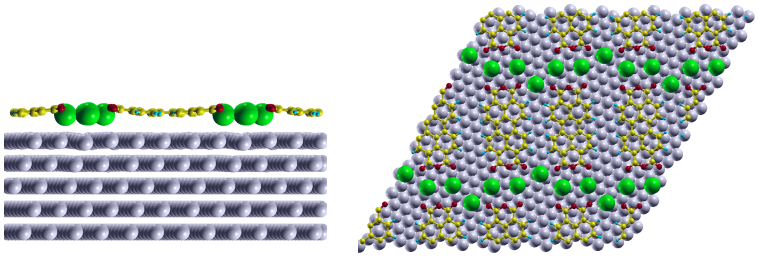

(a) (b)

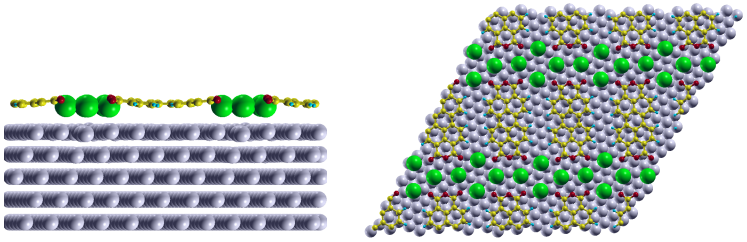

(c) (d)

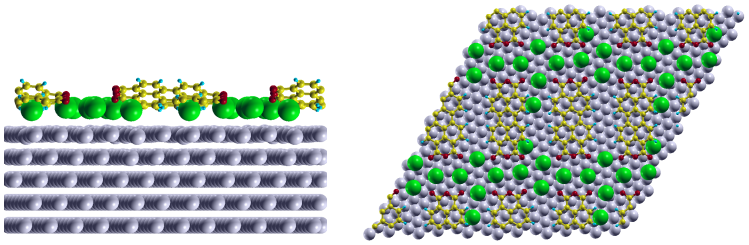

(e) (f)

for the K atoms far apart from each other (2.49 eV per K atom), pointing to an energy gain due to the intercalation, which amounts to 2.62 eV per PTCDA molecule. Such a strong bonding between the K atoms and PTCDA molecules in the monolayer can be associated with the efficient formation of the ordered K_2PTCDA phase even without annealing"[5].

$$E_{ads} = \frac{1}{N}(E(total) - E(Ag) - N.E(PTCDA) - M.E(K)) \tag{4.3}$$

The adsorption energies for the different stoichiometries also provide insight into the formation of the different phases. Having half of the surface covered by a K_2PTCDA layer and half by a K_4PTCDA layer is energetically favorable by 0.42 eV per PTCDA molecule over a homogeneous K_3PTCDA coverage. This is in excellent agreement with the above-described experiments. In contrast, at higher K coverages (4 potassium atoms per PTCDA molecule) a homogeneous K_4PTCDA layer is by 0.59 eV per molecule more stable than the coexistence of K_3PTCDA and K_5PTCDA domains [73]. All these point towards the particular stability of K_4PTCDA which is hence the next stable phase formed following K_2PTCDA, with continued K deposition. The average adsorption heights of the different atomic species present in K_4PTCDA are given in Table 4.5.

4.3.3 ST[H]M

The STM images were simulated by integrating the local density of states between the Fermi energy (E_F) and the Fermi energy plus the applied tunneling bias (V_T) following the Tersoff-Hamann approach [68]. The integrated density of states (DOS) was then averaged over more than 300 real-space grid

[5]taken from Zwick, Baby et al. Ref.[73]

Table 4.4: The adsorption energy E_{ads} per molecule calculated using equation 4.3. The PTCDA/Ag(111) mentioned here is in the herringbone phase on pristine Ag. Taken from Zwick, Baby et al. Ref. [73].

Phases	$E(total)$ (eV)	$E(Ag)$ (eV)	N	$E(PTCDA)$ (eV)	M	$E(K)$ (eV)	E_{ads} (eV)
$K/Ag(111)$	-118.62	-116.00	0	-287.72	1	-0.12	-2.49
$PTCDA/Ag(111)$	-1009.14	-425.40	2	-287.72	0	-0.12	-4.01
K_2PTCDA	-531.32	-231.74	1	-287.72	2	-0.12	-11.61
K_3PTCDA	-1160.50	-554.95	2	-287.72	6	-0.12	-14.69
K_4PTCDA	-1168.60	-554.95	2	-287.72	8	-0.12	-18.61
K_5PTCDA	-1174.32	-554.95	2	-287.72	10	-0.12	-21.35

Table 4.5: The calculated average adsorption heights of different atomic species present in herringbone PTCDA/Ag(111), K_2PTCDA and K_4PTCDA phases. C_{pery} is the average height of the carbon atoms in the perylene core, C_{func} is the average height of the functional C atoms, O_{anhy} and O_{carb} are the average heights of anhydride and carboxylic oxygen atoms and K is the average height of the potassium atoms (See Figure 4.4 for a schematic of PTCDA molecule). The PTCDA/Ag(111) mentioned here is in the herringbone phase on pristine Ag.

Phases	C_{pery} (Å)	C_{func} (Å)	O_{anhy} (Å)	O_{carb} (Å)	K (Å)
PTCDA/Ag(111)	2.73	2.71	2.76	2.59	-
K_2PTCDA	2.85	3.08	3.17	3.17	2.74
K_4PTCDA	3.04	3.34	3.43	3.45	2.72

points on the surface of a hemispherical tip with a diameter of 2.0 Å (Courtesy: Oliver T. Hofmann) [154]. The z-coordinate of the apex of such a model tip, for which the averaged DOS displays a given value (isovalue) was plotted as a function of the lateral position (x, y) as a color map to reproduce the constant current images (Courtesy: Guido Fratesi). The Tersoff-Hamann approach [68, 69] provides a first approximation of the STM images assuming an s-type tip wave function. It should be noted that the assumptions made in the Tersoff-Hamann approach should not be confused with the properties of actual electronic states at the tip. Quoting the original paper by Tersoff and Hamann, "*the s-wave treatment here is not intended as an accurate description of a real tip, but rather as a useful way of parameterizing the effect of finite tip size*" [69]. This approximation is rather done, as the tunnelling matrix element becomes particularly simple, when treating the tip "*as a locally spherical potential well where it approaches nearest the surface*" and then considering only the solution with an s-type angular momentum. Another reason why a strictly atomistic interpretation of the s-type tip wave function is not useful here is the averaging procedure we applied. Still, applying the Tersoff-Hamann approach is useful for obtaining qualitative and here also semi-quantitative insight. This is because at a reduced tip to sample distance it can be viewed as the simplest model of a tip providing atomic resolution.

In this work the tunneling conditions used for STHM comprise of sufficient contributions from the local electron density of states. And hence the images simulated using the Tersoff-Hamann approach can be used to compare with these STHM images. However, for a fully quantitative understanding of STHM higher angular momentum contributions (for example p-type wave functions) can become relevant as well [75]. "Indeed, when comparing

the simulation in Figure 4.8(1)(b) with the experimental ST[H]M images of Figure 4.8(1)(a) and (1)(c) distinct similarities can be found. While the experimentally determined basis is clearly reproduced by the calculations, the features corresponding to PTCDA and K need to be discussed further. The simulated STM image reveals that the strongest features stem from the C-C bonds near the PTCDA anhydride groups. This might also be inferred from the experimental STM image in Figure 4.8(1)(a); however, the experimental features are strongly broadened and, consequently, the potassium atoms remain unresolved. In contrast, most of the intramolecular details from the calculation are clearly visible in the STHM image in Figure 4.8(1)(c), which supports the general assignment of the surface unit cell. We observe distinct spot-like features stemming from the in-plane incorporated potassium as well as features deriving from PTCDA. In comparable STHM experiments on a $K_{0.5}$PTCDA phase on Au(111) the K atoms were not resolved directly [72]. The experimentally characterized K_2PTCDA structure (shown in Figure 4.2(d)) fully agrees with the geometry-optimized structure obtained from DFT, Figure 4.6. This also implies that most likely no further potassium is situated underneath or on top of the PTCDA layer, when comparing with the experimental observation described above. Furthermore, the DFT analysis shows that upon K intercalation the oxygens of the functional groups of PTCDA tend to bend away from the surface as discussed in the previous section, an effect that has been observed experimentally for K intercalated PTCDA on Ag(110) in a similar way [34]. In passing we note that the STHM contrast can indeed be tuned to improve the submolecular resolution of PTCDA even further, however, at the expense of the visibility of K atoms in the same scan"[6].

[6]taken from Zwick, Baby et al. Ref.[73]

It can be observed that the experimental image (Figure 4.8(2)(a)) has been reproduced very well by the calculated constant current STM picture for K_4PTCDA (Figure 4.8(2)(b)). The K atoms are located near the anhydride groups of PTCDA as seen in Figure **??**, similar to the K_2PTCDA phase. However, as the K concentration is higher in the current K_4PTCDA case, not all K atoms attain equivalent positions in the unit cell. In STHM two nonequivalent positions of K with respect to PTCDA are observed: the first (K_A) in between two molecules along $\mathbf{a_2}$, with carboxylic and anhydride oxygen atoms as neghbours; and the second (K_B) in between two molecules along $\mathbf{a_1}$, in the vicinity of carboxylic oxygen atoms only (Figure 4.8(2)(a)). The K_A positions bear resemblance to the K_2PTCDA case, where the K atoms have a carboxylic and an anhydride oxygen as nearest neighbors in one of the adjacent PTCDA rows. Interestingly the very specific details observed in STHM are reproduced also in the simulations (such as the inner structure of PTCDA) where the most intense features can be related to C-C bonds near the carboxylic oxygen atoms (as in the case of K_2PTCDA). Now we will discuss the most prominent and intriguing feature localized in between four neighboring PTCDA molecules as visible in the experimental STM image that has a broad and blurred appearance. In the STM simulation a very identical feature at and in between the actual K positions is observed, which matches the experimental data perfectly (Figure 4.8(2)). A similar observation has been reported previously where multiple adatoms are imaged as a single feature in experimental and simulated scanning tunneling topographies, for Cu dimers in the template growth of metal-organic chains on Cu(110) [155]. The Tersoff-Hamann-based STM simulations originate from a calculation of the density of states between E_F and the energy corresponding to the given tip bias V_T and so the positive tip bias used here

implies that the tunneling occurs through the unoccupied states which in turn means that there is a significant unoccupied density of states in the region between the K atoms somewhat above E_F. More about the nature of this very interesting density of unoccupied states will be discussed in the next section.

"Comparing the simulated and experimental STM images to the STHM image (Figure 4.8(2)(c)), notable differences arise for the actual visibility of the K atoms. While the four potassium atoms are individually resolved only in the STHM image, a fifth bright "ghost feature" is simultaneously visible in between the identified K positions, though significantly more narrow and less intense than in the STM measurements and simulations. This is attributed to the fact that for the chosen parameters the contrast obtained by STHM is not purely topographic, but to a certain extent also electronic (as evidenced by the nice agreement of the submolecular contrast between experimental STHM and simulated STM image discussed above). Consequently, it constitutes a remnant of the intense, blurred feature observed in the genuine STM mode and we emphasize that without the DFT calculations this "ghost feature" is easily mistaken for a fifth K atom. Accordingly, the structure of the adsorbate can be described by a monomolecular unit cell that contains four potassium atoms per PTCDA which justifies the above designation of this structure as K_4PTCDA, neither K_3PTCDA nor K_5PTCDA. The simulated STM images obtained for K_3PTCDA and K_5PTCDA are shown in Figure 4.6 which are clearly not in agreement with the experimental images shown in Figures 4.8(2)(a) and (c)"[7].

[7]taken from Zwick, Baby et al. Ref.[73]

Figure 4.8: Experimental STM, simulated STM and experimental STHM images obtained for (1) K_2PTCDA and (2) K_4PTCDA phases. Taken from Zwick, Baby et al. Ref. [73].

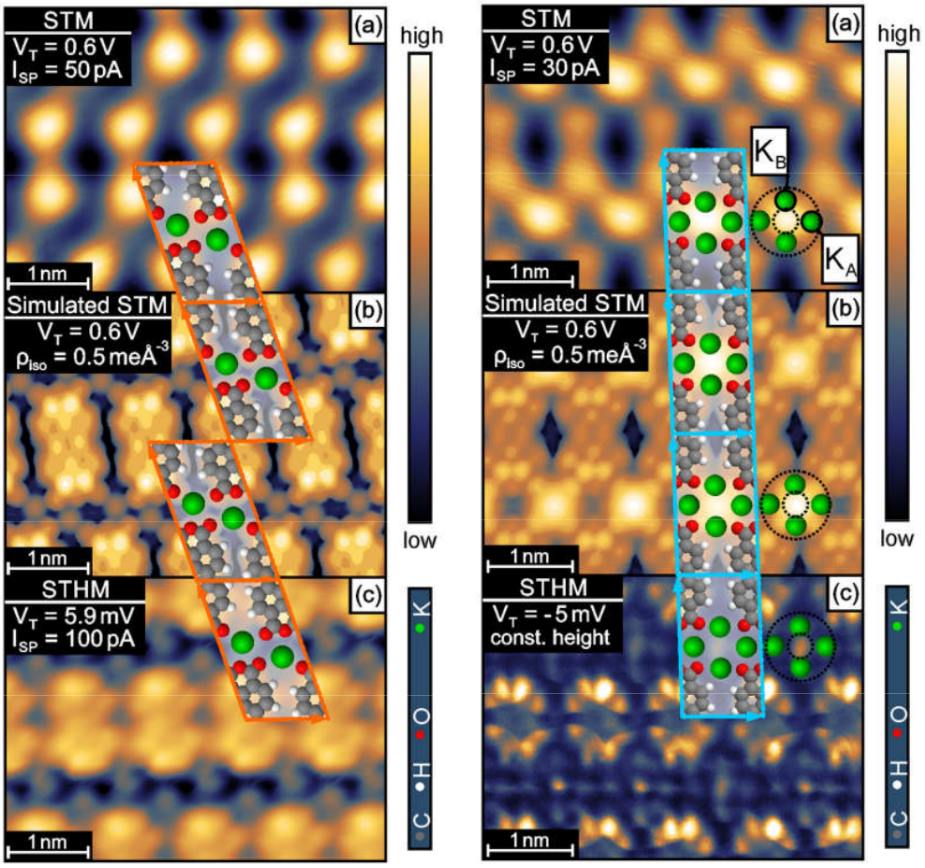

(1) (2)

Figure 4.9: Simulated STM images obtained for (a) K_3PTCDA at $V_T = 0.6$ V and $\rho_{iso} = 0.3$ me/Å^3 and (b) K_5PTCDA at $V_T = 0.8$ V and $\rho_{iso} = 0.3$ me/Å^3. Taken from Zwick, Baby et al. Ref. [73].

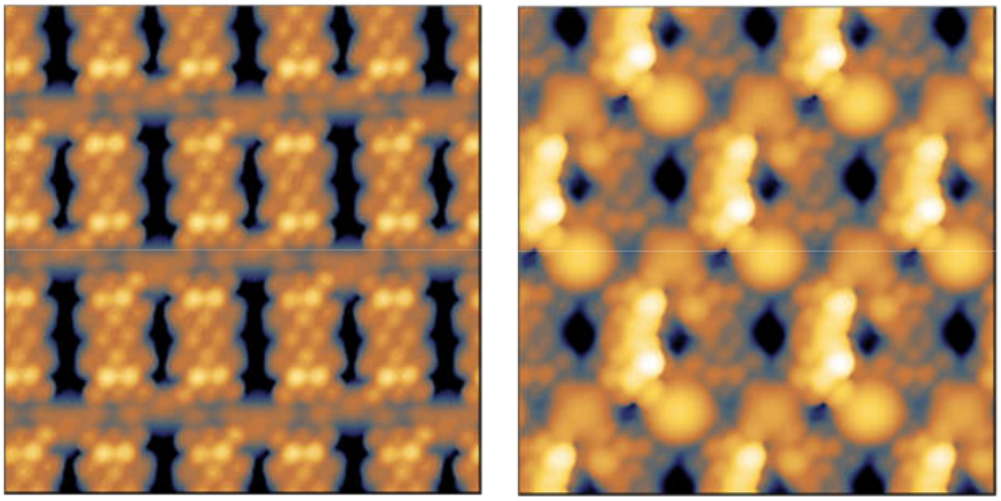

(a) (b)

4.3.4 Electronic Structure and Charge Transfer Analysis

After the identifying and confirming the second doping stage as K_4PTCDA from the adsorption energies and STM simulations, we proceeded by analysing the electronic properties of the two stable doping phases K_2PTCDA and K_4PTCDA. To this respect we calculated the MOPDOS using the *ab initio* molecular simulations computer program package FHI-aims [156]. In the case of PTCDA adsorbed on Ag(111), the LUMO is filled to a significant extent and hence pinned to the Fermi energy level, an effect that is well documented in experiments [157, 158], and in simulations [148] (not shown here). Therefore PTCDA is known to exhibit this kind of metallic behaviour when adsorbed on Ag(111). In the K_2PTCDA phase the PTCDA LUMO-derived state gets completely filled due to the charge transfer from the K atoms as seen in the MOPDOS of Figure 4.10(a) and shifts more than half an eV below the Fermi level thereby showing a metal to semiconductor phase transition on K doping (as no states are present at the E_F anymore). While in the case of K_4PTCDA phase, we observe that the LUMO+1 is completely hybridized and spread over a large energy range of approx. 3 eV and the LUMO+2 is shifted to lower energy such that it onsets at E_F (see Figure 4.10(b)).

The three dimensional charge rearrangement isodensity plots for both K_2PTCDA and K_4PTCDA phases are shown in Figure 4.11. This has been computed by using the equation 3.2. A huge electronic charge accumulation can be observed in between the K atoms and the underlying Ag in the case of K_2PTCDA (Figure 4.11(a), (b)). For K_4PTCDA phase, it can be seen that the K atoms are clearly depleted of electrons and that the PTCDA gains electronic charge (Figure 4.11(c), (d)). Note that the different isovalues were to be chosen for better visualization of the two cases (choosing the

Figure 4.10: MOPDOS obtained for (a) K_2PTCDA and (b) K_4PTCDA phases.

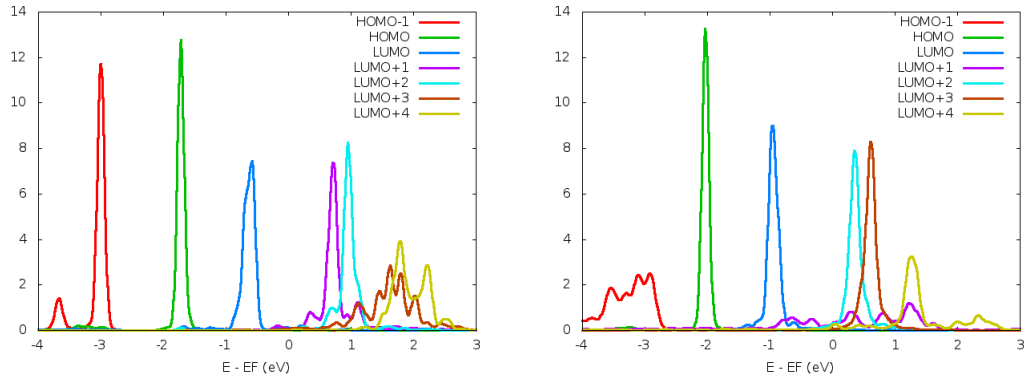

(a) (b)

same isovalue of K_2PTCDA for K_4PTCDA resulted in extremely smeared out images due to the excessive charge rearrangements occurring in the latter compared to the former).

The quantitative charge-transfer analysis can be carried out by looking into the molecular and atomic charges of the adsorbate layer. For this purpose, I did the Löwdin charge partitioning scheme [114, 115] as implemented in Quantum Espressso. The optimized structures obtained from VASP 5.3.3. was used to do the Quantum Espresso calculations, followed by the Löwdin charge analysis. In the case of K_2PTCDA phase, each PTCDA has 1.3 electrons more and each K has 0.7 electrons less. So, the two K atoms together lose 1.4 electrons out of which 1.3 is gained by the PTCDA and only 0.1 lost electron/molecule is attributed to the Ag substrate thereby reducing its work function by 0.64 eV. Whereas in the K_4PTCDA phase each PTCDA has 1.4 excess electronic charge and each K is deprived of 0.6 electrons. So,

Figure 4.11: (a) Side and (b) top views of 3D charge rearrangement plot (for an isovalue = 0.006 e/Å^3) for K_2PTCDA, and (c) side and (d) top views of the same for K_4PTCDA (for an isovalue = 0.06 e/Å^3). Red colour indicates accumulation and blue colour indicates depletion of electrons.

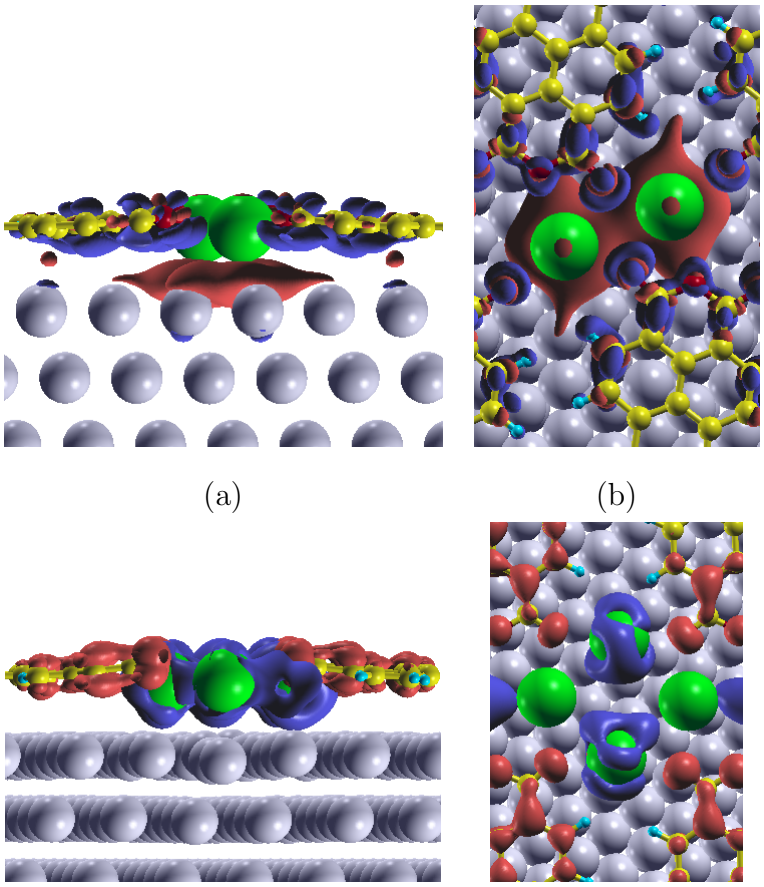

(a) (b)

(c) (d)

the four K atoms altogether lose 2.4 electrons out of which 1.4 electrons is taken by the PTCDA and the remaining 1.0 electron/molecule is assigned to the Ag substrate. This huge charge transfer reduces the work function of Ag by -1.42 eV.

In addition to the Löwdin charge analysis, a Bader Charge Analysis [159] based on the charge densities calculated with VASP was also performed (done by Elisabeth Verwüster) [8]. The Bader analysis reveals that the negative charge on each PTCDA molecule increases upon depositing potassium, i.e., the charge per molecule increases from 1.1 electrons for undoped PTCDA/Ag(111) via 1.7 electrons per molecule for K_2PTCDA to 1.9 electrons per molecule in K_4PTCDA. In the undoped PTCDA/Ag(111) case the electrons transferred to PTCDA originate from the Ag substrate, whereas the net charges on the Ag atoms are apparently hardly affected by the interaction with the adsorbate in K_2PTCDA, i.e., there the negative net charge on PTCDA directly comes from the K atoms (each K loses around 0.78 electrons) and the Bader charge on the Ag substrate is negligibly small. While in the case of K_4PTCDA each K atom loses around 0.8 electrons which gives rise to an increased electron density in the Ag substrate (1.1 electrons per K_4 cluster in the K_4PTCDA phase). Concluding we can say that both the analysis (Löwdin and Bader) are in good agreement with each other, but the different partitioning schemes employed in these two methods give a difference of around 0.2 to 0.3 electrons in the end results obtained using these two.

[8] Version 0.95 of the Bader Charge Analysis code released by the Henkelman group was used [160, 161, 162, 163]. Before performing this analysis, the VASP calculations were reran applying the aedens module in order to write out also the core-densities from the PAW calculations and very accurate settings were used especially for enforcing a more dense mesh in the FFT (Fast Fourier Transform) procedure.

Figure 4.12: LUMO of a K_4^{+4} four-fold positively charged cluster (K is represented by purple balls).

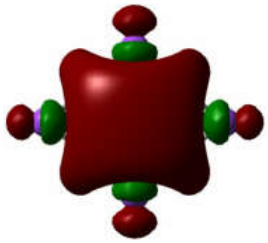

As deduced from the simulated STM image in the previous section, to understand the nature of the huge density of unoccupied states at the center of the four K atoms, a K_4 cluster was constructed by arranging the atoms at exactly the same positions at which they are present in the optimized structure of K_4PTCDA. Looking into the electronic properties of such a K_4 cluster resulted in the HOMO-1 of the cluster characterized by a significant amplitude in the wave function right at the center of the four K atoms [9]. As per the Bader charge analysis before, assuming a charge transfer of approximately one electron per K atom to the PTCDA layer and the Ag(111) substrate, this state becomes the LUMO of the K_4^{+4} cluster which undergoes hybridization and is broadened on the Ag surface. The respective LUMO of the four-fold positively charged cluster is shown in Figure 4.12. It can be seen that the LUMO of K_4^{4+} is a bonding one, in phase superposition of potassium hybrid orbitals, which is characterized by a massive charge density at the center of the four K atoms strongly reminiscent of the feature seen in STM. The LUMO of the K_4^{4+} cluster (Figure 4.12) is reproducible also when

[9]The calculations on the K_4 clusters were performed by Prof. Egbert Zojer using Gaussian09 [164] and employing the PBE [46] functional in conjunction with the 6-311G(d,p) basis set [165].

Table 4.7: The calculated change in work function, $\Delta\phi$ for the different cases investigated.

Phases	$\Delta\phi$ (eV)
2K in K_2PTCDA cell (as in Figure 4.5(a))	-1.89
PTCDA in K_2PTCDA cell (as in Figure 4.5(c))	0.16
K_2PTCDA	-0.64
K_3PTCDA	-1.02
K_4PTCDA	-1.42
K_5PTCDA	-1.49

using a hybrid-functional (here B3LYP).

Finally I report in Table 4.7 the change in work function for the cases investigated so far. The values are in agreement with the charge transfer analysis for the respective cases.

Chapter 5

Conclusions

Metal-organic interfaces are present in any organic electronic device and studying these hybrid junctions will help in understanding and modelling new interfaces and also improving the efficiency of the existing ones. In this thesis, I have investigated two systems using DFT methods namely (i) pentacene/Al(001) and (ii) K doping of PTCDA/Ag(111). In the case of pentacene/Al(001), our calculations have shown that the interface is characterized by a single geometric and electronic configuration of the molecule where the molecule is bent into a V-shape. This occurs due to the anchoring of its two central carbon atoms to a pair of Al atoms underneath, an effect never reported before which facilitates the LUMO filling. This direct C-Al bonding is obtained only by the inclusion of van der Waals interactions in the theoretical calculations. The most stable adsorption configuration is an Al-bridge site where the long molecular axis is oriented along the [110] direction. Ordered islands are formed by the molecules in the experiment facilitated by a molecule-induced surface reconstruction. The V-shaped conformation is also found for a hollow site where the long molecular axis is oriented along the [100] direction. The molecules are also adsorbed at small terraces and

at defects (as seen in the STM), which are largely present on Al(001) in the standard preparation conditions, and exhibit the V-shape.

We obtain a narrowing of the XPS spectrum for the adsorbed molecules (at the most stable site) which which is explained by the broadening induced by charge transfer, and a narrowing due to the excitation-site dependent screening. The absence of LUMO in the NEXAFS spectra confirms the strong interaction of the molecule with the Al substrate resulting in hybridization and filling of the former, additionally facilitated by the V-shape. Another interesting result is the reduction in the azimuthal dichroism (associated with the energy splitting of the σ resonances) due to the modified C-C bond lengths observed in the NEXAFS.

In the case of the second system, the alkali metal doping of an adsorbed organic monolayer was studied. Potassium was evaporated onto pristine PTCDA monolayer domains on Ag(111) (submonolayer coverage) by the experimental group. The experimentalists observed the formation of self-organized structures of the K-intercalated layers. Two new and stable K_xPTCDA phases for $x = 2$ and 4 stoichiometries could be achieved without any annealing. By combining the DFT calculations that I performed during my secondment at Graz University of Technology, Austria with complementary experimental (LEED, ST[H]M) methods, we were able to understand the atomistic details of the formed phases and their stability. The potassium atoms adsorbed in between the molecules initiate the restructuring process of the PTCDA molecules, leading to a complete conversion of the initial herringbone arrangement into the K_2PTCDA phase. At higher K concentration this is then followed by the formation of a second stable phase named K_4PTCDA. The stoichiometry for this second doping stage was correctly determined only after confronting the ST[H]M features with the simulation

results. In both the phases the K atoms adsorb near the functional groups of PTCDA. The PTCDA LUMO-derived states get filled with increasing K concentration, while K loses electrons in both cases and especially in the K_4PTCDA phase. This results in a huge density of unoccupied states which contributes to a major and very interesting feature in the ST[H]M images.

Appendix A

Quantum Espresso

Quantum Espresso (QE) stands for Quantum opEn Source Package for Research in Electronic Structure Simulation and Optimization. It is a free and open source software distribution of packages used for running DFT based simulations to perform self-consistent electronic structure calculations, structure relaxations, molecular dynamics calculations, and materials modelling [66]. The Kohn-Sham (KS) equation as given in equation 2.3 is solved self-consistently for a set of fixed nuclear positions. Plane wave basis sets are used to represent the system wavefunctions. The ionic potential (nucleus+core electrons) is provided by the pseudopotential (PP). PPs could be Norm-conserving, Ultrasoft or Projected Augmented Wave (PAW) type. The LDA, GGA, hybrid functionals and van der Waal's corrected functionals are available [66]. Like in most DFT codes periodic boundary conditions are used also here. i.e. the unit cell is repeated in all the three directions as in a crystal. So, to do calculations of isolated molecules, a very large unit cell is to be used. And if one needs to simulate for example a slab, the unit cell employed should be larger only in one particular direction in which the interaction is to be minimized.

Iterative diagonalization is performed by using Davidson or conjugate gradient method in order to solve the KS equation 2.3 [66]. Self-consistency is achieved via the modified Broyden method of [166]. Finally, the structural optimizations are performed by using the Broyden-Fletcher-Goldfarb-Shanno (BFGS) quasi-Newton algorithm [66].

Appendix B

Vienna Ab Initio Simulation Package (VASP)

The Vienna Ab Initio Simulation Package (VASP) is a plane wave package similar to Quantum Espresso, used to perform quantum mechanical calculations [167, 145]. PPs or the PAW method is used. VASP 5.3.3 version is used for this work in conjunction with the geometry optimizer GADGET [146]. Even though VASP itself provides routines to perform geometry optimizations of periodic systems, the VASP-based optimizer GADGET [146] was used in this work to run full geometry optimizations. One of the reasons for this choice was that VASP uses Cartesian coordinates for the optimization while GADGET performs the optimization in internal coordinates. Performing the optimization using internal coordinates is more efficient and leads to more realistic results compared to an optimization in Cartesian coordinates especially with regard to the tilting of upright standing molecules [146].

The VASP input files are: `INCAR` which contains the input parameters required for the simulation, `POSCAR` contains the positions of the atoms within the unit cell, `KPOINTS` contains the k-points mesh and `POTCAR` that contains

the PPs for each atomic species present in the system. In addition to these four if one is using GADGET, another input file namely `INPDAT` containing the simulation parameters for GADGET is needed. The main output file is the `OUTCAR` file. Other files are `CONTCAR` that contains the optimized coordinates, `OSZICAR` containing the converged forces and energies, `WAVECAR` containing the wavefunctions and `CHGCAR` containing the charge density.

Appendix C

Molecular Orbital Projected Density of States (MOPDOS)

The contributions from the orbitals of the free molecule to the density of states of an adsorbed system can be determined by performing the Molecular Orbital Projected Density of States (MOPDOS). The procedure to compute the same, as we have implemented in `molecularpdos.x` within Quantum ESPRESSO is described here. In more general terms, one can analyze the electronic structure of a given system named "A" (here, the molecule/substrate interface) in terms of the energy levels of a part of it named "B" (here, the molecule). This approach may also be used to analyze a complex molecule in terms of its subunits, or a different electronic configuration (say, A is the molecule with a core-level excitation while B is the same but in the ground state as we did to study excitations of pentacene [64]).

If we indicate by $|\psi^A_{n_a\mathbf{k}}\rangle$ the eigenvectors of system A and by $\epsilon^A_{n_a\mathbf{k}}$ its eigenvalues (same for system B), where $\mathbf{k}$ is the k-vector in the Brillouin zone with weight $\omega_{\mathbf{k}}$, the MOPDOS of system A, projected onto the n_b-th

orbital of system B and evaluated at the energy E reads:

$$MOPDOS_{n_b}(E) = \sum_{n_a\mathbf{k}} \omega_{\mathbf{k}} \, |\langle \psi^B_{n_b\mathbf{k}} | \psi^A_{n_a\mathbf{k}} \rangle|^2 \, \delta(E - \epsilon^A_{n_a\mathbf{k}}). \tag{C.1}$$

The eigenstates are computed by separate `pw.x` calculations (in the PWscf package of Quantum Espresso) for A and B; for consistency, the same unit cell and $\mathbf{k}$ sampling should be used. A shortcoming of the plane wave representation is that direct evaluation of the overlap integral $|\langle \psi^B_{n_b\mathbf{k}} | \psi^A_{n_a\mathbf{k}} \rangle|^2$ requires handling the full states for the two systems, which can be computationally demanding already for a moderately large unit cell. Our implementation instead goes through a more efficient local basis set representation of the system. Let us indicate by $|\phi^{nlm}_I\rangle \equiv |\phi_\nu\rangle$, with $\nu = (I, n, l, m)$, the atomic wavefunction of atom I with quantum numbers n, l, and m. The number of such states, N_ϕ, is generally much smaller than that of plane waves making the calculations more manageable.

Hence we can approximate the eigenfunctions in terms of this local basis set:

$$|\psi^A_{n_a\mathbf{k}}\rangle \approx \sum_\nu P^A_{n_a\mathbf{k},\nu} |\phi_\nu\rangle \tag{C.2}$$

$$|\psi^B_{n_b\mathbf{k}}\rangle \approx \sum_\nu P^B_{n_b\mathbf{k},\nu} |\phi_\nu\rangle \tag{C.3}$$

where the coefficients P are the complex projections of the KS eigenstates onto the local basis, $P^A_{n_a\mathbf{k},\nu} = \langle \phi_\nu | \psi^A_{n_a\mathbf{k}} \rangle$ and similarly for B. The above expressions are approximate since the local basis set does not span completely the original Hilbert space (see, e.g., the "spilling" [168]) but this is often of no concern to a qualitative analysis. Within Quantum ESPRESSO, the coefficients P are computed by the `projwfc.x` code in a standard calculation of the DOS projected onto atomic orbitals and are stored in the file

`atomic_proj.xml`. The execution of `projwfc.x` has to be performed for systems A and B separately.

The orbital overlaps in Eq. (C.1) are eventually computed from Eqs. (C.2) and (C.3) as:

$$\langle \psi^B_{n_b\mathbf{k}} | \psi^A_{n_a\mathbf{k}} \rangle = \sum_\nu (P^B_{n_b\mathbf{k},\nu})^* P^A_{n_a\mathbf{k},\nu}. \tag{C.4}$$

Notice that the index ν in the summation should identify the same atomic state in the two systems for the local orbitals which are common for the two systems only. So, if system B is a subsystem of A, we have $N^A_\phi > N^B_\phi$ and the summation runs over N^B_ϕ states. In all cases, the fraction of atomic states to be used can be specified in input by appropriate variables (`i_atmwfc_beg_full/part` and `i_atmwfc_end_full/part`) such that:

`(i_atmwfc_end_full) - (i_atmwfc_beg_full) + 1` $= N^A_\phi$ and

`(i_atmwfc_end_part) - (i_atmwfc_beg_part) + 1` $= N^B_\phi$

Bibliography

[1] H. Inokuchi. The discovery of organic semiconductors. Its light and shadow. *Organic Electronics*, 7(2):62–76, 2006.

[2] M. Pope and C. E. Swenberg. *Electronic processes in organic crystals and polymers*. 1999.

[3] D.B. Mitzi, K. Chondroudis, and C.R. Kagan. Organic-inorganic electronics. *IBM Journal of Research and Development*, 45(1):29–45, 2001.

[4] S. R. Forrest. The path to ubiquitous and low-cost organic electronic appliances on plastic. *Nature*, 428:911–918, 2004.

[5] A. Tsumura, H. Koezuka, and T. Ando. Macromolecular electronic device: Field-effect transistor with a polythiophene thin film. *Applied Physics Letters*, 49(18):1210–1212, 1986.

[6] A. Hepp, H. Heil, W. Weise, M. Ahles, R. Schmechel, and H. von Seggern. Light-emitting field-effect transistor based on a tetracene thin film. *Physical Review Letters*, 91(15):157406, 2003.

[7] Y. Fukuda, T. Watanabe, T. Wakimoto, S. Miyaguchi, and M. Tsuchida. An organic led display exhibiting pure RGB colors. *Synthetic Metals*, 111:1–6, 2000.

[8] W. E. Howard. Better displays with organic films. *Scientific American*, 290(2):76, 2004.

[9] A. Facchetti. Semiconductors for organic transistors. *Materials Today*, 10(3):28–37, 2007.

[10] C. W. Tang. Two-layer organic photovoltaic cell. *Applied Physics Letters*, 48(2):183–185, 1986.

[11] P. Peumans, V. Bulović, and S. R. Forrest. Efficient photon harvesting at high optical intensities in ultrathin organic double-heterostructure photovoltaic diodes. *Applied Physics Letters*, 76(19):2650–2652, 2000.

[12] A. Bandhopadhyay and A. J. Pal. Large conductance switching and binary operation in organic devices: Role of functional groups. *The Journal of Physical Chemistry B*, 107(11):2531–2536, 2003.

[13] Y. Yang, J. Ouyang, L. Ma, R. J. Tseng, and C.-W. Chu. Electrical switching and bistability in organic/polymeric thin films and memory devices. *Advanced Functional Materials*, 16(8):1001, 2006.

[14] B. K. Crone, A. Dodabalapur, R. Sarpeshkar, A. Gelperin, H. E. Katz, and Z. Bao. Organic oscillator and adaptive amplifier circuits for chemical vapor sensing. *Journal of Applied Physics*, 91(12):10140–10146, 2002.

[15] G. Witte and C. Wöll. Growth of aromatic molecules on solid substrates for applications in organic electronics. *Journal of Materials Research*, 19(07):1889–1916, 2004.

[16] S. R. Forrest and M. E. Thompson. Introduction: Organic electronics and optoelectronics. *Chemical Reviews*, 107(4):923–925, 2007.

[17] G. R. Dholakia, M. Meyyappan, A. Facchetti, and T. J. Marks. Monolayer to multilayer nanostructural growth transition in n-type oligothiophenes on Au (111) and implications for organic field-effect transistor performance. *Nano Letters*, 6(11):2447–2455, 2006.

[18] L. Floreano, A. Cossaro, D. Cvetko, G. Bavdek, and A. Morgante. Phase diagram of pentacene growth on Au (110). *The Journal of Physical Chemistry B*, 110(10):4908–4913, 2006.

[19] M. Pedio, B. Doyle, N. Mahne, A. Giglia, F. Borgatti, S. Nannarone, S. K. M. Henze, R. Temirov, F. S. Tautz, L. Casalis, et al. Growth of pentacene on Ag (111) surface: A NEXAFS study. *Applied Surface Science*, 254(1):103–107, 2007.

[20] A. Ferretti, C. Baldacchini, A. Calzolari, R. Di Felice, A. Ruini, E. Molinari, and M. G. Betti. Mixing of electronic states in pentacene adsorption on copper. *Physical Review Letters*, 99(4):1–4, 2007.

[21] K. Müller, A. P. Seitsonen, T. Brugger, J. Westover, T. Greber, T. Jung, and A. Kara. Electronic structure of an organic/metal interface: Pentacene/Cu (110). *The Journal of Physical Chemistry C*, 116(44):23465–23471, 2012.

[22] S. Söhnchen, S. Lukas, and G. Witte. Epitaxial growth of pentacene films on Cu (110). *The Journal of Chemical Physics*, 121(1):525–534, 2004.

[23] H. Yildirim, T. Greber, and A. Kara. Trends in adsorption characteristics of benzene on transition metal surfaces: Role of surface chemistry and van der Waals interactions. *The Journal of Physical Chemistry C*, 117(40):20572–20583, 2013.

[24] W. Liu, J. Carrasco, B. Santra, A. Michaelides, M. Scheffler, and A. Tkatchenko. Benzene adsorbed on metals: Concerted effect of covalency and van der Waals bonding. *Physical Review B*, 86(24):245405, 2012.

[25] J. Xue and S. R. Forrest. Bipolar doping between a molecular organic donor-acceptor couple. *Physical Review B*, 69(24):245322, 2004.

[26] J. Wüsten, S. Berger, K. Heimer, S. Lach, and C. Ziegler. Interaction of alkali metals with perylene-3, 4, 9, 10-tetracarboxylic–dianhydride thin films. *Journal of Applied Physics*, 98(1):013705, 2005.

[27] A. J. Heeger, A. G. MacDiarmid, and H. Shirakawa. The nobel prize in chemistry, 2000: Conductive polymers. *Stockholm, Sweden: Royal Swedish Academy of Sciences*, 2000.

[28] C. K. Chiang, C. R. Fincher, Y. W. Park, A. J. Heeger, H. Shirakawa, E. J. Louis, S. C. Gau, and Alan G. MacDiarmid. Electrical conductivity in doped polyacetylene. *Physical Review Letters*, 39:1098–1101, Oct 1977.

[29] R. Mitsuhashi, Y. Suzuki, Y. Yamanari, H. Mitamura, T. Kambe, N. Ikeda, H. Okamoto, A. Fujiwara, M. Yamaji, N. Kawasaki, et al. Superconductivity in alkali-metal-doped picene. *Nature*, 464(7285):76–79, 2010.

[30] M. F. Craciun, S. Rogge, and A. F. Morpurgo. Correlation between molecular orbitals and doping dependence of the electrical conductivity in electron-doped metal-phthalocyanine compounds. *Journal of the American Chemical Society*, 127(35):12210–12211, 2005.

[31] V. Shklover, S. Schmitt, E. Umbach, F. S. Tautz, M. Eremtchenko, Y. Shostak, J. A. Schaefer, and M. Sokolowski. Strong K-induced changes in perylene-tetracarboxylic-dianhydride films on Ag (110) studied by HREELS and LEED. *Surface Science*, 482:1241–1248, 2001.

[32] Y. Hosoi, N. Koch, Y. Sakurai, H. Ishii, T. U. Kampen, G. Salvan, Dietrich R. T. Zahn, G. Leising, Y. Ouchi, and K. Seki. Structural study of thin films of neutral and potassium-doped oligophenylenes on Cu (100). *Surface science*, 589(1):19–31, 2005.

[33] A. Tamai, A. P. Seitsonen, R. Fasel, Z-X Shen, J. Osterwalder, and T. Greber. Doping-induced reorientation of C60 molecules on Ag(111). *Physical Review B*, 72(8):085421, 2005.

[34] G. Mercurio, O. Bauer, M. Willenbockel, B. Fiedler, T. Sueyoshi, C. Weiss, R. Temirov, S. Soubatch, M. Sokolowski, and F. S. Tautz. Tuning and probing interfacial bonding channels for a functionalized organic molecule by surface modification. *Physical Review B*, 87(12):121409, 2013.

[35] H.-H. Yang, Y.-H. Chu, C.-I Lu, T.-H. Yang, K.-J. Yang, C.-C. Kaun, G. Hoffmann, and M.-T. Lin. Digitized charge transfer magnitude determined by metal–organic coordination number. *ACS Nano*, 7(3):2814–2819, 2013.

[36] Y. Hasegawa, Y. Yamada, and M. Sasaki. Reordering and disordering of the copper hexadecafluorophthalocyanine (F16CuPc) monolayer by K doping. *The Journal of Physical Chemistry C*, 118(42):24490–24496, 2014.

[37] M. Yano, M. Endo, Y. Hasegawa, R. Okada, Y. Yamada, and M. Sasaki. Well-ordered monolayers of alkali-doped coronene and picene: Molecular arrangements and electronic structures. *The Journal of Chemical Physics*, 141(3):034708, 2014.

[38] L. H. Thomas. The calculation of atomic fields. In *Mathematical Proceedings of the Cambridge Philosophical Society*, volume 23, pages 542–548. Cambridge Univ Press, 1927.

[39] E. Fermi. Un metodo statistico per la determinazione di alcune prorieta dell'atome. *Rend. Accad. Naz. Lincei*, 6(602-607):32, 1927.

[40] E. Schrödinger. An undulatory theory of the mechanics of atoms and molecules. *Physical Review*, 28(6):1049, 1926.

[41] P. Hohenberg and W. Kohn. Inhomogeneous electron gas. *Phys. Rev.*, 136:B864–B871, Nov 1964.

[42] W. Kohn and L. J. Sham. Self-consistent equations including exchange and correlation effects. *Phys. Rev.*, 140:A1133–A1138, Nov 1965.

[43] G. P. Brivio and M. I. Trioni. The adiabatic molecule–metal surface interaction: Theoretical approaches. *Reviews of Modern Physics*, 71(1):231, 1999.

[44] J. P. Perdew. Accurate density functional for the energy: Real-space cutoff of the gradient expansion for the exchange hole. *Physical Review Letters*, 55(16):1665, 1985.

[45] J. P. Perdew. Density-functional approximation for the correlation energy of the inhomogeneous electron gas. *Physical Review B*, 33:8822–8824, Jun 1986.

[46] J. P. Perdew, K. Burke, and M. Ernzerhof. Generalized Gradient Approximation Made Simple. *Physical Review Letters*, 77(18):3865–3868, 1996.

[47] S. Grimme. Accurate description of van der Waals complexes by density functional theory including empirical corrections. *Journal of Computational Chemistry*, 25(12):1463–1473, 2004.

[48] V. G. Ruiz, W. Liu, E. Zojer, M. Scheffler, and A. Tkatchenko. Density-functional theory with screened van der Waals interactions for the modeling of hybrid inorganic-organic systems. *Physical Review Letters*, 108(14):146103, 2012.

[49] A. D. Becke. Density-functional exchange-energy approximation with correct asymptotic behavior. *Physical Review A*, 38(6):3098, 1988.

[50] A. Tkatchenko and M. Scheffler. Accurate molecular van der Waals interactions from ground-state electron density and free-atom reference data. *Physical Review Letters*, 102(7):073005, 2009.

[51] E. M. Lifshitz. The theory of molecular attractive forces between solids. 1956.

[52] E. Zaremba and W. Kohn. Van der waals interaction between an atom and a solid surface. *Physical Review B*, 13(6):2270, 1976.

[53] A. Bondi. van der Waals volumes and radii. *The Journal of Physical Chemistry*, 68(3):441–451, 1964.

[54] K. Siegbahn, K. Nordling, A. Fahlman, et al. ESCA. Atomic, molecular, and solid state. *Nova Acta Regiae Societatis Scientarium Upsaliensis, Ser. IV*, 20, 1967.

[55] J. M. Hollander and W. L. Jolly. X-ray photoelectron spectroscopy. *Accounts of Chemical Research*, 3(6):193–200, 1970.

[56] S. García-Gil, A. García, and P. Ordejón. Calculation of core level shifts within DFT using pseudopotentials and localized basis sets. *European Physical Journal B*, 85(7), 2012.

[57] G. Makov and M. C. Payne. Periodic boundary conditions in ab initio calculations. *Physical Review B*, 51(7):4014, 1995.

[58] G. Fratesi, V. Lanzilotto, L. Floreano, and G. P. Brivio. Azimuthal Dichroism in near-edge X-ray absorption fine structure spectra of planar molecules. *Journal of Physical Chemistry C*, 117(13):6632–6638, 2013.

[59] M. Taillefumier, D. Cabaret, A.-M. Flank, and F. Mauri. X-ray absorption near-edge structure calculations with the pseudopotentials: Application to the K edge in diamond and α-quartz. *Physical Review B*, 66(19):195107, 2002.

[60] J. C. Slater, J. B. Mann, T. M. Wilson, and J. H. Wood. Nonintegral occupation numbers in transition atoms in crystals. *Physical Review*, 184(3):672, 1969.

[61] J. F. Janak. Proof that ∂ E / ∂ $n_i = \varepsilon$ in density-functional theory. *Physical Review B*, 18(12):7165, 1978.

[62] L. Triguero and L. G. M. Pettersson. Calculations of near-edge x-ray-absorption spectra of gas-phase and chemisorbed molecules by means of density-functional and transition-potential theory. *Physical Review B*, 58(12):8097–8110, 1998.

[63] A. Baby, G. Fratesi, S. R. Vaidya, L. L. Patera, C. Africh, L. Floreano, and G. P. Brivio. Anchoring and bending of pentacene on Aluminum (001). *The Journal of Physical Chemistry C*, 119(7):3624–3633, 2015.

[64] A. Baby, H. Lin, G. P. Brivio, L. Floreano, and G. Fratesi. Core-level spectra and molecular deformation in adsorption: V-shaped pentacene on Al (001). *Beilstein Journal of Nanotechnology*, 6(1):2242–2251, 2015.

[65] C. Gougoussis, M. Calandra, A. P. Seitsonen, and F. Mauri. First-principles calculations of x-ray absorption in a scheme based on ultrasoft pseudopotentials: From α -quartz to high- T_c compounds. *Physical Review B - Condensed Matter and Materials Physics*, 80(7):1–8, 2009.

[66] P. Giannozzi, S. Baroni, N. Bonini, M. Calandra, R. Car, C. Cavazzoni, D. Ceresoli, G. L. Chiarotti, M. Cococcioni, I. Dabo, A. Dal Corso, S. de Gironcoli, S. Fabris, G. Fratesi, R. Gebauer, U. Gerstmann, C. Gougoussis, A. Kokalj, M. Lazzeri, L. Martin-Samos, N. Marzari, F. Mauri, R. Mazzarello, S. Paolini, A. Pasquarello, L. Paulatto, C. Sbraccia, S. Scandolo, G. Sclauzero, A. P. Seitsonen, A. Smogunov, P. Umari, and R. M. Wentzcovitch. QUANTUM ESPRESSO: a modular and open-source software project for quantum simulations of materials. *Journal of Physics: Condensed Matter*, 21(39):395502, 2009.

[67] G. Binnig, H. Rohrer, C. Gerber, and E. Weibel. Surface studies by scanning tunneling microscopy. *Physical Review Letters*, 49(1):57, 1982.

[68] J. Tersoff and D. R. Hamann. Theory and application for the scanning tunneling microscope. *Physical Review Letters*, 50(25):1998, 1983.

[69] J. Tersoff and D. R. Hamann. Theory of the scanning tunneling microscope. *Physical Review B*, 31:805–813, Jan 1985.

[70] R. Temirov, S. Soubatch, O. Neucheva, A. C. Lassise, and F. S. Tautz. A novel method achieving ultra-high geometrical resolution in scanning tunnelling microscopy. *New Journal of Physics*, 10(5):053012, 2008.

[71] C. Weiss, C. Wagner, C. Kleimann, M. Rohlfing, F. S. Tautz, and R. Temirov. Imaging Pauli repulsion in scanning tunneling microscopy. *Physical Review Letters*, 105(8):086103, 2010.

[72] C. Weiss, C. Wagner, R. Temirov, and F. S. Tautz. Direct imaging of intermolecular bonds in scanning tunneling microscopy. *Journal of the American Chemical Society*, 132(34):11864–11865, 2010.

[73] C. Zwick, A. Baby, Gruenewald M., Verwüster E., Hofmann O. T., Forker R., Fratesi G., Brivio G. P., Zojer E., and Fritz T. Complex stoichiometry dependent reordering of 3,4,9,10-perylene tetracarboxylic dianhydride on Ag(111) upon K intercalation. *ACS Nano*, 2015. PMID: 26718635.

[74] C. J. Chen. Origin of atomic resolution on metal surfaces in scanning tunneling microscopy. *Physical Review Letters*, 65(4):448, 1990.

[75] J. I. Martínez, E. Abad, C. González, F. Flores, and J. Ortega. Improvement of scanning tunneling microscopy resolution with h-sensitized tips. *Physical Review Letters*, 108(24):246102, 2012.

[76] F. Donati, G. Fratesi, L. Ning, A. Brambilla, M. I. Trioni, A. L. Bassi, C. S. Casari, and M. Passoni. Electronic and magnetic properties of bulk Cr tips for scanning tunneling spectroscopy. *Physical Review B*, 87(23):235431, 2013.

[77] W. H. Mills and M. Mills. Ccxxx.—the synthetical production of derivatives of dinaphthanthracene. *Journal of the Chemical Society, Transactions*, 101:2194–2208, 1912.

[78] R. B. Campbell, J. M. Robertson, and J. Trotter. The crystal and molecular structure of pentacene. *Acta Crystallographica*, 14(7):705–711, 1961.

[79] Y. Y. Lin, D. J. Gundlach, S. F. Nelson, and T. N. Jackson. Stacked pentacene layer organic thin-film transistors with improved characteristics. *IEEE Electron Device Letters*, 18(12):606–608, 1997.

[80] S. F. Nelson, Y-Y Lin, D. J. Gundlach, and T. N. Jackson. Temperature-independent transport in high-mobility pentacene transistors. *Applied Physics Letters*, 72(15):1854–1856, 1998.

[81] D. Knipp, R. A. Street, A. Völkel, and J. Ho. Pentacene thin film transistors on inorganic dielectrics: Morphology, structural properties, and electronic transport. *Journal of Applied Physics*, 93(1):347–355, 2003.

[82] O. D. Jurchescu, J. Baas, and T. Palstra. The effect of impurities on the mobility of single crystal pentacene. *arXiv preprint cond-mat/0404130*, 2004.

[83] Y. Yamashita. Organic semiconductors for organic field-effect transistors. *Science and Technology of Advanced Materials*, 10(2):024313, 2009.

[84] G. Bavdek, A. Cossaro, D. Cvetko, C. Africh, C. Blasetti, F. Esch, A. Morgante, and L. Floreano. Pentacene nanorails on Au (110). *Langmuir*, 24(3):767–772, 2008.

[85] P. G. Schroeder, C. B. France, J. B. Park, and B. A. Parkinson. Energy level alignment and two-dimensional structure of pentacene on Au(111) surfaces. *Journal of Applied Physics*, 91(5):3010–3014, 2002.

[86] Y.-H. Chu, C.-H. Hsu, C.-I Lu, H.-H. Yang, T.-H. Yang, C.-H. Luo, K.-J. Yang, S.-H. Hsu, G. Hoffmann, C.-C. Kaun, et al. Spin-dependent molecule symmetry at a pentacene–Co spinterface. *ACS Nano*, 9(7):7027–7032, 2015.

[87] M. G. Betti, A. Kanjilal, and C. Mariani. Electronic states of a single layer of pentacene: standing-up and flat-lying configurations. *The Journal of Physical Chemistry A*, 111(49):12454–12457, 2007.

[88] K. Toyoda, I. Hamada, K. Lee, S. Yanagisawa, and Y. Morikawa. Density functional theoretical study of pentacene/noble metal interfaces with van der Waals corrections: vacuum level shifts and electronic structures. *The Journal of Chemical Physics*, 132(13):134703, 2010.

[89] M. Wießner, J. Kübert, V. Feyer, P. Puschnig, A. Schöll, and F. Reinert. Lateral band formation and hybridization in molecular monolayers: NTCDA on Ag (110) and Cu (100). *Physical Review B*, 88(7):075437, 2013.

[90] D. Lüftner, T. Ules, E. M. Reinisch, G. Koller, S. Soubatch, F S. Tautz, M. G. Ramsey, and P. Puschnig. Imaging the wave functions of adsorbed molecules. *Proceedings of the National Academy of Sciences*, 111(2):605–610, 2014.

[91] Y. S. Lee, J. H. Park, and J. S. Choi. Electrical characteristics of pentacene-based Schottky diodes. *Optical Materials*, 21(1-3):433–437, 2003.

[92] C. H. Kim and D. Jeon. Organic metal-semiconductor field-effect transistors using aluminum-pentacene schottky junctions. *Journal of the Korean Physical Society*, 57(6):1702–1706, 2010.

[93] S. Steudel, K. Myny, V. Arkhipov, C. Deibel, S. De Vusser, J. Genoe, and P. Heremans. 50 MHz rectifier based on an organic diode. *Nature Materials*, 4(8):597–600, 2005.

[94] V. Nádaždy, R. Durný, J. Puigdollers, C. Voz, S. Cheylan, and K. Gmucová. Experimental observation of oxygen-related defect state in pentacene thin films. *Applied Physics Letters*, 90(9):1–3, 2007.

[95] A. K. Pandey, P. E. Shaw, Ifor D. W. Samuel, and J. M. Nunzi. Effect of metal cathode reflectance on the exciton-dissociation efficiency in heterojunction organic solar cells. *Applied Physics Letters*, 94(10):10–12, 2009.

[96] D. Tondelier, K. Lmimouni, D. Vuillaume, C. Fery, and G. Haas. Metal/organic/metal bistable memory devices. *Applied Physics Letters*, 85(23):5763–5765, 2004.

[97] M. Simeoni, S. Picozzi, and B. Delley. An ab-initio study of pentacene on aluminum (100) surface. *Surface Science*, 562(1-3):43–52, 2004.

[98] G. Saranya, Shiny Nair, V. Natarajan, P. Kolandaivel, and K. Senthilkumar. A theoretical study of structural and electronic properties of pentacene/Al(100) interface. *Journal of Molecular Graphics and Modelling*, 38:334–341, 2012.

[99] H. Brune, J. Wintterlin, J. Trost, G. Ertl, J. Wiechers, and R. J. Behm. Interaction of oxygen with Al(111) studied by scanning tunneling microscopy. *The Journal of Chemical Physics*, 99(3):2128–2148, 1993.

[100] J. D. Pack and H. J. Monkhorst. "Special points for Brillouin-zone integrations"-a reply. *Physical Review B*, 16(4):1748–1749, 1977.

[101] M. Methfessel and A. T. Paxton. High-precision sampling for Brillouin-zone integration in metals. *Physical Review B*, 40(6):3616–3621, 1989.

[102] M. Mura, A. Gulans, T. Thonhauser, and L. Kantorovich. Role of van der waals interaction in forming molecule-metal junctions: flat organic molecules on the Au (111) surface. *Physical Chemistry Chemical Physics*, 12(18):4759–4767, 2010.

[103] D. C. Langreth, B. I. Lundqvist, S. D. Chakarova-Käck, V. R. Cooper, M. Dion, P. Hyldgaard, A. Kelkkanen, J. Kleis, L. Kong, S. Li, et al. A density functional for sparse matter. *Journal of Physics: Condensed Matter*, 21(8):084203, 2009.

[104] A. Tkatchenko, L. Romaner, O. T. Hofmann, E. Zojer, C. Ambrosch-Draxl, and M. Scheffler. van der Waals interactions between organic adsorbates and at organic/inorganic interfaces. *MRS bulletin*, 35(06):435–442, 2010.

[105] S. S. Zade, N. Zamoshchik, A. R. Reddy, G. Fridman-Marueli, D. Sheberla, and M. Bendikov. Products and mechanism of acene dimerization. A computational study. *Journal of the American Chemical Society*, 133(28):10803–10816, 2011.

[106] Z. Zhou and R. G. Parr. New measures of aromaticity: absolute hardness and relative hardness. *Journal of the American Chemical Society*, 111(19):7371–7379, 1989.

[107] P. Geerlings, F. De Proft, and W. Langenaeker. Conceptual density functional theory. *Chemical Reviews*, 103(5):1793–1873, 2003.

[108] M. F. Cheng and W. K. Li. A computational study of the Diels-Alder reactions involving acenes: Reactivity and aromaticity. *Chemical Physics Letters*, 368(5-6):630–638, 2003.

[109] S.T. Howard and T.M. Krygowski. Benzenoid hydrocarbon aromaticity in terms of charge density descriptors. *Canadian Journal of Chemistry*, 75(9):1174–1181, 1997.

[110] P. Von Ragué Schleyer, M. Manoharan, H. Jiao, and F. Stahl. The acenes: Is there a relationship between aromatic stabilization and reactivity? *Organic Letters*, 3(23):3643–3646, 2001.

[111] E. Steiner and P. W. Fowler. Ring Currents in Aromatic Hydrocarbons. *International Journal of Quantum Chemistry*, 60(1 996):609–616, 1996.

[112] K. B. Wiberg. Properties of Some Condensed Aromatic Systems. *The Journal of Organic Chemistry*, 62(17):5720–5727, 1997.

[113] J. Ossowski, J. Rysz, M. Krawiec, D. Maciazek, Z. Postawa, A. Terfort, and P. Cyganik. Oscillations in the Stability of Consecutive Chemical Bonds Revealed by Ion-Induced Desorption. *Angewandte Chemie International Edition*, 54(4):1336–1340, 2015.

[114] P.-O. Löwdin. On the Non-Orthogonality Problem Connected with the Use of Atomic Wave Functions in the Theory of Molecules and Crystals. *The Journal of Chemical Physics*, 18(3):365–375, 1950.

[115] P.-O. Lowdin. On the nonorthogonality problem. *Advances in Quantum Chemistry*, 5:185, 1970.

[116] E. Pehlke and M. Scheffler. Evidence for site-sensitive screening of

core holes at the Si and Ge (001) surface. *Physical Review Letters*, 71(14):2338–2341, 1993.

[117] L. Bianchettin, A. Baraldi, S. De Gironcoli, S. Lizzit, L. Petaccia, E. Vesselli, G. Comelli, and R. Rosei. Geometric and electronic structure of the N Rh (100) system by core-level photoelectron spectroscopy: Experiment and theory. *Physical Review B - Condensed Matter and Materials Physics*, 74(4):1–9, 2006.

[118] J. L. Cabellos, D. J. Mowbray, E. Goiri, A. El-Sayed, L. Floreano, D. G. de Oteyza, C. Rogero, J. E. Ortega, and A. Rubio. Understanding charge transfer in donor–acceptor/metal systems: A combined theoretical and experimental study. *The Journal of Physical Chemistry C*, 116(34):17991–18001, 2012.

[119] G. Fratesi, V. Lanzilotto, S. Stranges, M. Alagia, G. P. Brivio, and L. Floreano. High resolution NEXAFS of perylene and PTCDI: a surface science approach to molecular orbital analysis. *Physical Chemistry Chemical Physics*, 16(28):14834–14844, 2014.

[120] M. Klues, K. Hermann, and G. Witte. Analysis of the near-edge X-ray-absorption fine-structure of anthracene: A combined theoretical and experimental study. *Journal of Chemical Physics*, 140(1):0–9, 2014.

[121] G. Fratesi, C. Motta, M. I. Trioni, G. P. Brivio, and D. Sánchez-Portal. Resonant lifetime of core-excited organic adsorbates from first principles. *The Journal of Physical Chemistry C*, 118(17):8775–8782, 2014.

[122] Q. Chen, A. J. McDowall, and N. V. Richardson. Ordered structures of tetracene and pentacene on Cu(110) surfaces. *Langmuir*, 19(24):10164–10171, 2003.

[123] S. Lukas, G. Witte, and Ch. Wöll. Novel mechanism for molecular self-assembly on metal substrates: Unidirectional rows of pentacene on Cu(110) produced by a substrate-mediated repulsion. *Physical Review Letters*, 88:028301, Dec 2001.

[124] M. Eremtchenko, R. Temirov, D. Bauer, J. A. Schaefer, and F. S. Tautz. Formation of molecular order on a disordered interface layer: Pentacene/Ag(111). *Phys. Rev. B*, 72:115430, Sep 2005.

[125] V. Lanzilotto, C. Sanchez-Sanchez, G. Bavdek, D. Cvetko, M. F. Lopez, J. A. Martin-Gago, and L. Floreano. Planar growth of pentacene on the dielectric TiO_2 (110) surface. *The Journal of Physical Chemistry C*, 115(11):4664–4672, 2011.

[126] J. Wuesten, C. Ziegler, and T. Ertl. Electron transport in pristine and alkali metal doped perylene-3, 4, 9, 10-tetracarboxylicdianhydride (PTCDA) thin films. *Physical Review B*, 74(12):125205, 2006.

[127] I. G. Hill, A. Kahn, Z. G. Soos, and Jr R. A. Pascal. Charge-separation energy in films of π-conjugated organic molecules. *Chemical Physics Letters*, 327(3–4):181 – 188, 2000.

[128] G. G. Fuentes and M. Knupfer. Preparation and characterization of single-phase potassium-doped PTCDA thin films. *Physical Review B*, 70(23):233202, 2004.

[129] G. G. Fuentes and M. Knupfer. Electronic structure and work function of potassium-doped PTCDA thin films. *Applied Physics A*, 84(3):329–333, 2006.

[130] K. Heimer, J. Wuesten, S. Lach, and C. Ziegler. Interaction of alkali metals with perylene-3, 4, 9, 10-tetracarboxylic-dianhydride thin

films studied by IR spectroscopy. *The Journal of Chemical Physics*, 126(16):164709, 2007.

[131] J. Wüsten, K. Heimer, S. Lach, and C. Ziegler. Alkali metals in perylene-3, 4, 9, 10-tetracarboxylicdianhydride thin films. *Journal of Applied Physics*, 102(2):023708, 2007.

[132] C. Zazza, S. Meloni, A. Palma, M. Knupfer, G. G. Fuentes, and R. Car. Quasi-one-dimensional ko chain in PTCDA thin films: evidence from first-principles calculations. *Physical review letters*, 98(4):046401, 2007.

[133] J. Wüsten, S. Berger, M. Salomo, .A Mönnich, M. Bauer, S. Lach, M. Aeschlimann, and C. Ziegler. Hot-electron dynamics in thin films of sodium-doped perylene-3, 4, 9, 10-tetracarboxylic dianhydride. *Physical Review B*, 78(19):195326, 2008.

[134] T. Dienel, A. Krause, R. Alle, R. Forker, K. Meerholz, and T. Fritz. Alkali metal doped organic molecules on insulators: Charge impact on the optical properties. *Advanced Materials*, 22(36):4064–4070, 2010.

[135] S. C. B Mannsfeld and T. Fritz. Analysis of the substrate influence on the ordering of epitaxial molecular layers: The special case of point-on-line coincidence. *Physical Review B*, 69:075416, Feb 2004.

[136] M. Gruenewald, K. Wachter, M. Meissner, M. Kozlik, R. Forker, and T. Fritz. Optical and electronic interaction at metal–organic and organic–organic interfaces of ultra-thin layers of PTCDA and SnPc on noble metal surfaces. *Organic Electronics*, 14(9):2177–2183, 2013.

[137] R. Forker, C. Golnik, G. Pizzi, T. Dienel, and T. Fritz. Optical absorption spectra of ultrathin PTCDA films on gold single crystals: Charge

transfer beyond the first monolayer. *Organic Electronics*, 10(8):1448–1453, 2009.

[138] R. Forker, M. Gruenewald, and T. Fritz. Optical differential reflectance spectroscopy on thin molecular films. *Annual Reports Section" C"(Physical Chemistry)*, 108:34–68, 2012.

[139] K. Glöckler, C. Seidel, A. Soukopp, M. Sokolowski, E. Umbach, M. Böhringer, R. Berndt, and W-D Schneider. Highly ordered structures and submolecular scanning tunnelling microscopy contrast of PTCDA and DM-PBDCI monolayers on Ag (111) and Ag (110). *Surface Science*, 405(1):1–20, 1998.

[140] L. Kilian, E. Umbach, and M. Sokolowski. Molecular beam epitaxy of organic films investigated by high resolution low energy electron diffraction (SPA-LEED): 3, 4, 9, 10-perylenetetracarboxylicacid-dianhydride (PTCDA) on Ag (111). *Surface Science*, 573(3):359–378, 2004.

[141] Y. Zou, L. Kilian, A. Schöll, T. Schmidt, R. Fink, and E. Umbach. Chemical bonding of PTCDA on Ag surfaces and the formation of interface states. *Surface Science*, 600(6):1240–1251, 2006.

[142] S. K. M. Henze, O. Bauer, T-L Lee, M. Sokolowski, and F. S. Tautz. Vertical bonding distances of PTCDA on Au (111) and Ag (111): Relation to the bonding type. *Surface Science*, 601(6):1566–1573, 2007.

[143] D. E. Hooks, T. Fritz, and M. D. Ward. Epitaxy and molecular organization on solid substrates. *Advanced Materials*, 13(4):227–241, 2001.

[144] T. E. Weller, M. Ellerby, S. S. Saxena, R. P. Smith, and N. T. Skipper. Superconductivity in the intercalated graphite compounds C6Yb and C6Ca. *Nature Physics*, 1(1):39–41, 2005.

[145] G. Kresse and J. Furthmüller. Efficient iterative schemes for ab initio total-energy calculations using a plane-wave basis set. *Physical Review B*, 54(16):11169, 1996.

[146] T. Bučko, J. Hafner, and J. G. Ángyán. Geometry optimization of periodic systems using internal coordinates. *The Journal of Chemical Physics*, 122(12):124508, 2005.

[147] G. Kresse and D. Joubert. From ultrasoft pseudopotentials to the projector augmented-wave method. *Physical Review B*, 59(3):1758, 1999.

[148] L. Romaner, D. Nabok, P. Puschnig, E. Zojer, and C. Ambrosch-Draxl. Theoretical study of PTCDA adsorbed on the coinage metal surfaces, Ag (111), Au (111) and Cu (111). *New Journal of Physics*, 11(5):053010, 2009.

[149] M. Chelvayohan and C. H. B. Mee. Work function measurements on (110),(100) and (111) surfaces of silver. *Journal of Physics C: Solid State Physics*, 15(10):2305, 1982.

[150] G. M. Rangger, O. T. Hofmann, L. Romaner, G. Heimel, B. Bröker, R.-P. Blum, R. L. Johnson, N. Koch, and E. Zojer. F4TCNQ on Cu, Ag, and Au as prototypical example for a strong organic acceptor on coinage metals. *Physical Review B*, 79(16):165306, 2009.

[151] H. B. Michaelson. The work function of the elements and its periodicity. *Journal of Applied Physics*, 48(11):4729–4733, 1977.

[152] P. Statiris, H. C. Lu, and T. Gustafsson. Temperature dependent sign reversal of the surface contraction of Ag (111). *Physical Review Letters*, 72(22):3574, 1994.

[153] O. Bauer, G. Mercurio, M. Willenbockel, W. Reckien, C. H. Schmitz, B. Fiedler, S. Soubatch, T. Bredow, F. S. Tautz, and M. Sokolowski. Role of functional groups in surface bonding of planar π-conjugated molecules. *Physical Review B*, 86(23):235431, 2012.

[154] G. Heimel, L. Romaner, J.-L. Brédas, and E. Zojer. Organic/metal interfaces in self-assembled monolayers of conjugated thiols: A first-principles benchmark study. *Surface Science*, 600(19):4548–4562, 2006.

[155] T. Classen, G. Fratesi, G. Costantini, S. Fabris, F. L. Stadler, C. Kim, S. de Gironcoli, S. Baroni, and K. Kern. Templated growth of metal–organic coordination chains at surfaces. *Angewandte Chemie*, 117(38):6298–6301, 2005.

[156] V. Blum, R. Gehrke, F. Hanke, P. Havu, V. Havu, X. Ren, K. Reuter, and M. Scheffler. Ab initio molecular simulations with numeric atom-centered orbitals. *Computer Physics Communications*, 180(11):2175–2196, 2009.

[157] A. Hauschild, K. Karki, B. C. C. Cowie, M. Rohlfing, F. S. Tautz, and M. Sokolowski. Molecular distortions and chemical bonding of a large π-conjugated molecule on a metal surface. *Physical Review Letters*, 94(3):036106, 2005.

[158] S. Duhm, A. Gerlach, I. Salzmann, B. Bröker, R. L. Johnson, F. Schreiber, and N. Koch. PTCDA on Au (111), Ag (111) and Cu (111): correlation of interface charge transfer to bonding distance. *Organic Electronics*, 9(1):111–118, 2008.

[159] R. F. W. Bader. *Atoms in molecules*. Wiley Online Library, 1990.

[160] G. Henkelman, A. Arnaldsson, and H. Jónsson. A fast and robust algorithm for bader decomposition of charge density. *Computational Materials Science*, 36(3):354–360, 2006.

[161] E. Sanville, S. D. Kenny, R. Smith, and G. Henkelman. Improved grid-based algorithm for bader charge allocation. *Journal of Computational Chemistry*, 28(5):899–908, 2007.

[162] W. Tang, E. Sanville, and G. Henkelman. A grid-based bader analysis algorithm without lattice bias. *Journal of Physics: Condensed Matter*, 21(8):084204, 2009.

[163] M. Yu and D. R. Trinkle. Accurate and efficient algorithm for bader charge integration. *The Journal of Chemical Physics*, 134(6):064111, 2011.

[164] M. J. E. A. Frisch, G. W. Trucks, Hs. B. Schlegel, G. E. Scuseria, M. A. Robb, J. R. Cheeseman, G. Scalmani, V. Barone, B. Mennucci, G. A. Petersson, et al. Gaussian 09, revision a. 02, gaussian. *Inc., Wallingford, CT*, 200, 2009.

[165] J.-P. Blaudeau, M. P. McGrath, L. A. Curtiss, and L. Radom. Extension of Gaussian-2 (G2) theory to molecules containing third-row atoms K and Ca. *The Journal of Chemical Physics*, 107(13):5016–5021, 1997.

[166] D. D. Johnson. Modified Broyden's method for accelerating convergence in self-consistent calculations. *Physical Review B*, 38(18):12807, 1988.

[167] G. Kresse and J. Hafner. Ab initio molecular dynamics for liquid metals. *Physical Review B*, 47(1):558, 1993.

[168] D. Sanchez-Portal, E. Artacho, and J. M. Soler. Projection of plane-wave calculations into atomic orbitals. *Solid State Communications*, 95(10):685–690, 1995.